

# UC San Diego

## UC San Diego Electronic Theses and Dissertations

### Title

Multiscale Transport in Porous Media and Patterned Surfaces

### Permalink

<https://escholarship.org/uc/item/6zm734d8>

### Author

Ling, Bowen

### Publication Date

2016

Peer reviewed|Thesis/dissertation

UNIVERSITY OF CALIFORNIA, SAN DIEGO

SAN DIEGO STATE UNIVERSITY

**Multiscale Transport in Porous Media and Patterned Surfaces**

A dissertation submitted in partial satisfaction of the  
requirements for the degree  
Doctor of Philosophy

in

Engineering Science (Mechanical and Aerospace Engineering)

by

Bowen Ling

Committee in charge:

University of California, San Diego

Professor David Saintillan, Co-Chair  
Professor Prabhakar Bandaru  
Professor John McCartney

San Diego State University

Professor Ilenia Battiato, Chair  
Professor Gustaaf Jacobs

2016

Copyright  
Bowen Ling, 2016  
All rights reserved.

The dissertation of Bowen Ling is approved, and it is acceptable in quality and form for publication on microfilm and electronically:

---

---

---

---

---

Co-Chair

---

Chair

University of California, San Diego

San Diego State University

2016



DEDICATION

*To My Parents*

Xiaochun LING and Yaling LI

*and My Wife*

Ye TIAN.

EPIGRAPH

*Three Rules of Work:*

*Out of clutter find simplicity.*

*From discord find harmony.*

*In the middle of difficulty lies opportunity.*

—Albert Einstein

## TABLE OF CONTENTS

	Signature Page . . . . .	iii
	Dedication . . . . .	iv
	Epigraph . . . . .	v
	Table of Contents . . . . .	vi
	List of Figures . . . . .	ix
	List of Tables . . . . .	xiii
	Acknowledgements . . . . .	xiv
	Vita . . . . .	xviii
	Abstract of the Dissertation . . . . .	xx
Chapter 1	Introduction . . . . .	1
	1.1 A Brief History . . . . .	2
	1.2 Development of Multiscale Transport Theory . . . . .	7
	1.2.1 Upscaling methods . . . . .	8
	1.2.2 Advection-Diffusion Equation (ADE) in Coupled Systems . . . . .	10
	1.3 Multiscale Transport: Experimental Methods . . . . .	13
	1.3.1 Micromodels Fabrication . . . . .	15
	1.3.2 Visualization . . . . .	20
	1.3.3 Data Analysis . . . . .	24
Chapter 2	Macro-scale Dispersion in Coupled system: Theory . . . . .	33
	2.1 Introduction . . . . .	33
	2.2 Model Formulation . . . . .	38
	2.2.1 Flow Equations . . . . .	38
	2.2.2 Transport Equations . . . . .	41
	2.3 Homogenization and Upscaled Equations . . . . .	43
	2.4 Dispersion Coefficient and Matrix Properties . . . . .	47
	2.4.1 Thin porous matrix limit, $\Lambda \ll 1$ . . . . .	51
	2.4.2 Thick porous matrix limit, $\Lambda \gg 1$ . . . . .	53
	2.5 Validation and Model Accuracy: Numerical Experiments . . . . .	55
	2.5.1 Code validation . . . . .	55
	2.5.2 Upscaled Model's Accuracy and Predictivity . . . . .	56
	2.5.3 Upscaled model results . . . . .	62
	2.5.4 Comparison with existing models . . . . .	63

	2.6 Conclusions . . . . .	67
Chapter 3	Patterned microchannels as benchmark experiments for transport in fracture-matrix systems . . . . .	71
	3.1 Introduction . . . . .	71
	3.2 Material and Methods . . . . .	75
	3.2.1 Micromodels . . . . .	75
	3.2.2 Visualization and Measurement . . . . .	76
	3.2.3 Data Analysis . . . . .	78
	3.2.4 Porous Structure and Experiment Matrix . . . . .	78
	3.2.5 Analytical Models . . . . .	80
	3.3 Results: comparison with experimental data . . . . .	84
Chapter 4	Micro-scale Multi-phase Flow in Porous Media . . . . .	89
	4.1 Introduction . . . . .	89
	4.2 Microfluidic experiments . . . . .	93
	4.2.1 Design and photolithography . . . . .	93
	4.2.2 Experimental design . . . . .	95
	4.3 Experimental results . . . . .	97
	4.4 Numerical simulations . . . . .	101
	4.4.1 Deterministic two- and three-dimensional simula- tions . . . . .	102
	4.4.2 Stochastic two-dimensional simulations . . . . .	104
	4.5 Conclusions . . . . .	110
Chapter 5	Conclusions . . . . .	112
Appendix A	Derivation of the upscaled equations . . . . .	116
	A.1 Asymptotic Expansion . . . . .	116
	A.2 Order $\mathcal{O}(\sqrt{\epsilon})$ : $c_f^{(1)}$ and $c_m^{(1)}$ solutions . . . . .	118
	A.3 Order $\mathcal{O}(\epsilon)$ : $c_f^{(2)}$ and $c_m^{(2)}$ solutions . . . . .	119
	A.4 Upscaled Equations . . . . .	121
Appendix B	Thin Fracture Solution . . . . .	127
	B.1 Tang <i>et al.</i> 's solution . . . . .	127
	B.1.1 Equations and Boundary Conditions . . . . .	127
	B.1.2 Dimensionless Form . . . . .	129
	B.1.3 Solve the concentration for matrix . . . . .	130
	B.1.4 solve concentration in fracture . . . . .	131
	B.1.5 Inverse Laplace transform . . . . .	134

Appendix C	Derivation of the upscaled equations using flux model . . . . .	137
	C.1 Velocity . . . . .	137
	C.1.1 fracture . . . . .	137
	C.1.2 matrix . . . . .	138
	C.1.3 Symmetric top wall, pinned bottom wall . . . . .	139
	C.2 Solute Transport . . . . .	141
	C.2.1 fracture . . . . .	141
	C.2.2 Matrix . . . . .	143
	C.2.3 Boundary condition and Interface condition . . . . .	144
	C.3 General Steps of solving . . . . .	145
	C.4 Calculate dispersion coefficient $\kappa$ . . . . .	150
	C.4.1 Calculate $\mathbb{D}_f$ . . . . .	153

## LIST OF FIGURES

Figure 1.1:	Sir Geoffrey Ingram Taylor . . . . .	3
Figure 1.2:	Schematic of the three story lines and their interaction. . . . .	4
Figure 1.3:	Scan of the preface of Lamb’s 1st edition of “Hydrodynamics” (or as pointed out by himself the 2nd edition of his previous publication). . . . .	5
Figure 1.4:	(a) Fractured rock (work by Knight and Grab, <i>Geomorphology</i> 2014[161]); (b) An intragranular porous domain for pore-scale modeling (work by Liu and <i>et al.</i> [188]; (c) Channel-Matrix coupled system. . . . .	11
Figure 1.5:	Sophisticated micromodel with valves patterned for flow control (Work by S. Maerkl, from Squires and Quake [291]). . . . .	15
Figure 1.6:	Hele-Shaw cell experimental set up reported in Saffman and Taylor’s work[270]. . . . .	17
Figure 1.7:	Viscous fingering observed in the Hele-Shaw cell [54]. . . . .	18
Figure 1.8:	Same beads placed in different fluids with different Reflection Index (RI) [128]. . . . .	19
Figure 1.9:	General procedure and illustration of stereo lithography, work by Melchels <i>et al.</i> [213]. . . . .	20
Figure 1.10:	Complex three-dimensional structure created by stereo lithography, work by Tse <i>et al.</i> [321]. . . . .	21
Figure 1.11:	Illustration of general procedures of four methods in soft lithography, work by Xia and Whitesides [361]. . . . .	27
Figure 1.12:	Image of the concentration field indicated by the Florescent dye ALEXA-488. Bright green corresponds to higher concentration regime. Images were taken using exposure time 75 <i>ms</i> . . . . .	28
Figure 1.13:	Direct visualisation (a and c) and gamma scan of the same model. Work by Oostrom <i>et al.</i> [234]. . . . .	29
Figure 1.14:	Schematic illustration of confocal microscopy. Work by Minsky [219]. . . . .	29
Figure 1.15:	Intensity measured in the shown micromodel for different instance. . . . .	30
Figure 1.16:	Calibration procedure used in the solute transport study . . . . .	30
Figure 1.17:	(a) Original bright field image collected form the experiment; (b) Boundary detected image; (c) Flooded image; (d) Original florescent image collected form the experiment; (e) Boundary detected image; (f) Flooded image . . . . .	31
Figure 1.18:	Mater-plane and 3D histogram plot . . . . .	32
Figure 1.19:	Result of image process by using the “3D histogram” analysis . . . . .	32
Figure 2.1:	Problem domain. . . . .	39
Figure 2.2:	Normalized dispersion coefficients $\kappa_f$ (solid red lines) and $\kappa_d$ (dashed back line) versus <i>Pe</i> for different values of $\lambda$ and $\Lambda$ . Also, $\Psi = -0.78$ and $h = 10$ . . . . .	48

Figure 2.3:	(a) Scaling behavior of the normalized dispersion coefficient $\Pi$ defined in (2.46) for thin porous media ( $\Lambda \lesssim 1$ ) and (b) $h < 1$ and $h > 1$ . The coefficient $\Pi$ , i.e. transverse dispersion, is controlled by the width $h$ of the porous matrix when $\Lambda \lesssim 1$ ; this dependence goes from linear to quadratic as $h$ increases above the threshold $h \approx 1$ . . . . .	52
Figure 2.4:	Scaling behavior of the normalized dispersion coefficient $\Pi$ defined in (2.46) for thick porous media ( $\Lambda \gg 1$ ). The normalized dispersion coefficient is controlled by matrix permeability only, when $\Lambda \gg 1$ . . . . .	54
Figure 2.5:	Comparison between the averaged 2D concentration in the channel and the 1D analytical solution, equation (2.56) [233], for passive scalar transport in a single channel with uniform velocity and constant injection. The average concentration $\langle c_f \rangle$ is plotted in terms of the dimensionless distance from the channel inlet at different instances in time $\tilde{t}$ . $h = 10$ , $\phi = 1$ , $\epsilon = 0.01$ , $D_f = D_{mx} = D_{my} = 1$ and $u_f = u_m = u^* = 0.01$ . . . . .	56
Figure 2.6:	(Left) Average concentration profiles $\langle c_f \rangle$ along the channel obtained either from the upscaled 1D (solid lines) or the pore-scale 2D equations (dashed lines) for different instances in time and Péclet numbers, i.e. $Pe = \{0.1, 10, 100, 1000\}$ . (Right) Absolute error $E_f(x, t) :=  \langle c_f \rangle_{2D} - \langle c_f \rangle_{1D} $ corresponding to each simulation. The dashed horizontal line represents the error bound $\sqrt{\epsilon}$ prescribed by homogenization theory. . . . .	58
Figure 2.7:	Simulation parameters: $\epsilon = 0.02$ , $\lambda = 31.6$ , $\phi = 0.1$ , $\Psi = -0.78$ , $D_f = 1$ , $D_{mx} = 0.1$ , $D_{my} = 0.1$ , $h = 10$ . (Left) Average concentration profiles $\langle c_f \rangle$ along the channel obtained either from the upscaled 1D (solid lines) or the pore-scale 2D equations (dashed lines) for different instances in time. (Right) Absolute error $E_f(x, t) :=  \langle c_f \rangle_{2D} - \langle c_f \rangle_{1D} $ corresponding to each simulation. The dashed horizontal line represents the error bound $\sqrt{\epsilon}$ prescribed by homogenization theory. . . . .	59
Figure 2.8:	Time evolution of the channel average concentration $\langle c_f \rangle$ calculated at location $x^* = b$ for different $\lambda$ and Péclet numbers. The parameters used in the simulations are $\phi = 0.01$ , $\Psi = -0.78$ , $\epsilon = 0.01$ , $D_f = 1$ , and $h = 10$ . . . . .	61
Figure 2.9:	Difference between the average concentration in the channel $\langle c_f \rangle$ for two values of dimensionless permeability $\lambda = \sqrt{10^2}$ and $\lambda = \sqrt{10^3}$ and different Péclet numbers, obtained from (3.6). A set of parameters used in the simulations is: $\phi = 0.5$ , $\Psi = -0.78$ , $\epsilon = 0.02$ , $D_f = 1$ , $D_{mx} = 0.1$ , $D_{my} = 0.1$ , $h = 10$ . Concentration $\langle c_f \rangle$ is measured at $x = 1$ . . . . .	62

Figure 2.10:	Comparison between $\langle c_f \rangle$ (solid lines) and $\langle c_m \rangle$ (dashed lines) for low (top) and (high) Péclet numbers. The simulation parameters are $\phi = 0.5$ , $\Psi = -0.78$ , $\epsilon = 0.02$ , $D_f = 1$ , $D_{mx} = 0.1$ , $D_{my} = 0.1$ , $h = 10$ . Concentration $\langle c_f \rangle$ and $\langle c_m \rangle$ are measured at $x = 1$ . . . . .	64
Figure 2.11:	(Left) Comparison between the breakthrough curves obtained from (3.6a) and (2.57) (by Dejam <i>et al.</i> ) with the averaged pore-scale solution for two permeability values, $\lambda = 0.3$ and $\lambda = 100$ . (Right) Absolute errors between upscaled solutions (3.6a) and (2.57) and the averaged pore-scale solution $E_{1D}(x, t; \lambda) :=  \langle c_f \rangle_{2D} - \langle c \rangle_{f,1D} $ and $E_D(x, t; \lambda) :=  \langle c_f \rangle_{2D} - \langle c \rangle_{f,Dejam\ et\ al.} $ , respectively. The simulations parameters are: $\epsilon = 0.02$ , $\phi = 0.1$ , $\Psi = -1$ , $D_f = 1$ , $D_{mx} = 0.1$ , $D_{my} = 0.01$ , $h = 10$ . . . . .	66
Figure 3.1:	Schematics of the experimental setup: (a) micromodel design with valve system, (b) exterior flow system, and (c) an example of measured concentration distribution, where the dye concentration increases with the intensity of the green colour. . . . .	75
Figure 3.2:	Intensity-concentration relations for three exposure times. The error bar represents three standard deviations. . . . .	77
Figure 3.3:	Error ratio $E_{Disp}/E_{Diff}$ plotted in Péclet number (Pe) and dimensionless permeability ( $\lambda$ ) space. Dots are representing exact value of the ratio, colored space filled is cubic fitting based on the exact value points. Warm color corresponds to values that are larger than 1. . . . .	85
Figure 3.4:	Comparison between experimental data collected at $\tilde{x} = 2$ mm along the channel patterned by transverse R1 riblets (symbols) and the fitted analytical solution (3.4) (line) for different values of the Péclet number. The error bars represent one standard deviation of the average concentration from its mean value. . . . .	86
Figure 3.5:	Comparison between experimental data collected at $\tilde{x} = 2$ mm along the channel patterned by cylinder structures C1 (squares) and C3 (circles) and the fitted analytical solution (3.6) (line) for different values of the Péclet number. The error bars represent one standard deviation of the average concentration from its mean value. . . . .	87
Figure 4.1:	(a) Pore Structure. Pore spaces are shown in black, and the solid phase is in white; (b) Three-dimensional configuration. . . . .	94
Figure 4.2:	(a) Illustration of the piping system; (b) Realization; (c) Flow path in different phases of the experiment. . . . .	96
Figure 4.3:	Definition of the Non-wetting/wetting fluid and contact angle. . . . .	97
Figure 4.4:	Five repetitions (first, second, third, fourth, and fifth rows, respectively) of drainage (first column) and imbibition (second column) in the microcell D. . . . .	98



Figure 4.5:	The second repetition in cell A (first row), cell B (second row), cell C (third row), cell E (forth row), and cell F (fifth row) of drainage (first column) and imbibition (second column). . . . .	99
Figure 4.6:	Interfacial length at the end of the drainage (left) and imbibition (right) cycles obtained in the experiments and numerical simulations. . . . .	100
Figure 4.7:	Saturation at the end of the drainage (left) and imbibition (right) cycles obtained in the experiments and numerical simulations. . . . .	100
Figure 4.8:	<b>Left:</b> Definition of the master plane and the mapping process; <b>Right:</b> $p(\xi, \eta)$ of all the experimental results. . . . .	101
Figure 4.9:	Three-dimensional simulation of (a) drainage and (b) imbibition with constant injection velocity $9.24 \times 10^{-4}$ m/s. . . . .	103
Figure 4.10:	Two-dimensional simulation of (a) drainage and (b) imbibition with constant injection velocity $9.24 \times 10^{-4}$ m/s. . . . .	104
Figure 4.11:	Two-dimensional simulation of (left column) drainage and (right column) imbibition with random injection velocity with mean $9.24 \times 10^{-4}$ m/s and CV=0.05. Different rows are different realizations. . . . .	105
Figure 4.12:	Two-dimensional simulation of (left column) drainage and (right column) imbibition with random injection velocity with mean $9.24 \times 10^{-4}$ m/s and CV=0.1. Different rows are different realizations. . . . .	106
Figure 4.13:	Coefficient of variance of the interface length at the end of drainage (left) and imbibition (right) cycles observed in the experiments and computed from the stochastic simulations. . . . .	107
Figure 4.14:	Two-dimensional simulation of (left column) drainage and (right column) imbibition with random injection velocity with mean $9.24 \times 10^{-1}$ m/s and CV=0.1. Different rows are different realizations. . . . .	108
Figure 4.15:	<b>Top:</b> $p(\xi, \eta)$ of simulation with variance of 0.05; <b>Bottom:</b> $p(\xi, \eta)$ of simulation with variance of 0.1. . . . .	109
Figure 4.16:	Contour lines with $p = 0.9$ , $p = 0.7$ , $p = 0.5$ . . . . .	109
Figure 4.17:	Contour lines comparison between the deterministic simulations with the experimental results with different $p$ values. . . . .	110

## LIST OF TABLES

Table 1.1:	Classification of fabrication of microfluidic chips. . . . .	16
Table 1.2:	Different Visualization methods with their VOF and time required for each frame. . . . .	22
Table 3.1:	Overview of experimental conditions: volumetric flow rate $Q$ , Péclet number $Pe$ , structure porosity $\phi$ , and obstacles dimensions $d$ and $w$ , as defined in Figure 3.1. For all micromodels, the chip's length and depth are $L = 15$ mm and $H_z = 28.0 \mu\text{m}$ , respectively, the porous matrix width is $W = 1.5$ mm, and the fracture aperture is $b = 0.25$ mm. . . . .	79
Table 3.2:	Fitting parameters and modeling error for $\tilde{x}_1 = 2$ mm and $\tilde{x}_2 = 8$ mm. . . . .	83
Table 4.1:	Micromodel Dimensions . . . . .	93
Table 4.2:	Wetting (hexadecane) and non-wetting (DI water) fluid properties	97

## ACKNOWLEDGEMENTS

The moment has finally arrived. It is interesting how we humans remember things, we may not remember an important dimensionless number we use everyday, but would never forget some irrelevant things that happened only once, not even the tiniest details.

I still remember the moment I was entering Ilenia's office ( "Dr.Battiato" back then, it took me a month to change to "Ilenia", it's really abnormal/inappropriate to call advisor's first name in China), still remember the first thing I noticed was a paint, one of my advisor's many masterpieces. There is a gray figure with one of the saddest faces, on top of the person there are streams of rainbows, magnificently fascinating. I immediately realized that the person may not be sad about losing something but about what she/he's having: the mind is so colorful that makes no language suitable to present all of the ideas. Ilenia surely has this kind of beautiful mind that inspires our research projects so much. At almost every difficult point (e.g.the week before the second submission of the JFM paper), when everything seems stuck and there's no way we could move the project forward, Ilenia still have new idea which can lead to wonderful solutions. Contrarily to the freedom of mind, Ilenia may have the most rigorous and serious altitude on work, even on a space or a comma. The most nervous moment is not before the exams or getting reviews from the journal, but is receiving emails from Ilenia during the revision of papers. Although those comments with a lot of "!"-s (exclamation marks) really made me think " should I change to another job?

maybe I'm too dumb for this...", I have to say that I really appreciate the seriousness and effort Ilenia put in the work and I've learned a lot. Outside work, Ilenia takes great care of all of her students, she always says "Bowen, it's ok, you just tell that person (usually a big guy, to whom I cannot say no) Ilenia said that, and dump all of the blames on me, I will take care of it. You just need to focus on your work." which makes us feel that there always a person on our back. And all of those "bar meetings", "group dinners" make the PhD journey really a great enjoyment. With all these great memories, fancy languages become pale at this point, I just would like to say: thank you Ilenia, for being my PhD advisor, thank you.

I also would like to thank Alex, similarly, whom I call "Dr.Tartakovsky" first time went to PNNL (Pacific Northwest National Laboratory), people were so confused then told me "Oh, we don't call him Dr.Tartakovsky here, just Alex". Once, I was chatting with people after dinner about the "philosophy of life", when asked "what would be the perfect state of life", I said "maybe make some great achievements in one field but still be modest and keep learning, have a busy job which I enjoy doing but I can stop doing after maybe 5 pm everyday to have time to spend with family, have a great habit, be nice to other people and maybe tell un-funny jokes to my students/colleagues...Oh! just like Alex!" This pretty much summarizes my impression of a great life style that a guy can have, and thank Alex for letting me know it is achievable in academia. Despite the fact that you've never asked me for lunch when I was in PNNL, I really enjoyed every project we worked together and every piece of advice you provide. Thank you! It is always my pleasure and great honor to work with Ilenia and Alex, who showed me

how scientists should work and direct me toward that.

从2011年本科最后一年访问，2012年决定念博士，直到现在博士即将毕业，最大的感受，不是取得成绩的愉悦，而是不能陪伴在父母和亲人身边的无奈和难过。爸妈，谢谢你们对我的支持，无论是经济上还是精神上，在很多人的不理解，怀疑中，你们坚定不移支持着我，儿子叩谢！

我的妻子田野，给予了我无数的鼓励，陪伴着我度过了无数个难熬的时刻，谢谢！

爷爷奶奶外公外婆，每次拿着全A的成绩单给你们看，你们脸上的笑容，是给我的最好的礼物！特别感谢宏平舅舅，对我学术上的指导和帮助，大学深受您的感染，才觉得做学术特别“酷”！还有所有的亲人，谢谢你们对我的理解和支持！

特别感谢所有指导帮助过我的老师，小学的王羽左老师，初中的程龙老师，高中的沈水红老师，大学的李毅波老师，你们不仅帮助我学业上的成长，更重要的是，教育了我如何做人，谢谢！

最后，感谢我所有的同学，学长和朋友，“13班1111”的朋友们，那一个个通宵做实验，写论文的夜晚，因为你们的“鼓励”，不再单调，谢谢！还有孙明阳，谢谢你在我不在家乡的时候，对我父母和亲人的关心，谢谢！

The text of this dissertation includes the reprints of the following papers, either accepted or submitted for consideration at the time of publication. The dissertation author was the primary investigator and author of these publications.

## Chapter 2

Ling, B., Tartakovsky, A., Battiato, I., (2016), 'Dispersion controlled by permeable surfaces: surface properties and scaling'. *Journal of Fluid Mechanics*, 801, 13-42.

### **Chapter 3**

Ling, B., Oostrom, M., Tartakovsky, A., Battiato, I., (2016), 'Patterned microchannels as benchmark experiments for transport in fracture-matrix systems'. *Environmental Science and Technology*, Submission code: es-2016-05929v.

### **Chapter 4**

Ling, B., Bao, J., Oostrom, M., Battiato, I., Tartakovsky, A., (2016), 'Modeling variability of porescale multiphase flow experiments'. *Advanced Water Resource*, Submission code: ADWR-2016-349.

## VITA

2012	B.E. in Mechanical Engineering, Central South University, China
2011-2012	Visiting, University of California, Berkeley, California
2012-2014	Graduate Working, Mechanical Engineering, Clemson University, Clemson, South Carolina
2014-2015	PhD Intern, Fundamental and Computational Sciences Directorate, Pacific Northwest National Laboratory, Richland, Washington
2014-2016	PhD, Mechanical and Aerospace Engineering, University of California and San Diego State University, San Diego, California

## JOURNAL PUBLICATIONS

**B.Ling, A.Tartakovsky, I.Battiato**, Dispersion controlled by permeable surfaces: surface properties and scaling, *Journal of Fluid Mechanics* 801 (2016): 13-42.

**B.Ling, M.Oostrom, A.Tartakovsky, I.Battiato**, Patterned micro channels as benchmark experiments for transport in fracture matrix systems, (*Environmental Science and Technology*, Submission code: es-2016-05929v);

**B.Ling, J.Bao, M.Oostrom, I.Battiato, A.Tartakovsky**, Modeling variability of pore scale multiphase flow experiments, (*Advances in Water Resources*, Submission code: ADWR-2016-349);

**B.Ling, I.Battiato**, Energy-Based Classification of Liquid Jet Dynamics, (To be submitted to *Physics Review Letters*);

## SELECT PRESENTATIONS

**B.Ling, and I.Battiato**. Energy-based Classification of Liquid Jet Dynamics. (2013, APS-DFD, Poster);

**B.Ling, and I.Battiato**. Energy-based Classification of Liquid Jet Dynamics: Experiments and Theory. (2014, APS-DFD, Presentation);

**B.Ling, M.Oostrom, A.Tartakovsky and I.Battiato**. Transport Dynamics over Micro-patterned Surfaces. (2014, AGU, Poster);

**B.Ling**, and **I.Battiato**. Energy-based Classification of Liquid Jet Dynamics. (2015, 8th Joint-Doctoral Program Research Symposium, Poster);

**B.Ling**, **M.Oostrom**, **A.Tartakovsky** and **I.Battiato**. Transport Dynamics over Micro-patterned Surfaces: Theory and Experiment. (2015, SDSU Student Research Symposium, Presentation);

**B.Ling**, **A.Tartakovsky** and **I.Battiato**. Analytical Study on Transport Dynamics over Micro-Patterned Surfaces. (2015, SOLCAL Research Symposium, Presentation);



ABSTRACT OF THE DISSERTATION

**Multiscale Transport in Porous Media and Patterned Surfaces**

by

Bowen Ling

Doctor of Philosophy in Engineering Science (Mechanical and Aerospace  
Engineering)

University of California, San Diego, 2016  
San Diego State University, 2016

Ilenia Battiato, Chair  
David Saintillan, Co-Chair

The aim of this dissertation is to establish a framework to describe multi-scale transport through porous media. Transport of mass and momentum in porous media can be studied at two different scales: the macro-scale (averaged-, continuum- or Darcy-scale) and the micro-scale (pore-scale). Particularly challenging from the modeling perspective are coupled systems (e.g. channel-matrix systems) and/or inherently unstable phenomena (e.g. multiphase transport). The former require multiscale ap-

proaches since the quantities of interest on one scale (e.g. macro-scale) may depend on the properties or physics at another scale (e.g. micro-scale). The latter challenge the very basic concept of system reproducibility as well as the perturbative approaches on which upscaling methods are generally based upon. The first part of this dissertation focuses on multi-scale mass transport in a two-dimensional channel embedded between two porous surfaces. By means of perturbation theory and asymptotic analysis, we first derive the set of upscaled equations describing mass transport in the coupled channel-matrix system and an analytical expression relating the macro-scale dispersion coefficient with the surface properties, namely porosity and permeability. Our analysis shows that their impact on dispersion coefficient strongly depends on the magnitude of Péclet number, i.e. on the interplay between diffusive and advective mass transport. Our analysis shows the possibility of controlling the dispersion coefficient, or transversal mixing, by either active (i.e. changing the operating conditions) or passive mechanisms (i.e. controlling matrix effective properties) for a given Péclet number. Then, we compare the upscaled model against experiments conducted on microchannels with surfaces patterned with different topologies. The experimental data are in agreement with the developed theory and quantitatively confirm the impact of the matrix geometry on dispersion at different Péclet numbers. Furthermore, we demonstrate that patterned microchannels can be used as benchmarks experiments to model flows in coupled channel/fracture-matrix systems. The second part of this dissertation focuses on experimentally quantifying and improving the reproducibility of pore-scale multiphase flow experiments. The unstable nature of multiphase flows

in porous media questions the basic concepts of both reproducibility and experimental benchmarking for numerical codes' validation and calibration. Subpore-scale heterogeneity and temporal fluctuations of experimental equipment can strongly control two-phase flow displacement data. We experimentally demonstrate that the introduction of spatial heterogeneity in pore-scale microfluidic models improves the reproducibility of multiphase flow experiments, and variability in fluid displacement between different realizations of the same experimental pore structure can be numerically captured by stochastic numerical simulations. The latter appears to be a more appropriate framework to describe unstable pore-scale displacement in multiphase transport.

# Chapter 1

## Introduction

Authors have different ways to start their scientific articles (e.g. books, journal papers, thesis). Especially the very first sentence of the introduction. Some may emphasize the great importance of their work, while others may convey the sense of the difficulty of the research topic. As a PhD student who has been working (“working” serves as a forgiving euphemism for “struggling”) on this subject for years, and yet has still decided to continue exploring this field as a life-time career, I started wondering that there must be something more than "a great importance to environmental/industrial applications" or "a commitment to solve such a difficult problems".

The old saying "Fortune favours the bold" also applies to the scientific world. Great pioneers like Newton, Maxwell, Schrödinger, and Prandtl, among others, had great bravery and the vision to establish something did not exist before and later became the foundation of entire new fields. When reading the establishment of any new field or development of new methods, one can always find a conflict between

great minds, painfully struggling to strip away the old, and, most importantly, the enjoyment of seeing a complete new landscape after overcoming all the obstacles. It is not the success of applying something that already exists that excites us, but the moment of saying "Oh, wait! This is counter-intuitive, isn't it interesting?!".

Therefore I would like to start my PhD dissertation by sharing a brief history of the multi-scale transport in porous media. Not only is the story itself serving as a respect of scientific giants, but also it ignited the passion and curiosity of exploring.

## **1.1 A Brief History**

An old saying in our country is: 'A great man is one who contributes enormously to one or several fields, finds links between those fields, and then opens a brand new way of looking at the world for people'. Sir G.I. Taylor surely fits this description as he made great contributions to many different fields: solid mechanics, fluid mechanics, turbulence, diffusion processes, hydrology and so on. As far as multi-scale transport, Taylor proposed a general approach of coupling physics at different scales. In 1921, he showed interest in diffusion processes [317] and introduced a general approach to derive the so called "longitudinal diffusion coefficient". In 1953 Taylor [316] proposed the idea of incorporating solute diffusion at a smaller scale (Taylor studied dispersion in a single tube, thus it is not "pore-scale") into dispersion at a larger scale. Such idea also links two different time scales (diffusion time scale and advection time scale) and provides a general framework to investigate the phenomenon at the macro-scale.



Figure 1.1: Sir Geoffrey Ingram Taylor

In the paper, Taylor intuitively proposed two conditions (later refined and derived theoretically by Aris[12]) which allow one to relate the transport process perpendicular to the flow direction with the longitudinal concentration gradient according to [316, Eq. (19)]

$$\frac{\partial^2 c}{\partial z^2} + \frac{1}{z} \frac{\partial c}{\partial z} = f(z) \frac{\partial c}{\partial x}, \quad (1.1)$$

where  $c$  is the concentration,  $z$  is the radial coordinate and  $x$  is the longitudinal axis. This equation is key to link micro-scale transverse with macro-scale longitudinal transport processes. Furthermore, the dispersion coefficient was derived. A similar idea was later adopted for the derivation of the dispersion in many other different scenarios (e.g., channels with reactive walls and with varying cross-section).

To illustrate why Taylor's work is of such great importance, we may look at the two separate paths undertaken by scientists before/after Taylor's work and the

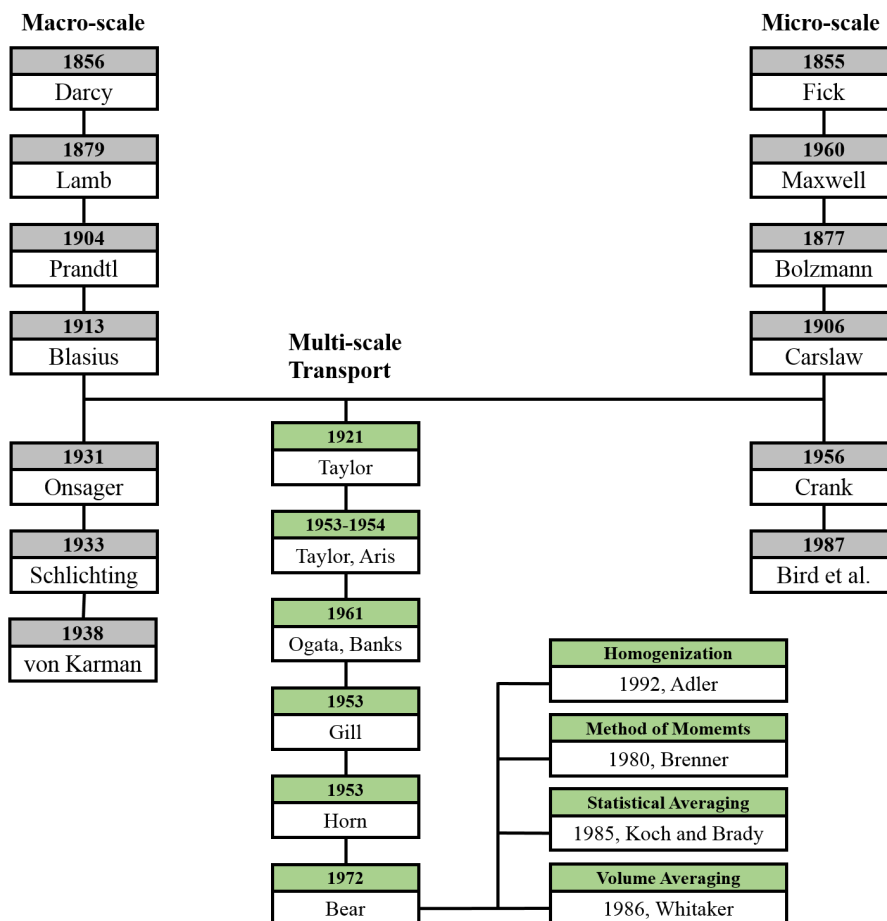


Figure 1.2: Schematic of the three story lines and their interaction.

missing link in between. As the terminology “multi-scale transport” suggests, we are interested in transport phenomena at/across different scales or, more specifically, on transport processes of mass and/or momentum in single/multi-phase flow in porous media at different scales and their coupling. Two paths (figure 1.2) originated from two fundamental physics laws in this field: Fick’s Law [99]

$$J = -D \frac{\partial c}{\partial x}, \quad (1.2)$$

and Darcy's Law [74]

$$q = -\frac{k}{\mu} \frac{\partial p}{\partial x}. \quad (1.3)$$

For simplicity, we used the one-dimensional form of these two laws. Here  $J$  is the molar flux ( $\text{mol m}^{-2}\text{s}^{-1}$ ),  $D$  is the molecular diffusion coefficient (or diffusivity), and  $c$  is the concentration. In Darcy's law,  $q$  ( $\text{m/s}$ ) is the discharge per unit area (i.e.  $q = Q/A$  where  $Q$  is the volumetric flow rate and  $A$  is the area), and  $p$  is pressure. In equation (1.2), or (1.3), the molar (or volumetric) flux depends on some intrinsic properties ( $D$ ,  $k$ ,  $\mu$ ) and the gradient. The negative sign indicates the direction of the flux is opposite to that of the gradient, i.e. transport always occurs from higher to lower concentrations/densities.

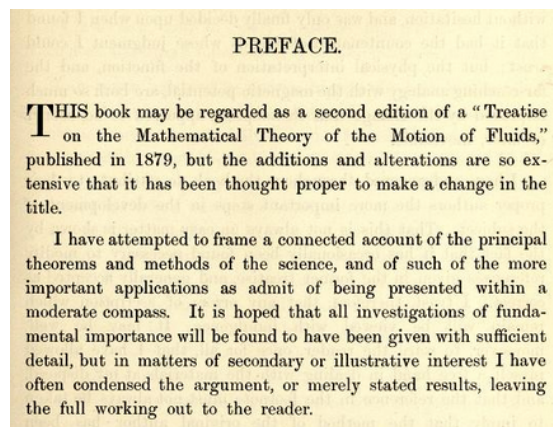


Figure 1.3: Scan of the preface of Lamb's 1st edition of "Hydrodynamics" (or as pointed out by himself the 2nd edition of his previous publication).

Interestingly, these two laws were proposed at the same time (1855 Fick's Law and 1856 Darcy's Law). Yet, they laid the foundations of two different perspectives



(micro-scale and marco-scale) on how scientists in this field study and interpret the physical world.

After Darcy proposed the macroscale transport equation (1.3) in 1879, Lamb published his book “A Treatise on the Mathematical Theory of the Motion of Fluids” [170], which was later named “Hydrodynamics” [171]. This book has been revised and re-published for the following hundred years and serves as one of the classic textbooks in hydrology. In 1904, Prandtl’s extraordinary work “Über Flüssigkeits bewegung bei sehr kleiner Reibung” (or “On the motion of fluids of very small viscosity”) [250] presents the boundary layer theory and, due to its revolutionary contribution, many refer him as the “father of modern fluid mechanics”. Later Blasius[38], Schlichting[277] made great contribution to the theory. Onsager and von Karman’s work on turbulence provided theoretical foundation for studying vegetated surfaces, drag-reduction etc.

On the Fick’s Law side of the diagram, Maxwell and Boltzmann studied movement of particles. Clarslaw’s work later became a classic textbook in heat transfer. Crank’s “The mathematics of diffusion” and Bird and *et al.*’s work “Transport phenomena” provided a general framework for solute transport problems. These transport governing equations solve the field point-wise whereas the quantities we are interested in (or physical laws we want to apply, e.g.the turbulent models) are at another scale and usually are averaged quantities. To find the bridge between these two paths, people adopt (or sometimes "re-discover") Taylor’s approach.

Through Taylor and Aris’s revolutionary work, now we are able to combine methods from both sides of the diagram (e.g. combine turbulent theory with transport

over nano-patterns, incorporate boundary layer theory with solute dispersion in fractured porous media). Methods that link transport physics at different scales then developed into the modern multi-scale transport theory.

In the following sections, we will introduce analytical and experimental approaches to systematically study multiscale transport.

## 1.2 Development of Multiscale Transport Theory

From the brief introduction of the multiscale transport history, one may have a hint of the importance of the “definition”. In almost all scientific research work, without a proper definition (of variable, operator, scale, dimension etc.), argument will lose all of its meaning. Some quantity/equation is defined “point-wise”, others may need a volume (or time interval) to ensure their validity. To get a rough (using “rough” is because we are, by default, looking at the scales where the continuum mechanics is still valid) idea about this difference, one may look at the example we used in the introduction of the history: Darcy’s equation and Fick’s equation.  $q$  (or very often used as “averaged velocity”) and the permeability all defined for a volume in Darcy’s equation. On the other side, in Fick’s law, the concentration  $c$ , the molecular diffusion coefficient ( $D$ ) are all defined at every point in the domain of interest. Or when one is studying the turbulence, the Reynolds decomposition of velocity:  $v = \langle v \rangle + v'$  where  $\langle v \rangle$  indicates the average/mean velocity and  $v'$  is the fluctuation also relies on a time interval to let the  $\langle \cdot \rangle$  operator be valid, but if one is solving the Navier-

Stokes equation then she/he can solve it for any time instance. The development of multiscale transport theory, thus, can be regarded as finding a definition of quantity or physics (the governing equation) which incorporate properties from a different scale. For instance, one of the main purpose of the Chapter 2 is: How to define (finding the expression of) the continuum scale dispersion coefficient which incorporates geometrical property at pore scale. At this point, one may ask: isn't that just taking averages? Yes, just taking averages (spatial or temporal), but in a smart way. The first part of this section is an introduction of different methods of taking averages using rigorous mathematical approach: upscaling methods. Then we will present how the upscaling technique is applied to find dispersion coefficient in coupled system.

### **1.2.1 Upscaling methods**

The essence of multiscale transport theories is to define the relationship between the physics at one scale and the properties at another scale under certain conditions. This could be achieved by upscaling or downscaling. If one is interested in macro-scale behavior (e.g.concentration field at the continuum scale, average velocity at the Darcy scale etc.) and wants to relate the physical properties at the micro scale (complex geometry at the pore-scale, reactive surface at the micro-scale, etc.), she/he may use upscaling methods for such a purpose. Some of these approaches include

- Homogenization theory [5, 129, 136, 144];
- Volume-averaging method [346, 151, 117, 259];

- Method of moments [272, 282, 283, 159, 48, 104];
- Statistical averaging [164, 276, 246].

These approaches involve perturbative methods in various forms (single- and multiple-scale expansions, Reynolds-type decomposition, etc.) and allow a rigorous derivation of the macroscale equations satisfied by spatially averaged microscale (pore-scale) quantities. A critical aspect that distinguishes upscaling methods from a straightforward averaging of pore-scale equations is the error analysis associated with, or the approximation error of, the upscaling procedure. For instance, using homogenization theory by multiple-scale expansion one expands pore-scale quantity as a perturbation series:  $c = c_0 + \epsilon c_1 + \epsilon^2 c_2 + \mathcal{O}(\epsilon^3)$ . If one solves for  $c_0$ ,  $c_1$  and  $c_2$  explicitly, then the approximation error in  $\tilde{c} = c_0 + \epsilon c_1 + \epsilon^2 c_2$  is at the order of  $\epsilon^3$ , where  $\epsilon$  is a small parameter. Regardless of the number of terms one explicitly solves for, an error bound can always be obtained, provided that certain conditions are met. Such error bounds not only provide the accuracy of the upscaled solution, but, more importantly, information about its predictive capabilities, i.e. under which conditions the macroscopic (upscaled) solution can represent pore-scale processes with the accuracy prescribed by the upscaling procedure. This is the formal criterion to determine whether an effective model is predictive or not.

In Chapter 2, we demonstrate how to construct a continuum approximation of transport in a channel-matrix coupled system by means of perturbation theory and provide error bounds for the macroscopic approximation. Some details about the

system investigated as well as the tools employed are provided in the following section. For technical details of the derivation, we refer the reader to Chapter 2.

### **1.2.2 Advection-Diffusion Equation (ADE) in Coupled Systems**

In this thesis, we are particularly interested in predicting the concentration field in coupled systems (figure 1.4) where a channel (or fracture) is embedded in a porous medium (matrix). Such a system can be used to model both natural processes such as flows in fractured rocks (figure 1.4-(a)) and over sediment beds [112, 229, 32, 188], coral reefs and canopies [108, 223, 240, 29], nutrients uptake from roots [197, 110] and passive predatory strategies in some carnivorous plants [112, 189, 279], as well as engineering and biological systems including superhydrophobic [268, 237, 27] and slippery liquid-infused porous surfaces [71, 137], shear sensors, flows in blood vessels [340, 7] and above carbon nanotube forests [78, 26, 28].

One of the greatest technical difficulties in handling such systems is the disparity of scales between the characteristic length associated to the porescale (e.g. width of the fracture/channel) and the system scale (e.g. length of the fracture/channel). Such disparity requires the use of upscaling methods and the construction of a macroscopic approximation. However, one obstacle in achieving this lies in (semi)analytically solving advection-diffusion equations while accounting for the non-uniformity of the velocity profile in the channel and/or matrix: this complication is generally overcome, or better avoided, by assuming uniform velocity in the channel, purely diffusive transport in the matrix or both. The first analytical treatment of transport mechanisms in

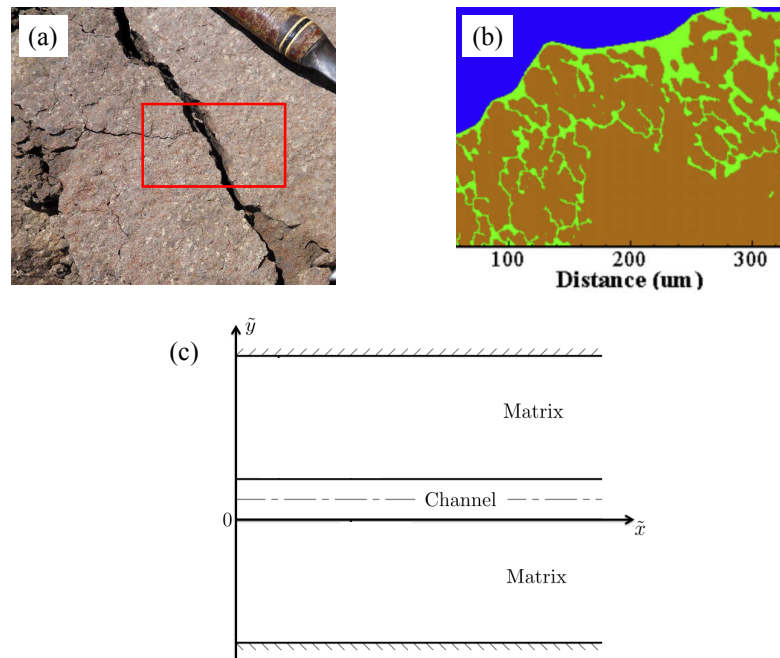


Figure 1.4: (a) Fractured rock (work by Knight and Grab, *Geomorphology* 2014[161]); (b) An intragranular porous domain for pore-scale modeling (work by Liu and *et al.*[188]); (c) Channel-Matrix coupled system.

channel-matrix systems is generally attributed to [303] (formulas are listed in appendix B), who considered a one-dimensional thin channel embedded in an impermeable (to flow) porous matrix. More recently, Dejam and *et al.*[79] coupled a two-dimensional ADE for the channel with a one-dimensional diffusion equation for the matrix. They considered a parabolic flow profile in the channel, and applied Reynolds decomposition to obtain an upscaled equation for the average concentration. By means of Laplace transform and numerical inverse Laplace transform, they studied transport

dynamics for different Péclet numbers. [118] considered transport in a cylindrical tube with a thin porous wall.

Most authors studied this problem by upscaling the transport equations in the channel and deriving the dispersion coefficient through a boundary flux type interfacial condition imposed on the channel-matrix interface, while ignoring flow in the matrix. Dispersion coefficients so derived can not only take the diffusion and advection effects into account but also couple the reaction on the interface. Similar to Taylor's derivation, these dispersion coefficients provide a physical insight of the flow and transport in the coupled system without explicitly solving the equations at the pore-scale. Here we list some dispersion coefficients commonly used and found in the literature.

- **1953, Taylor** [316, Eq. (25)]:

$$D_{Taylor-Aris} = 1 + Pe^2 \frac{1}{192} \quad (1.4)$$

- **1983, Horne, Rodriguez** [134, Eq. (10)]:

$$D_{HR} = Pe^2 \frac{2}{105} \quad (1.5)$$

- **1996, Berkowitz, Zhou** [37, Eq. (6)]:

$$D_{BZ} = 1 + Pe^2 \frac{8}{945} \quad (1.6)$$

- **2006, Parks, Romero** [242, Eq. (14)]:

$$D_{PR} = 1 + Pe^2 \frac{1}{210} \quad (1.7)$$

- **2007, Dentz, Carrera** [80, Eq. (75)]:

$$D_{DC} = 1 + Pe^2 \frac{2}{105} \quad (1.8)$$

- **2012, Wang, Cardenas, Deng, Bennett** [337, Eq. (28)]:

$$D_{WCDB} = 1 + Pe^2 \frac{72}{\pi^6} \sum_{n=1}^{\infty} [\cos(n\pi) + 1]^2 \left[ 1 - \exp\left(-\frac{Dn^2\pi^2 t}{b^2}\right) \right] \approx 1 + Pe^2 \frac{1}{213} \quad (1.9)$$

- **2013, Griffiths, Howell, Shipley** [229, Eq. (96)]:

$$D_{GHS} = 1 + Pe^2 \frac{A^2}{48(A+2)^2(1+\lambda\pi)^2}, \quad A = \frac{\alpha}{\sqrt{k}}, \quad \lambda = \frac{16\phi\alpha k}{\alpha + 4\sqrt{k}} \quad (1.10)$$

- **2014, Dejam, Hassanzadeh, Chen** [79, Eq. (71)]:

$$D_{DHC} = 1 + Pe^2 \frac{1}{175} \quad (1.11)$$

In (1.4)-(1.11), the Péclet number is defined as  $Pe = Ub/D_0$  with  $U$  the average velocity,  $b$  the aperture of the channel/fracture and  $D_0$  the molecular diffusion coefficient. All the dispersion coefficients listed above conveyed the same idea of using multi-scale transport theory to incorporate micro-scale physics/properties into the macro-scale effective equations by the dispersion coefficient.

### 1.3 Multiscale Transport: Experimental Methods

After the equations are derived and solutions achieved, an immediate question would be: can they predict the transport behavior? To answer this question, one



may compare the upscaled model with direct numerical simulations. Yet, pore-scale simulations are generally computationally expensive. Well controlled experiments are one irreplaceable evidence for model validation (analytical or numerical models).

In Chapter 3 and Chapter 4, we establish benchmark experiments for single phase and multiphase transport in porous media. In Chapter 3, a series experiments are performed on micro-patterned surfaces to validate the upscaled model derived in Chapter 2. This is based on the working hypothesis that a micro-patterned surface can be treated as porous media under certain conditions despite the fact that the number of arrays ( $\approx 5 - 10$ ) is much smaller than the number of pores and obstacles in conventional porous media (tens of thousands or even millions). The solution developed for porous media using upscaling approach and effective media theory is still predictive.

In Chapter 4, a more difficult problem is tackled: multiphase displacement in porous media. People spent many decades in studying multiphase flow theoretically, numerically and experimentally. Different models have been developed to predict immiscible fluids displacement. A common question scientists are facing is quite fundamental: reproducibility of multiphase flow experiments. The inherently unstable nature of multiphase flows introduce large uncertainty in experiments. Point-wise comparison (at the pore scale) becomes infeasible while comparing the averaged quantity (at the continuum scale) can not provide enough information for validation. In order to solve this dilemma, experimental technique and analysis algorithms are developed in Chapter 4, which evaluate the multiphase flow stochastically both for

the experiments and the simulation.

The possibility of realization of all these well controlled experiments relies on the fast development of the equipment and experimental methods. In this section, we will provide a general guide line of microfluidic devices including the fabrication, visualization, data analysis and how these are being applied in our studies.

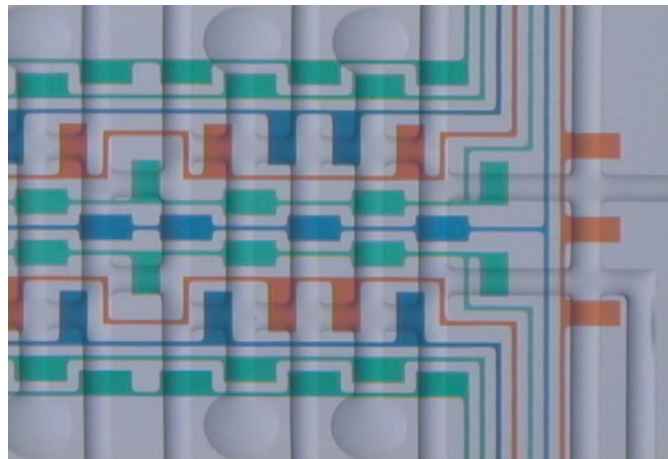


Figure 1.5: Sophisticated micromodel with valves patterned for flow control (Work by S. Maerkl, from Squires and Quake [291]).

### 1.3.1 Micromodels Fabrication

Different techniques can be adopted for the fabrication of microfluidic devices. They can be categorized in (i) material deposition and (ii) material removal methods.

In 1958, Saffman and Taylor [270] performed a series of experiments on the penetration of a fluid into a porous medium using Hele-Shaw cell (figure 1.6). In 1959 Chuoke and *et al.*'s work [62] showed the instability of the liquid-liquid displacement in the Hele-Shaw cell. Recent experimental study [54] by Bunton and *et al.* utilizes the

Table 1.1: Classification of fabrication of microfluidic chips.

<b>Techniques</b>	<b>Pro.</b>	<b>Con.</b>	<b>Studies</b>
Hele-Shaw cell	Low cost, Easy to make	Top view	1958, Saffman <i>et al.</i> [270] 2016, Bunton <i>et al.</i> [54]
Glass/Other Beads	Low cost, Easy to make	Random/3D	1952, Chatenever <i>et al.</i> [57] 2016, Fand <i>et al.</i> [96]
Optical lithography	Easy to replicate, Geometry	Clean room	1983, Thompson <i>et al.</i> [318]
Stereo lithography	Complex 3-D Geometry	Expensive	1986, Hull [140] 2003, Tse <i>et al.</i> [321]
Soft lithography	Easy to replicate, Geometry	Clean room	1998, Xia <i>et al.</i> [361] 2003, Quake <i>et al.</i> [255]
Wet etching	Easy to make	Wall surface	1983, Wegner [338] 2013, Grate [114]
Ion etching, DRIE	Accurate	Expensive	2008, Willingham [352] 2012, Karadimitriou [148]
Plasma/Laser etching	Accurate	Expensive	1990, Durandet [86] 2013, Mohammadi [220]

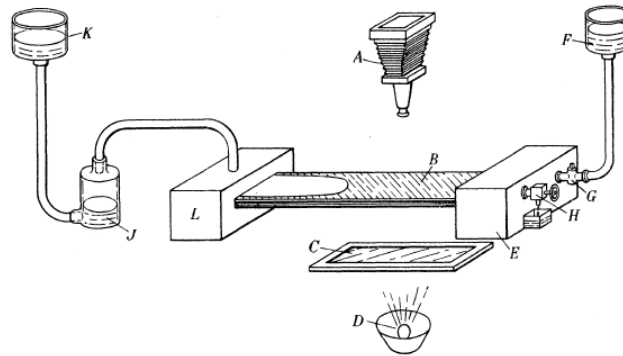


Figure 1.6: Hele-Shaw cell experimental set up reported in Saffman and Taylor's work[270].

Hele-Shaw cell to investigate viscous fingering (figure 1.7).

An early experimental study [57] applied one layer of glass beads in between of two parallel plates. As Chatenever and Calhoun pointed out, introducing multiple layers of beads would make the visualization more complicated. Recently, the use of polymer beads designed to match the optical index of the fluid allowed scientists to render the beads “invisible” (figure 1.8) and to visualize the velocity field at a fine temporal resolution [128, 96] by combining such indexed-matched techniques with Particle Image Velocimetry (PIV).

Optical lithography (or photo-lithography) has experienced a fast development during in the past few decades. Due to the precise realization of designed pore structure, network and etc., more and more experimentalists started using micromodels fabricated by lithographic techniques. Early studies (1980s) of the procedure can be found in Thompson *et al.*'s work [318]. A more recent review of the method can be found in Cheng *et al.* [59], and in the review paper by Karadimitriou and Hassanizadeh

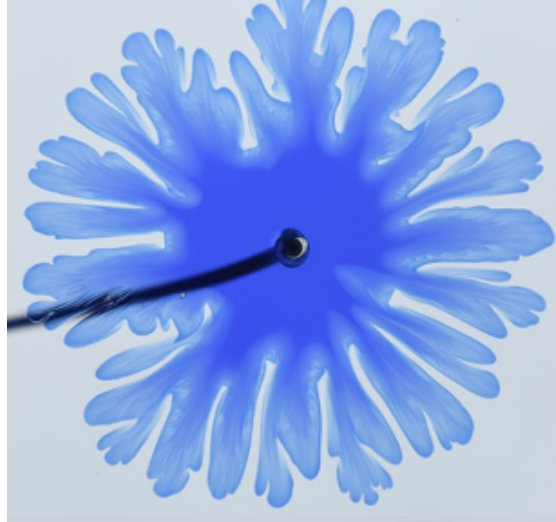


Figure 1.7: Viscous fingering observed in the Hele-Shaw cell [54].

[147]. In our study, the micromodels for the experiments (both non-reactive solute transport and multiphase transport) were fabricated using optical lithography.

Stereo-lithography, similar to 3D-printing, is an additive fabrication method by computer-aided system. Figure 1.9 shows a cartoon of the method: by means of a movable platform and a computer-controlled laser, different layers of the structure are deposited and melted. A review paper by Melchels *et al.* [213] provides a general introduction to this technique. Recent developed micro-stereo lithography is able to construct complex geometry as shown in Figure 1.10.

The general procedure of soft lithography shares many similarities with optical lithography, with the only difference that soft materials are utilized for the micromodels or replicas. As listed in the review paper by Xia and Whitesides [361], four different methods have been developed:

- Replica molding (REM) [94, 281];

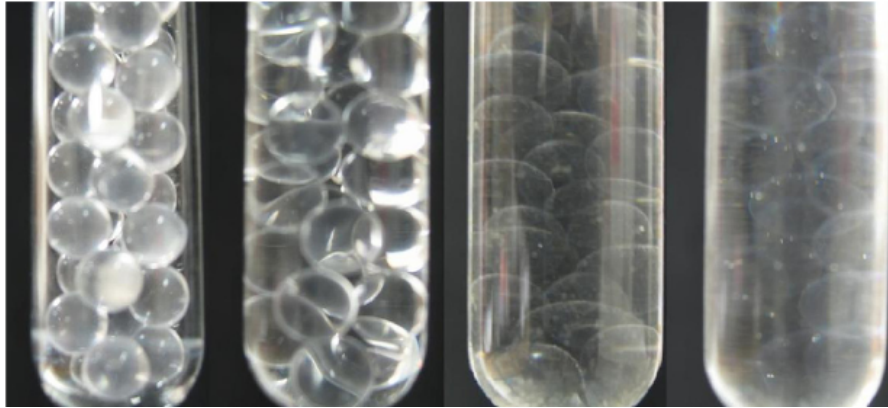


Figure 1.8: Same beads placed in different fluids with different Reflection Index (RI) [128].

- Microtransfer molding ( $\mu$ TM) [372, 154];
- Micromolding in capillaries (MIMIC) [155, 156];
- Solvent-assisted micromolding (SAMIM) [158, 176];

Schematics of the methods are shown in Figure 1.11. In our study, we applied the REM to produce micromodels for both single- and multi-phase flow experiments.

The fabrication method by material removal is based upon a wet etching technique developed in 1980s [338, 60]. The basic idea of wet etching is to remove the designed part on the wafer (silicon or glass) by etchants (*e.g.* acid). The remainder of the surface is covered by photo-resist or other resistance material (*e.g.* copper). Other etching methods exist that employ ions or laser as the “etchants”. The largest issue with etching is the vertical surface profile or property. Specifically, during wet etching the vertical walls are always curved due to the lack of control in vertical direction. The surface property can be largely improved with the newly developed technique of deep

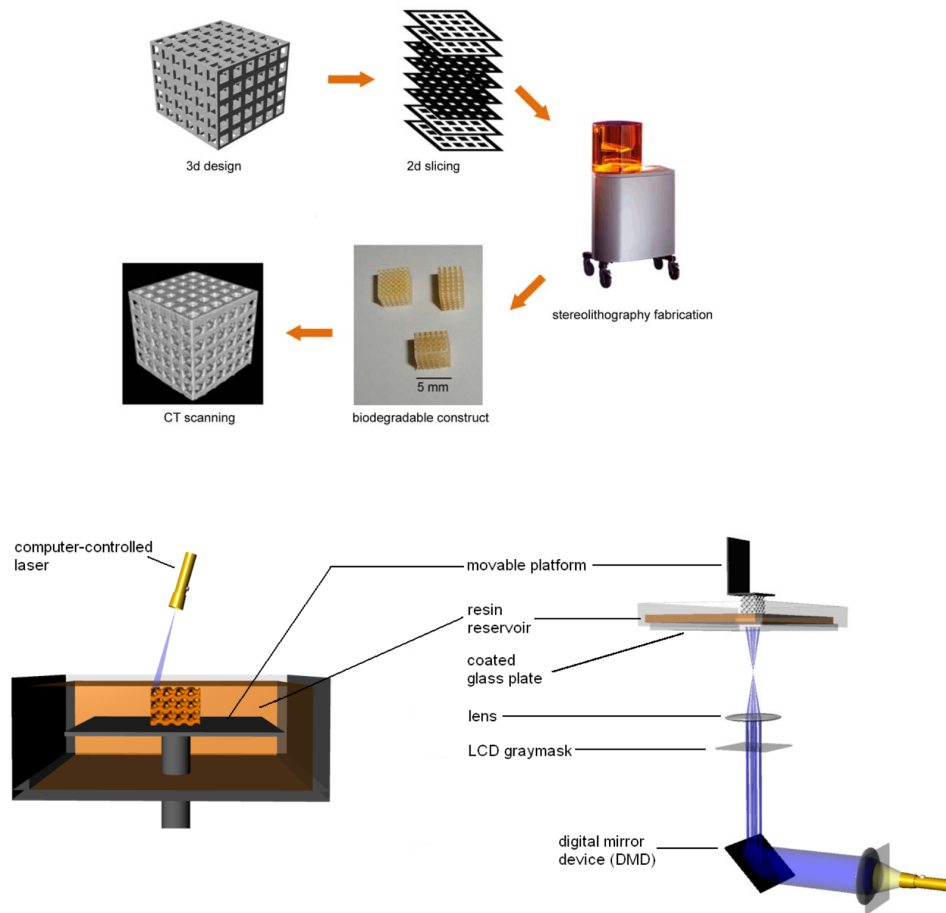


Figure 1.9: General procedure and illustration of stereo lithography, work by Melchels *et al.*[213].

reactive ion etching (DIRE) or plasma/laser etching [22, 275, 132, 142, 20, 204], yet the equipment cost may be prohibitive.

### 1.3.2 Visualization

As multi-scale transport requires, we need to observe and record transport physics at different scales. Generally, the more information one wants to achieve

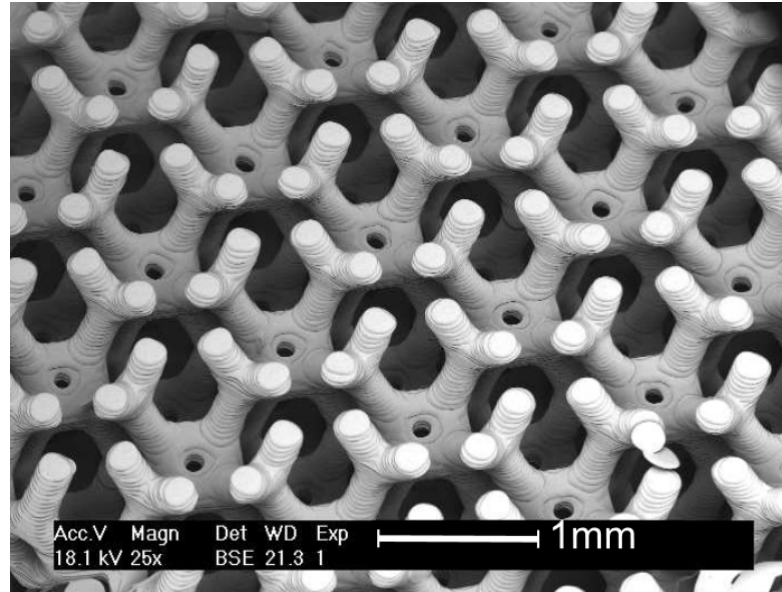


Figure 1.10: Complex three-dimensional structure created by stereo lithography, work by Tse *et al.*[321].

the greater effort she or he needs to spend. A review by Werth *et al.*[343] provides guidelines on how to select between different methods based the Field of View (FOV) and the temporal resolution needed. In table 1.2, we list the typical data for each method. A more detailed study can be found in Werth *et al.*'s [343].

Optical imaging method is a direct recording of light intensity. This may be the most straightforward method of measuring concentration fields. In order to indicate the transport of mass or momentum (solute transport, immisible fluid displacement, particles, velocity field, etc.) probing medium is added. For instance, florescent dye is frequently applied to the field. The florescent tracer only emits light in a certain range of the spectrum. In optical imaging, several methods can be used:

- Direct visualization [56, 65, 354, 289];



Table 1.2: Different Visualization methods with their VOF and time required for each frame.

<b>Techniques</b>	<b>Field of View</b>	<b>Time for each frame</b>	<b>References</b>
Optical Imaging	$10\mu m^2 - 0.12 m^2$	1/50 – 300s	2007, Oostrom <i>et al.</i> [235]
Gamma	$\approx 30 mm^2$	several – 45 s	1997, Barreau <i>et al.</i> [24]
X-ray	$0.001 mm^2 - 100 m^2$	1 – 1200 s	1997, Keller <i>et al.</i> [152], see also [58, 296]
Magnetic Resonance Imaging (MRI)	$0.001 mm^2 - 10 mm^2$	1 – 60 min	1997, Bora <i>et al.</i> [41], see also [172, 221]

- Regular microscopy [261, 330, 153, 243];
- Florescent microscopy [235, 368, 351, 347, 236];
- Confocal microscopy [115, 127, 368, 179, 212];
- Micro Particle Imaging Velocimetry ( $\mu$ PIV) [211, 274, 262, 344, 214];

Direct visualization, regular and florescent microscopy share the same idea of “using cameras to take pictures”. The main difference is the resolution scale and how to identify different substances we are interested in. For macro-scale (or Darcy scale) experiments, regular color-dye is generally used to indicate certain fluid’s displacement or mimic the behavior of the solute. To record the field without magnification, a regular camera or a high speed camera can be utilized. Instead, microscopes with different magnification objectives are used to observe the micro-scale fields. A charged coupled device (CCD) or a complementary metal-oxides semiconductor (CMOS) high speed camera is attached to the microscope and through a computer, the images can be recorded at 10 – 100 frames per second (fps).

One of the limitation of the three methods discussed above is that they can only record two-dimensional information. One can either take pictures from the top or from the side of the micromodels. Confocal microscopy can be used to overcome these shortcomings. Confocal microscopy was invented by Minsky in 1980s [219]. It uses optical apertures to enhance the contrast of images. It provides point-wise imaging by eliminating out-of-focus light signal and only the points close to the focal plane are recorded. By adjusting the focal plane, it is possible to reconstruct three-dimensional

information up to the maximum light penetration depth. The main limitation of confocal microscopy is the time needed for recording one image. As a result, it is suitable for studying steady or immobile transport systems but for three-dimensional unsteady problems, one may apply micro particle imaging velocimetry ( $\mu$ PIV). Similar to conventional PIV[251, 6, 350, 150], the  $\mu$ PIV introduces probing particles into the system and by taking two consecutive images the velocity vectors can be calculated. The difference between PIV and  $\mu$ PIV is the size of the probing particles.

### 1.3.3 Data Analysis

One could argue that the majority of experimental results are images, i.e. arrays of pixels with the values of intensity (light intensity or florescent intensity). There are many different ways to use these intensity data. The critical step is to convert them to physical quantities, e.g. concentration, fluid type, etc. In this brief introduction, we will present two different approaches employed in the experimental study of solute and multi-phase transport.

As shown in figure 1.15, in a typical florescent image we can have the intensity for different time instances recorded on a line. The bright green indicates a higher concentration of the fluorescent dye (ALEXA-488 is used in this image). In order to convert this intensity profile to concentration field, we need to perform calibration. For instance, the initial concentration ( $c_0$ ) of the dye solution used in this figure is  $34.40 \mu\text{mol}/L$ . We prepared solutions with  $100\%c_0$ ,  $75\%c_0$ ,  $50\%c_0$ ,  $25\%c_0$  and  $0\%c_0$  DI-water. The intensity of each solution at a fixed exposure time is measured at the

inlet of the micromodel. Figure 1.16 shows a linear relationship between intensity and concentration. By using this calibration result, we can convert all the intensity values in corresponding normalized concentration values.

For multiphase transport experiments, one may be more interested in the location of a given fluid (wetting phase or non-wetting phase) inside the micromodel. To analyze this, we can perform image processing. Figure 1.17 shows the procedure we employed in our study. After we collect bright field images (figure 1.17-a) or fluorescent images (figure 1.17-d), we use a Matlab boundary detecting code to convert the raw image into images shown in figure 1.17-b and 1.17-e. Then by using “Flood” algorithm [4], we can identify isolated fluid regions and find the space occupied by either the wetting or non-wetting fluid. Quantitative measurement of the interface length, saturation condition etc. of the experiments will be based on the processed images. The images (1.17-c and 1.17-f) processed from different experimental results are similar, therefore, all of our experimental results will be presented using bright field images.

In multi-phase fluid displacement experiments, due to the instability, the experimental results may be different even under the same condition and in the same micromodel. To identify and quantify these differences, we process the images and plot a “3-D histogram” of the probability of occupancy of each phase (wetting/nonwetting) at any given location in the micromodel. To illustrate this process, we introduce the idea of mater-plane. If one point  $A(\xi, \eta)$  on the master plane corresponds to a point  $A'(x, y)$  that is occupied by the non-wetting fluid, we add 1 to the two-dimensional

function  $P(\xi, \eta)$  which is defined on the master plane. A normalized function  $p(\xi, \eta)$  is defined as:  $p(\xi, \eta) = (1/N)P(\xi, \eta)$  where  $N$  is the number of results analyzed. The transformation from  $A$  to  $A'$  is done by multiplication of a transformation tensor. Figure 1.19 represents the  $p$  value from  $\sim 40$  experimental results. Some areas have a larger  $p$  value: this indicates the high probability of occupancy by a non-wetting fluid.

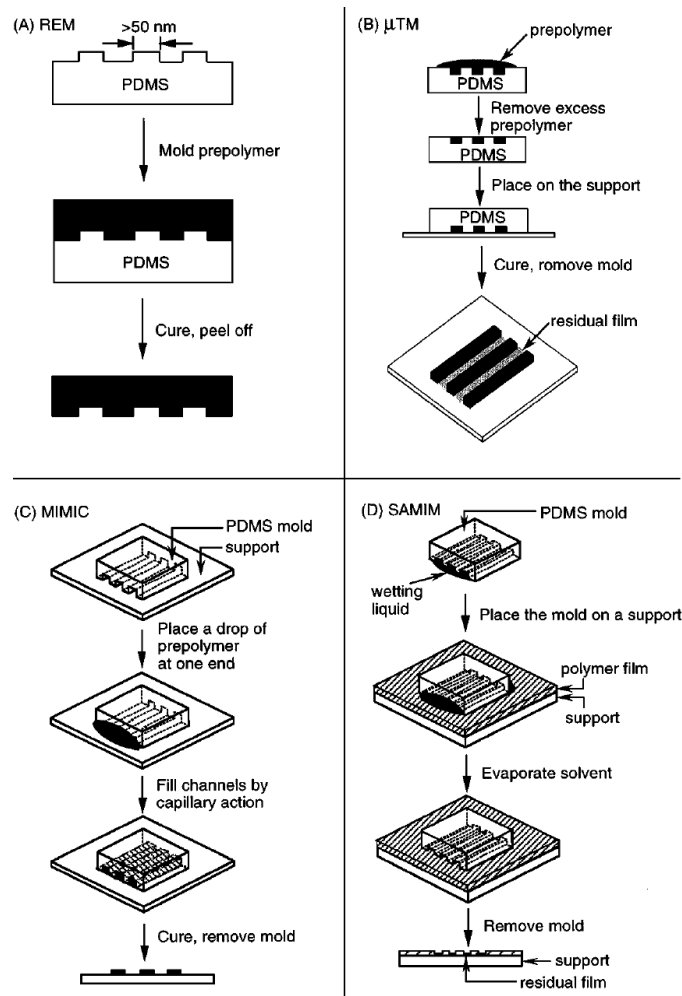


Figure 1.11: Illustration of general procedures of four methods in soft lithography, work by Xia and Whitesides [361].

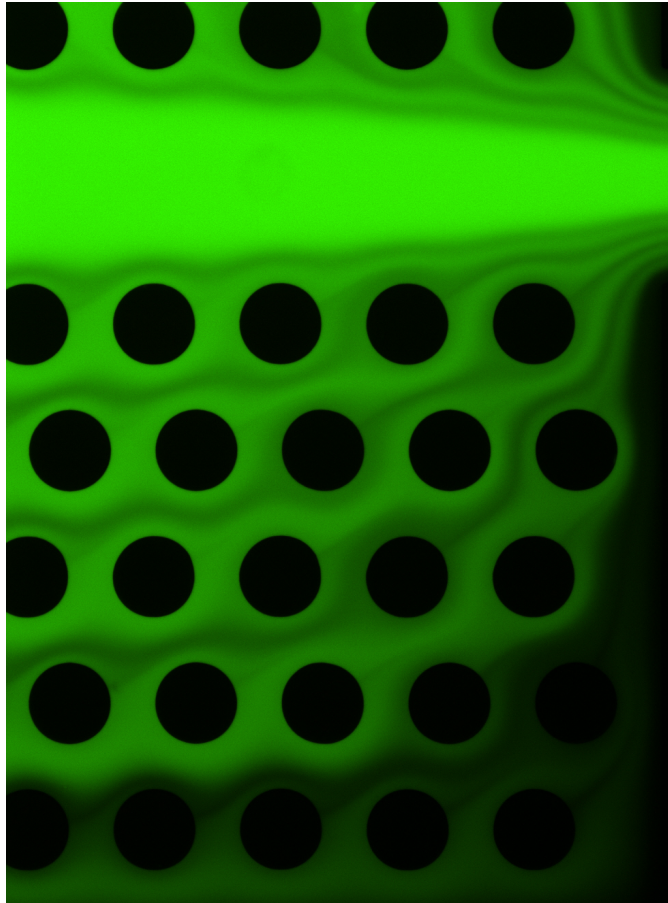


Figure 1.12: Image of the concentration field indicated by the Florescent dye ALEXA-488. Bright green corresponds to higher concentration regime. Images were taken using exposure time  $75\text{ ms}$ .

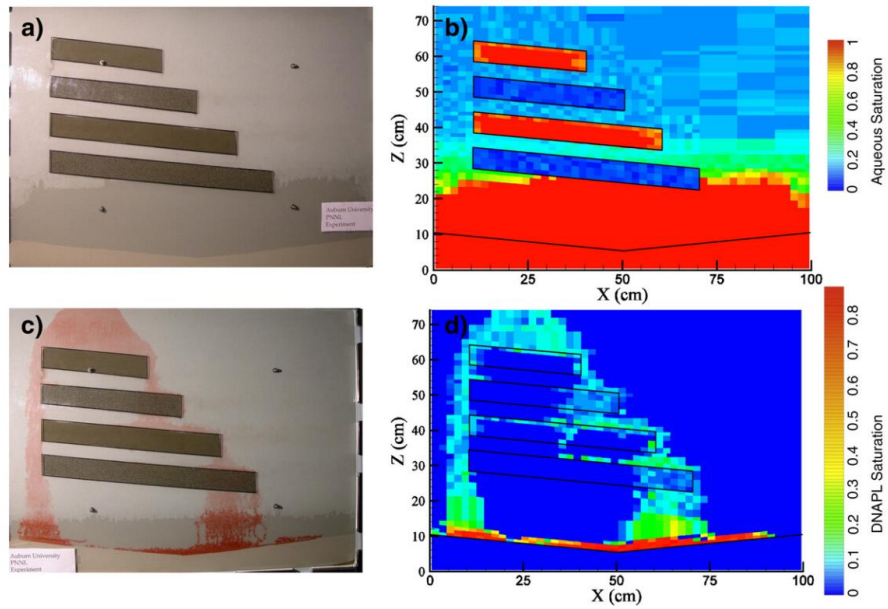


Figure 1.13: Direct visualisation (a and c) and gamma scan of the same model. Work by Oostrom *et al.*[234].

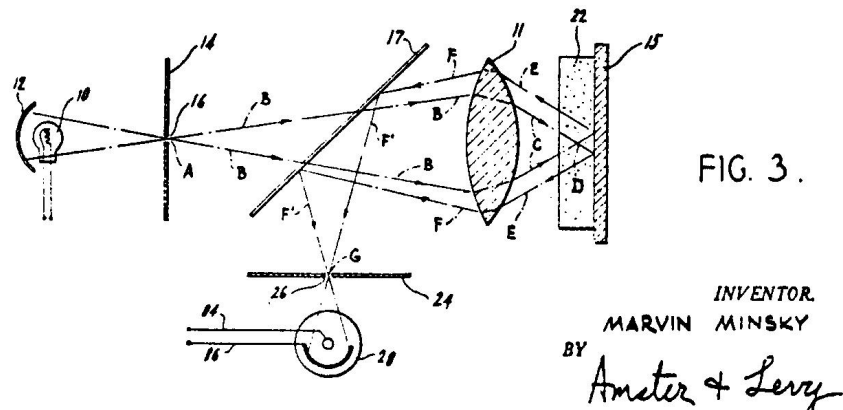


Figure 1.14: Schematic illustration of confocal microscopy. Work by Minsky [219].



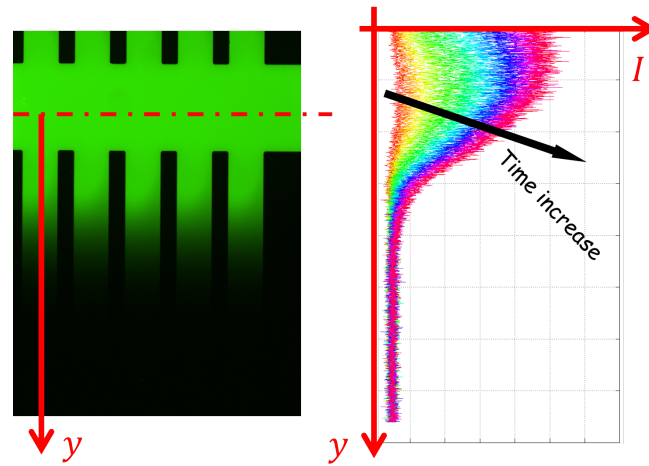


Figure 1.15: Intensity measured in the shown micromodel for different instance.

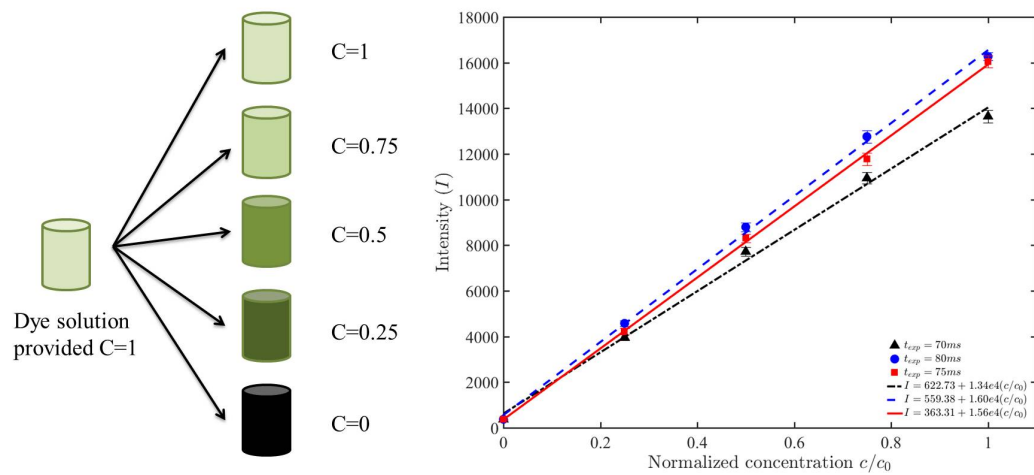


Figure 1.16: Calibration procedure used in the solute transport study

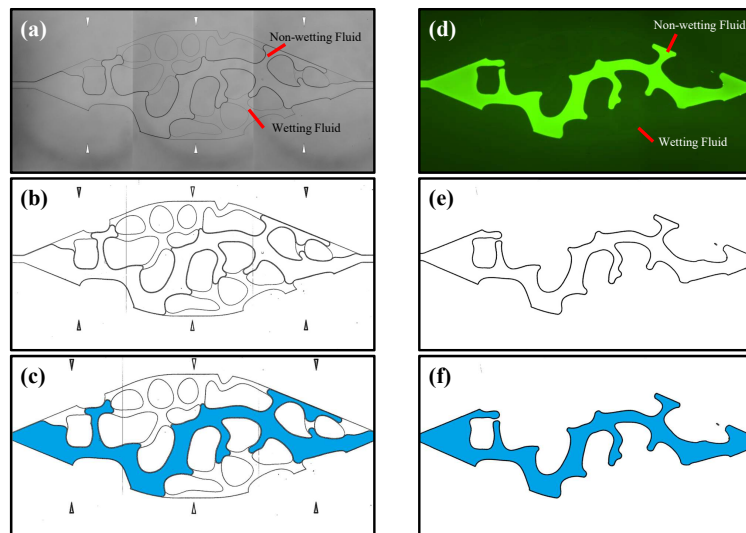


Figure 1.17: (a) Original bright field image collected form the experiment; (b) Bound-ary detected image; (c) Flooded image; (d) Original florescent image collected form the experiment; (e) Boundary detected image; (f) Flooded image

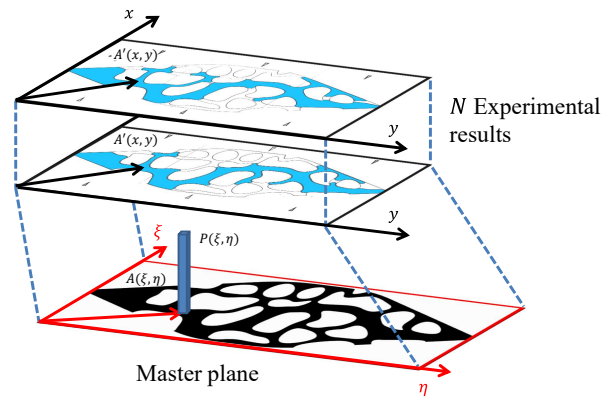


Figure 1.18: Mater-plane and 3D histogram plot

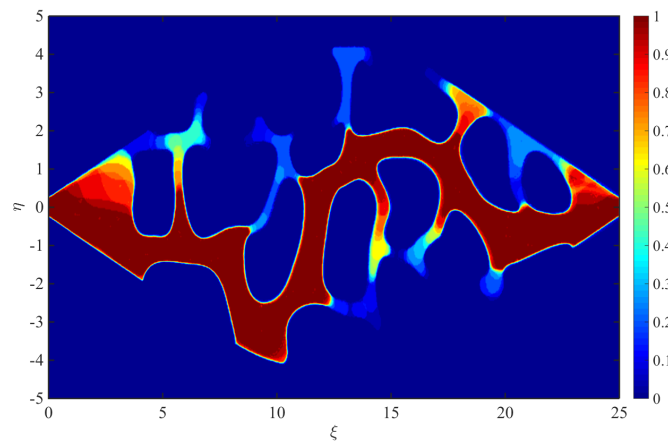


Figure 1.19: Result of image process by using the “3D histogram” analysis

## **Chapter 2**

# **Macro-scale Dispersion in Coupled system: Theory**

### **2.1 Introduction**

The unique features of patterned surfaces and porous coatings have been long recognized [e.g. 196]. Of particular interest are coupled flows and transport processes through and above permeable and/or (micro-) patterned layers as they are ubiquitous in environmental, biological and engineered systems. Examples of natural systems include transport in fractured rocks and flows over sediment beds [112, 229, 32, 188], coral reefs and canopies [108, 223, 240, 29], nutrients uptake from roots [197, 110] and passive predatory strategies in some carnivorous plants [112, 189, 279]. Coupled flows are critical to many engineering applications including superhydrophobic [268, 237, 27] and slippery liquid-infused porous surfaces [71, 137], shear sensors, flows in

blood vessels [340, 7] and above carbon nanotube forests [78, 26, 28], just to mention a few. Distinctive characteristics of micro-structured surfaces and nanoimprints are routinely adopted in a variety of other manufacturing processes including, but not limited to, ultrafiltration of colloids [200] and nutrient delivery in bioreactor devices [121, 118]. Channel transversal mixing is critical to, e.g., reduce membrane fouling or increase system's overall reactivity. This is particularly challenging in microfluidic devices where mixing is controlled by diffusion with resulting slow reaction rates. Surface patterns have been successfully employed to enhance transverse mixing in microchannels [298, 297] and reduce membrane fouling [341].

Yet, a clear connection between properties of the surface and its macroscopic response still remains an open question [43]. Notwithstanding significant theoretical advancements, attempts to relate surface properties to macroscopic quantities, such as the dispersion coefficient and average velocity, remain mostly phenomenological [e.g. 185, 363, 199, 137] and analytical expressions are available only for tractable geometries [e.g. 174, 75].

Here, we consider non-reactive tracer transport through a symmetric (micro-)channel embedded in a permeable porous matrix, and characterize the latter by its permeability and porosity. In this work, we are concerned with analytically relating the macroscopic response of the coupled channel-matrix system, i.e., the longitudinal dispersion coefficient, with the porous layer porosity and permeability and the channel transport regimes. We assume that the flow and transport are governed by the combination of Stokes, Brinkman and advection-diffusion equations subject to

appropriate initial and boundary conditions.

This formulation, relevant to study and control transversal mixing in micro-channels, is especially suitable to model Navier-Stokes flows (both laminar and turbulent) above patterned surfaces, e.g. micro-riblets [27] and carbon nanotube forests [28, 26], where the idealization of the pattern as a porous layer has been shown appropriate.

Two approaches are routinely employed to relate channel and matrix properties to dispersion in a coupled channel-matrix system: (i) analytical and semianalytical solutions of a system of coupled advection-diffusion equations (ADEs) and (ii) up-scaling perturbative methods. While exact, analytical solutions of a system of ADEs can often be obtained only under restrictive simplifying assumptions. The greatest technical difficulty in (semi)analytically solving advection-diffusion equations is accounting for the non-uniformity of the velocity profile in the channel and/or matrix: this complication is generally overcome, or better avoided, by assuming uniform velocity in the channel, purely diffusive transport in the matrix or both. The first analytical treatment of transport mechanisms in channel-matrix systems is generally attributed to [303], who considered a one-dimensional thin channel embedded in an impermeable (to flow) porous matrix. Their result was later extended by [300] to account for the presence of neighboring parallel channels. A detailed review of this approach is provided by [40]. More recently, [269] solved semi-analytically the transport problem for a uniform flow in a two-dimensional channel embedded in an impermeable two-dimensional infinite matrix, where mass transport was purely

diffusive.

Alternative approaches to connect macroscale transport properties to surface properties are upscaling methods, such as homogenization [135, 42], volume averaging [346], thermodynamically constrained averaging [116], stochastic homogenization, the method of moments [47] etc. These approaches involve perturbative methods in various forms (single- and multiple-scale expansions, Reynolds-type decomposition, etc.), which allow rigorous derivation of the macroscale equations satisfied by spatially averaged microscale (pore-scale) quantities. The connection between the micro- and the macro-scale is formally established through effective parameters (e.g. dispersion coefficient, effective contact angle, macroscopic reaction rates, slip velocity), which depend on the specific structure of the coupled channel-matrix system. Unlike (semi)analytical solutions, these methods allow one to relax many of the assumptions concerning the shape of the velocity profile in the channel-matrix system. This is achieved at the cost of obtaining an asymptotic approximation of the full microscopic solution, generally truncated at the first or second order. In this work, we focus on perturbative approaches, since our main objective is to explicitly account for steady non-uniform flow conditions and the impact of matrix permeability on dispersion.

Since the problem of transport in a channel (with or without porous walls) has been historically handled in the context of homogenization theory, we limit our attention to the results obtained with this specific technique. We emphasize that equivalent results have been achieved with other upscaling methods. The seminal result on the upscaling of passive tracer transport in a channel with planar walls is

generally attributed to the works by [316] and [12], who, by means of perturbation methods, derived the well-known Aris-Taylor formula for the dispersion coefficient. More recently, [216] studied transport in a two-dimensional channel with reactive walls. The leading order solution was found by asymptotic homogenization and the two-dimensional solution obtained in terms of the leading order solution and its first derivative. Recently, [79] coupled a two-dimensional ADE for the channel with a one-dimensional diffusion equation for the matrix. They considered a parabolic flow profile in the channel, and applied Reynolds decomposition to obtain an upscaled equation for the average concentration. By means of Laplace transform and numerical inverse Laplace transform, they studied transport dynamics for different Péclet numbers. [118] considered transport in a cylindrical tube with a thin porous wall. In a two-domain approach, they coupled Stokes and Darcy flow by means of the Beavers and Joseph condition for the effective slip at the free fluid-porous medium interface [34]. Asymptotic analysis was used to derive the corresponding macroscopic equation and effective dispersion coefficient.

Here, we model a coupled system composed by a planar channel embedded in a porous matrix of prescribed porosity and permeability and establish an analytical relationship between the effective transport properties of the system (i.e. macroscopic dispersion coefficient), those of the porous matrix, i.e. porosity and permeability, and different transport regimes identified by the Péclet number. We also investigate the scaling behavior of the normalized dispersion in various limits and for thin and thick porous matrices.



## 2.2 Model Formulation

We consider tracer transport in a single phase fully-developed pressure-driven laminar flow in a semi-infinitely long (micro-)channel embedded in a porous matrix with permeability  $k$  and porosity  $\phi$  (Figure 2.1). While the Carman-Kozeny equation establishes a unique relationship between porosity and permeability, it is unable to describe permeability dependencies over a broad range of porous media configurations [325]. Without loss of generality, we consider porosity and permeability as independent variables in order to account for the unknown relationship between  $k$  and the microstructure arrangement. The boundaries between the channel and the matrix walls are located at  $\tilde{y} = 0$  and  $\tilde{y} = 2b$ . The porous matrix width (thickness) is  $H$ , i.e., the matrix occupies the domains  $\tilde{y} \in (2b, 2b + H)$  and  $\tilde{y} \in (-H, 0)$ . A dilute Newtonian solution with density  $\rho$  and solute concentration  $c_0$  is injected at the domain inlet  $\tilde{x} = 0$ . Flow and transport occur both in the channel and the matrix, and are affected by the momentum and mass transfer across the channel-matrix interfaces.

We denote the concentration and the  $\tilde{x}$ -component of the velocity in the channel and the matrix by  $\tilde{c}_f$ ,  $\tilde{u}_f$ ,  $\tilde{c}_m$  and  $\tilde{u}_m$ , respectively. Due to the symmetry of the domain, we restrict our analysis to  $\tilde{y} \in (-H, b)$ .

### 2.2.1 Flow Equations

Fully-developed Stokes flow in the channel-matrix system can be described by coupling the Stokes equation in the channel with a Darcy-Brinkman equation in the

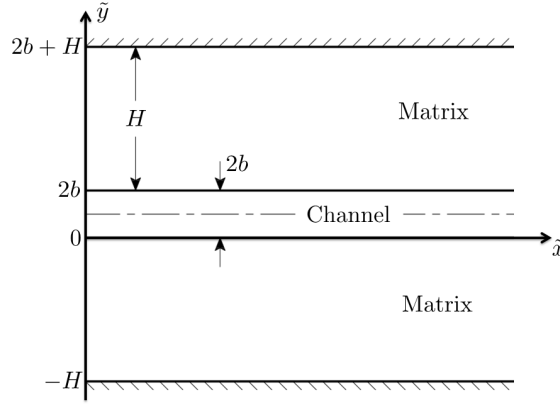


Figure 2.1: Problem domain.

matrix,

$$\mu \frac{d^2 \tilde{u}_f}{d\tilde{y}^2} - \frac{d\tilde{p}}{d\tilde{x}} = 0, \quad \tilde{y} \in (0, b), \quad (2.1a)$$

$$\mu \frac{d^2 \tilde{u}_m}{d\tilde{y}^2} - \frac{\mu}{k} \tilde{u}_m - \frac{d\tilde{p}}{d\tilde{x}} = 0, \quad \tilde{y} \in (-H, 0), \quad (2.1b)$$

respectively, where  $\tilde{u}_i(\tilde{y})$  with  $i = \{f, m\}$  is the  $\tilde{x}$ -component of the velocity in the channel and the matrix,  $\mu$  is the fluid dynamic viscosity,  $k [L^2]$  is the matrix permeability, and  $d_{\tilde{x}} \tilde{p}$  is a constant pressure gradient driving the flow in the  $\tilde{x}$ -direction. Equations (2.1) are subject to no-slip and symmetry boundary conditions at the bottom solid wall ( $\tilde{y} = -H$ ) and channel centerline ( $\tilde{y} = b$ ), respectively, and continuity of velocity and shear stress conditions at the interface separating the channel and the porous matrix ( $\tilde{y} = 0$ ),

$$\tilde{u}_m|_{\tilde{y}=-H} = 0, \quad \left. \frac{d\tilde{u}_f}{d\tilde{y}} \right|_{\tilde{y}=b} = 0, \quad \tilde{u}_f|_{\tilde{y}=0} = \tilde{u}_m|_{\tilde{y}=0}, \quad \left. \frac{d\tilde{u}_f}{d\tilde{y}} \right|_{\tilde{y}=0} = \left. \frac{d\tilde{u}_m}{d\tilde{y}} \right|_{\tilde{y}=0}. \quad (2.2)$$

While many boundary conditions have been proposed to couple free and filtration flows, see [175] for a review, continuity of velocity and shear stress has been proven accurate in a number of applications, e.g., [28, 26, 29].

We define the following dimensionless quantities:

$$x = \frac{\tilde{x}}{L}, \quad y = \frac{\tilde{y}}{b}, \quad p = \frac{\tilde{p}}{p_0}, \quad u_i = \frac{\tilde{u}_i}{U} \quad \text{with } i = \{f, m\}, \quad (2.3)$$

where  $L$  is a characteristic macroscopic/observation length scale, e.g., the distance far from the inlet where data are collected,  $p_0$  is a characteristic pressure, e.g., the ambient pressure, and  $U$  is the average velocity across the channel. Then, (2.1)-(2.2) can be cast in dimensionless form

$$\frac{d^2 u_f}{dy^2} - \Psi = 0, \quad y \in (0, 1), \quad (2.4a)$$

$$\frac{d^2 u_m}{dy^2} - \lambda^2 u_m - \Psi = 0, \quad y \in (-h, 0), \quad (2.4b)$$

subject to

$$u_m|_{y=-h} = 0, \quad \left. \frac{du_f}{dy} \right|_{y=1} = 0, \quad u_f|_{y=0} = u_m|_{y=0}, \quad \left. \frac{du_f}{dy} \right|_{y=0} = \left. \frac{du_m}{dy} \right|_{y=0}, \quad (2.5)$$

where

$$\lambda^2 = \frac{b^2}{k}, \quad \Psi = \frac{p_0 b^2}{\mu U L} \frac{dp}{dx}, \quad \text{and } h = \frac{H}{b}. \quad (2.6)$$

The system (2.4) admits an analytical solution for the velocity profiles in the channel and the matrix,  $u_f$  and  $u_m$ , respectively,

$$u_f(y) = \frac{\Psi}{2} y^2 + Ay + B, \quad y \in [0, 1], \quad (2.7)$$

$$u_m(y) = -\frac{\Psi}{\lambda^2} + Ee^{\lambda y} + Fe^{-\lambda y}, \quad y \in [-h, 0], \quad (2.8)$$

where  $A$ ,  $B$ ,  $E$  and  $F$  are integration constants

$$A = -\Psi, \quad (2.9a)$$

$$B = -\frac{\Psi}{\lambda^2} (-1 + e^\Lambda) (-1 + e^\Lambda + \lambda + \lambda e^\Lambda) (1 + e^{2\Lambda})^{-1}, \quad (2.9b)$$

$$E = -\frac{\Psi}{\lambda^2} e^\Lambda (-1 + \lambda e^\Lambda) (1 + e^{2\Lambda})^{-1}, \quad (2.9c)$$

$$F = -\frac{\Psi}{\lambda^2} (\lambda + e^\Lambda) (1 + e^{2\Lambda})^{-1}. \quad (2.9d)$$

Also,

$$\Lambda = \lambda h, \quad (2.10)$$

which represents a characteristic dimensionless length scale, also known as penetration length, associated to the thickness of the boundary layer between the free and filtration flows [224]. A classification between thin ( $\Lambda \ll 1$ ) and thick porous media ( $\Lambda \gg 1$ ) can be introduced based on the magnitude of  $\Lambda$  [26]. The slip velocity,  $U_{\text{slip}}$ , can be readily calculated as  $U_{\text{slip}} := u_m(y=0) = u_f(y=0)$ , i.e.

$$U_{\text{slip}} = -\Psi \frac{h(e^\Lambda - 1) [\Lambda(e^\Lambda + 1) + h(e^\Lambda - 1)]}{\Lambda^2(1 + e^{2\Lambda})}. \quad (2.11)$$

## 2.2.2 Transport Equations

We consider transport of a passive scalar injected at the channel inlet, i.e.,  $\tilde{x} = 0$  and  $\tilde{y} \in (0, b)$ , with concentration  $c_0$  for  $\tilde{t} > 0$ . The solute concentration in the channel

$\tilde{c}_f$  and the matrix  $\tilde{c}_m$  satisfy a system of coupled advection-dispersion equations

$$\frac{\partial \tilde{c}_f}{\partial \tilde{t}} + \tilde{u}_f \frac{\partial \tilde{c}_f}{\partial \tilde{x}} = \tilde{D}_f \left( \frac{\partial^2 \tilde{c}_f}{\partial \tilde{x}^2} + \frac{\partial^2 \tilde{c}_f}{\partial \tilde{y}^2} \right), \quad \tilde{y} \in (0, b), \quad \tilde{x}, \tilde{t} > 0, \quad (2.12a)$$

$$\frac{\partial \tilde{c}_m}{\partial \tilde{t}} + \tilde{u}_m \frac{\partial \tilde{c}_m}{\partial \tilde{x}} = \tilde{D}_{mx} \frac{\partial^2 \tilde{c}_m}{\partial \tilde{x}^2} + \tilde{D}_{my} \frac{\partial^2 \tilde{c}_m}{\partial \tilde{y}^2}, \quad \tilde{y} \in (-H, 0), \quad \tilde{x}, \tilde{t} > 0, \quad (2.12b)$$

where  $\tilde{D}_f$  is the molecular diffusion coefficient,  $\tilde{D}_{mx}$  and  $\tilde{D}_{my}$  are the  $\tilde{x}$  and  $\tilde{y}$  components of the dispersion coefficient in the matrix, and  $\tilde{u}_f = U u_f$  and  $\tilde{u}_m = U u_m$  are defined by (3.7a) and (3.7b), respectively. Equations (2.12) are subject to initial

$$\tilde{c}_f(\tilde{x}, \tilde{y}, \tilde{t} = 0) = 0 \quad \text{and} \quad \tilde{c}_m(\tilde{x}, \tilde{y}, \tilde{t} = 0) = 0, \quad (2.13)$$

and boundary conditions

$$\tilde{c}_f(0, \tilde{y} \in [0, b], \tilde{t}) = c_0, \quad \tilde{c}_f(\infty, \tilde{y} \in [0, b], \tilde{t}) = 0, \quad \frac{\partial \tilde{c}_f}{\partial \tilde{y}}(\tilde{x}, b, \tilde{t}) = 0, \quad (2.14)$$

$$\frac{\partial \tilde{c}_m}{\partial \tilde{x}}(0, \tilde{y} \in [-H, 0], \tilde{t}) = 0, \quad \tilde{c}_m(\infty, \tilde{y} \in [-H, 0], \tilde{t}) = 0, \quad \frac{\partial \tilde{c}_m}{\partial \tilde{y}}(\tilde{x}, -H, \tilde{t}) = 0. \quad (2.15)$$

Additionally, on the channel-matrix interface, the continuity of concentration and mass flux are satisfied,

$$\tilde{c}_f(\tilde{x}, 0, \tilde{t}) = \tilde{c}_m(\tilde{x}, 0, \tilde{t}) \quad \text{and} \quad \frac{\partial \tilde{c}_f}{\partial \tilde{y}}(\tilde{x}, 0, \tilde{t}) = \frac{\phi \tilde{D}_{my}}{\tilde{D}_f} \frac{\partial \tilde{c}_m}{\partial \tilde{y}}(\tilde{x}, 0, \tilde{t}), \quad (2.16)$$

where  $\phi$  is the matrix porosity. We define the following dimensionless quantities

$$t = \frac{U}{L} \tilde{t}, \quad D_f = \frac{\tilde{D}_f}{D^\star}, \quad D_{mi} = \frac{\tilde{D}_{mi}}{D^\star}, \quad c_i = \frac{\tilde{c}_i}{c_0}, \quad \text{with} \quad i = \{f, m\}. \quad (2.17)$$

Here,  $D^\star = \mathcal{O}(\tilde{D}_f)$  is the order of magnitude of the solute molecular diffusion coefficient such that  $D_f = \mathcal{O}(1)$ . Since we investigate the dynamics of transport in a time frame much larger than the diffusion time  $\tau_d = b^2/D^\star$  and close to the advection time,

$\tau_a = L/U$ , all the timescales are scaled by  $\tau_a$ . Then, Equations (2.12) can be written in dimensionless form as follows

$$\epsilon \text{Pe} \frac{\partial c_f}{\partial t} + \epsilon \text{Pe} u_f \frac{\partial c_f}{\partial x} = \epsilon^2 D_f \frac{\partial^2 c_f}{\partial x^2} + D_f \frac{\partial^2 c_f}{\partial y^2}, \quad y \in (0, 1), \quad x, t > 0, \quad (2.18a)$$

$$\epsilon \text{Pe} \frac{\partial c_m}{\partial t} + \epsilon \text{Pe} u_m \frac{\partial c_m}{\partial x} = \epsilon^2 D_{mx} \frac{\partial^2 c_m}{\partial x^2} + D_{my} \frac{\partial^2 c_m}{\partial y^2}, \quad y \in (-h, 0), \quad x, t > 0, \quad (2.18b)$$

where

$$\epsilon = \frac{b}{L}, \quad \text{and} \quad \text{Pe} = \frac{\tau_d}{\tau_a} = \frac{Ub}{D^*}. \quad (2.19)$$

Equations (2.18) are subject to

$$c_f(0, y \in [0, 1], t) = 1, \quad c_f(\infty, y \in [0, 1], t) = 0, \quad \frac{\partial c_f}{\partial y}(x, 1, t) = 0, \quad (2.20)$$

$$\frac{\partial c_m}{\partial x}(0, y \in [-h, 0], t) = 0, \quad c_m(\infty, y \in [-h, 0], t) = 0, \quad \frac{\partial c_m}{\partial y}(x, -h, t) = 0, \quad (2.21)$$

$$c_f(x, 0, t) = c_m(x, 0, t) \quad \text{and} \quad \frac{\partial c_f}{\partial y}(x, 0, t) = \frac{\phi D_{my}}{D_f} \frac{\partial c_m}{\partial y}(x, 0, t). \quad (2.22)$$

In the following section, we employ asymptotic homogenization to relate dispersion coefficient in the coupled channel-matrix system with the effective properties of the matrix.

## 2.3 Homogenization and Upscaled Equations

To derive the upscaled transport equations, we apply rescaling and asymptotic analysis to the ADEs (2.18). We introduce the rescaled longitudinal coordinate  $\xi$  and a coefficient  $\alpha$  such that

$$x := \xi \sqrt{\epsilon}, \quad \text{and} \quad \text{Pe} := \epsilon^{-\alpha}. \quad (2.23)$$

Equations (2.18a) and (2.18b) take the form

$$\epsilon \text{Pe} \left( \frac{\partial c_f}{\partial t} + \frac{u_f}{\sqrt{\epsilon}} \frac{\partial c_f}{\partial \xi} \right) = \epsilon D_f \frac{\partial^2 c_f}{\partial \xi^2} + D_f \frac{\partial^2 c_f}{\partial y^2}, \quad (2.24a)$$

$$\epsilon \text{Pe} \left( \frac{\partial c_m}{\partial t} + \frac{u_m}{\sqrt{\epsilon}} \frac{\partial c_m}{\partial \xi} \right) = \epsilon D_{mx} \frac{\partial^2 c_m}{\partial \xi^2} + D_{my} \frac{\partial^2 c_m}{\partial y^2}. \quad (2.24b)$$

Let us define the cross-sectional averaging operator

$$\langle \cdot \rangle = \frac{1}{L^*} \int_0^{L^*} \cdot \, dy, \quad (2.25)$$

where  $L^* = 1$  for the channel and  $L^* = -h$  for the matrix. Also, we employ the *ansatz*

$$c_i = c_i^{(0)}(\xi, t) + \sqrt{\epsilon} c_i^{(1)}(\xi, y, t) + \epsilon c_i^{(2)}(\xi, y, t) + \mathcal{O}(\epsilon\sqrt{\epsilon}), \quad i = \{f, m\}, \quad (2.26)$$

where  $c_i^{(j)}$  is the  $j^{\text{th}}$ -order term in the expansion of concentration  $c_i$ . Substituting (2.26)

in (2.24) while applying the averaging operator (2.25) leads to a system of coupled

upscaled (effective, macroscopic) equations (see Appendix)

$$\epsilon^2 \text{Pe} \left( \frac{\partial \langle c_f \rangle}{\partial t} + \langle u_f \rangle \frac{\partial \langle c_f \rangle}{\partial x} \right) = \epsilon^3 D_f^* \frac{\partial^2 \langle c_f \rangle}{\partial x^2} - \phi \left[ \epsilon^2 \text{Pe} N_1 \frac{\partial \langle c_m \rangle}{\partial x} + \frac{3D_{my}}{h} (\langle c_f \rangle - \langle c_m \rangle) \right], \quad (2.27a)$$

$$\epsilon^2 \text{Pe} \left( \frac{\partial \langle c_m \rangle}{\partial t} + \langle u_m \rangle \frac{\partial \langle c_m \rangle}{\partial x} \right) = \epsilon^3 D_m^* \frac{\partial^2 \langle c_m \rangle}{\partial x^2} + \frac{1}{\phi} \left[ \epsilon^2 \text{Pe} \frac{M_1}{h} \frac{\partial \langle c_f \rangle}{\partial x} + \frac{3D_f}{h} (\langle c_f \rangle - \langle c_m \rangle) \right], \quad (2.27b)$$

where

$$M_1 = -\left( \frac{\Psi}{6} + \frac{A}{2} + B \right) \quad \text{and} \quad N_1 = \frac{\Psi h}{\lambda^2} - \frac{F}{\lambda} (e^{\lambda h} - 1) + \frac{E}{\lambda} (e^{-\Lambda} - 1). \quad (2.28)$$

subject to

$$\langle c_f \rangle(x=0, t) = 1, \quad \langle c_f \rangle(x=\infty, t) = 0, \quad \langle c_f \rangle(x, t=0) = 0, \quad (2.29)$$

$$\frac{\partial \langle c_m \rangle}{\partial x}(x=0, t) = 0, \quad \langle c_m \rangle(x=\infty, t) = 0, \quad \langle c_m \rangle(x, t=0) = 0, \quad (2.30)$$

under the assumption that  $\langle c_i^{(1)} \rangle = \langle c_i^{(2)} \rangle = 0$ ,  $i = \{f, m\}$ , and provided the conditions

1.  $\epsilon \ll 1$ ,
2.  $Pe < \epsilon^{-1/2}$ ,

are met. Condition (1) ensures that geometric scales separation exists and is satisfied when the channel is long and thin. Condition (2) provides an upper bound on the Péclet number. To ensure the higher order correction terms have zero mean, we set  $\langle c_i^{(1)} \rangle = \langle c_i^{(2)} \rangle = 0$  [216].

The advection dispersion equations (3.6) are coupled through a source term describing the mass exchange between the matrix and the channel. Unlike existing works [266, 149], that postulated the coupling in the form of a storage term only, i.e.  $(\langle c_f \rangle - \langle c_m \rangle)$ , our analysis demonstrates that an additional contribution due to concentration gradients along the channel, i.e.  $\partial \langle c_i \rangle / \partial x$ ,  $i = \{m, f\}$ , must be considered as well. We emphasize that the flux  $\partial \langle c_m \rangle / \partial x$  is an advective term contributed by the non-zero permeability matrix. This is different from [303], [79] or [269], who only consider diffusive transport in the porous medium.

In (3.6),  $D_f^*$  and  $D_m^*$  are the dispersion coefficients for the channel and the matrix, respectively. The channel dispersion coefficient  $D_f^*$  is defined as

$$D_f^* = D_f + Pe^2 \frac{I_f}{D_f}, \quad (2.31)$$

or, equivalently and without loss of generality,

$$D_f^* = 1 + Pe^2 I_f, \quad (2.32)$$



if  $D^* \equiv \tilde{D}_f$  and  $D_f \equiv 1$  in (2.24) and (2.31), respectively. In the following, we will use the second expression (2.32) (i.e.  $D_f \equiv 1$ ) as it allows a direct comparison with formulas derived by other authors [134, 118, 79]. In (2.32),  $I_f = \frac{3}{560}\Psi^2 + \frac{1}{40}A\Psi + \frac{7}{360}B\Psi + \frac{7}{240}A^2 + \frac{1}{24}AB$ , i.e.

$$I_f = \frac{\Psi^2}{105} [1 + g(\lambda, \Lambda)] \quad (2.33)$$

where

$$g(\lambda, \Lambda) = \frac{7(e^\Lambda - 1)[e^\Lambda - 1 + \lambda(1 + e^\Lambda)]}{3\lambda^2(1 + e^{2\Lambda})} \quad (2.34)$$

or, equivalently,

$$g(\lambda, \Lambda) = \frac{7}{3\lambda} \left[ \tanh\Lambda + \frac{1}{\lambda}(1 - \operatorname{sech}\Lambda) \right]. \quad (2.35)$$

Also, from (2.11) it is immediate to show that

$$\frac{U_{\text{slip}}}{\Psi} = -\frac{3}{7}g(\lambda, \Lambda), \quad (2.36)$$

i.e. the normalized interfacial velocity  $-U_{\text{slip}}/\Psi$  is solely controlled by the porous matrix properties.

We emphasize that  $D_f^*$  explicitly depends on  $\lambda$  (inverse of the dimensionless permeability) through  $I_f$ . The matrix dispersion coefficient is

$$D_m^* = D_{mx} - \text{Pe}^2 \frac{I_m}{D_{my}}, \quad (2.37)$$

where

$$I_m = \frac{1}{h} \int_{-h}^0 u_m(y) N(y) dy, \quad (2.38)$$

and

$$N(y) = \int_0^y dy' \int_0^{y'} u_m(y^*) dy^*, \quad 0 < y^* < y', \quad 0 < y' < y. \quad (2.39)$$

The derivation details are presented in Appendix.

## 2.4 Dispersion Coefficient and Matrix Properties

In order to investigate the impact of matrix effective properties,  $h$  and  $\lambda$ , on macroscale transport in the channel, we compare  $D_f^*$  in (2.32) with the dispersion coefficient  $D_d$  obtained by [79] for a coupled system with purely diffusive transport in the matrix (i.e.  $\lambda \rightarrow \infty$  or  $k \rightarrow 0$ , and  $h \neq 0$ ). To isolate the effect of the width of the porous medium and its permeability,  $h$  and  $\lambda$ , on channel macroscopic transport, we normalize both coefficients by the Aris-Taylor dispersion coefficient  $D_{AT}$  for a single channel (i.e.  $\lambda \rightarrow \infty$  or  $k \rightarrow 0$ , and  $h = 0$ ) and define

$$\kappa_f := \frac{D_f^*}{D_{AT}} \quad \text{and} \quad \kappa_d := \frac{D_d}{D_{AT}} \quad (2.40)$$

where [79, 134]

$$D_d = 1 + \frac{1}{175} \text{Pe}^2 \quad \text{and} \quad D_{AT} = 1 + \frac{2}{105} \text{Pe}^2. \quad (2.41)$$

In Figure 2.2, we plot  $\kappa_f$  and  $\kappa_d$  as a function of  $\text{Pe}$  and  $\lambda$ , for a fixed  $h$ . It shows that two thresholds exist such that  $\kappa_f$  is constant for  $\text{Pe} < \text{Pe}_{\min}$  and  $\text{Pe} > \text{Pe}^*$ . For small Péclet number ( $\text{Pe} < \text{Pe}_{\min} \approx 1$ ),  $\kappa_f \rightarrow \kappa_d$ , i.e., the dispersion coefficient for the coupled system with permeable matrix (finite  $\lambda$ ) converges to its non-permeable

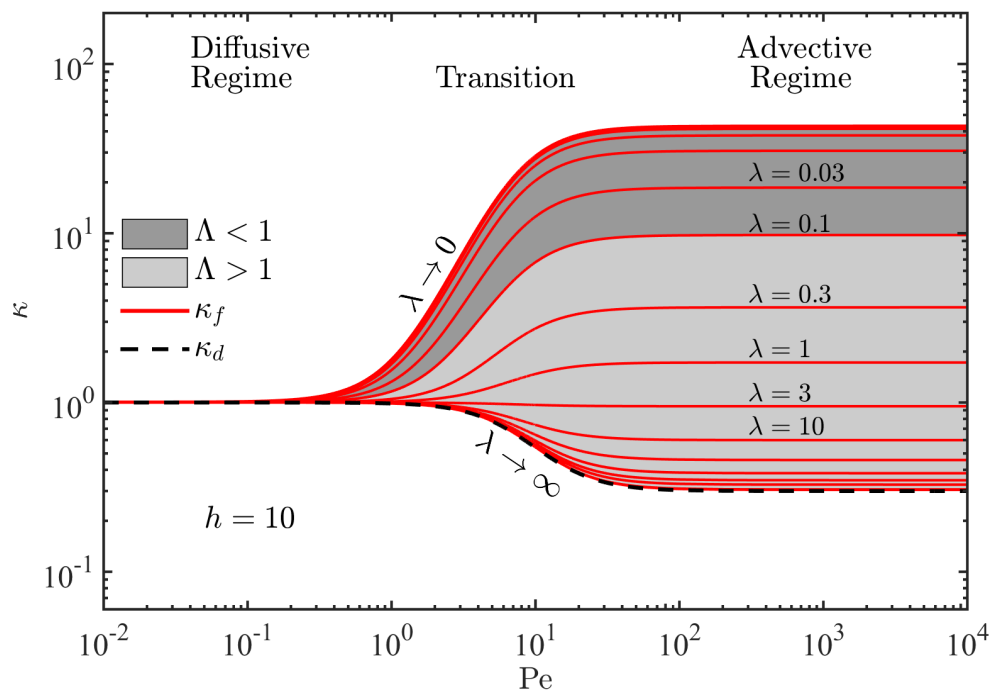


Figure 2.2: Normalized dispersion coefficients  $\kappa_f$  (solid red lines) and  $\kappa_d$  (dashed back line) versus  $Pe$  for different values of  $\lambda$  and  $\Lambda$ . Also,  $\Psi = -0.78$  and  $h = 10$ .

matrix limit ( $\lambda \rightarrow \infty$ ,  $h \neq 0$ ) independent of  $h$  and  $\lambda$ . When  $Pe < 1$ , advective mixing both in the matrix and channel is negligible relative to diffusive mixing. As a result,  $\kappa_f \rightarrow \kappa_d$  and  $\kappa_d \rightarrow 1$ . In the intermediate range of Péclet numbers ( $1 < Pe < Pe^*$ ),  $\kappa_f$  changes from  $\kappa_f = 1$ , to  $\kappa_f = \kappa_f(\lambda, h)$  when  $Pe > Pe^*$ . It is worth noticing that the dispersion coefficient can overcome its purely diffusive limit when  $\lambda < 1$ , i.e. mixing is enhanced compared to a channel of halfwidth  $b$ . When  $1 < Pe < Pe^*$ ,  $\kappa_f$  is a function of  $Pe$ ,  $h$  and  $\lambda$ . Therefore, the matrix properties (or  $\lambda$  and  $h$ ) and boundary conditions (or  $Pe$ ) can be independently modified to achieve the desired dispersion coefficient.

As mentioned above, for large Péclet number ( $Pe > Pe^*$ ),  $\kappa_f$  reaches a  $Pe$  independent asymptotic value  $\kappa_{\lambda, h}$ , i.e.  $\lim_{Pe \rightarrow \infty} \kappa_f = \kappa_{\lambda, h}$ . In this regime, for any given  $Pe$ , the dispersion coefficient increases with decreasing  $\lambda$  (Figure 2.2). This phenomenon is attributed to a decreasing mass flux at the interface between the channel and the matrix, and a resulting decreasing mass loss toward the matrix. Such mass loss is smaller compared with the zero-permeability case, where no solute is transported from the upper steam by the flow in the matrix. This is a newly identified mechanism regulating mass exchange between the channel and the matrix, which is purely controlled by the matrix properties ( $\lambda$  and  $h$ ) at fixed operating conditions (i.e., constant Péclet number). This mechanism is different from the mass transfer mechanism first proposed by [360] and then quantified by [79], where the channel-matrix interface flux increases (and dimensionless dispersion coefficient  $\kappa_d$  decreases) with increasing Péclet number and is independent of matrix properties  $\lambda$  and  $h$ . In the zero permeability limit, i.e.,  $\lambda \rightarrow \infty$ , and for fixed  $Pe$ ,  $\kappa_f \rightarrow \kappa_d$ , as expected. In the following, we focus on the study

of the dispersion coefficient in the matrix only  $\kappa_f$ , since it is deemed more relevant to many engineering applications where transversal mixing enhancement in the channel is the primary target.

Threshold value and scaling for thin and thick porous matrices We aim to identify the scaling behavior of  $\kappa_f$  in different regimes, if it exists. Combining (2.33) and (2.32) with (2.40), leads to

$$\kappa_f = 105 \frac{1 + \text{Pe}^2 I_f}{105 + 2\text{Pe}^2} \quad (2.42)$$

with  $I_f$  given by (2.33). We define  $\kappa_{f,\text{Pe} \rightarrow 0}$  and  $\kappa_{f,\lambda \rightarrow \infty}$  as the fracture dimensionless dispersion coefficients in the two purely diffusive limits:  $\text{Pe} \rightarrow 0$  for any  $\lambda$ , and  $\lambda \rightarrow \infty$  for any  $\text{Pe}$ , respectively. The coefficient  $\kappa_{f,\text{Pe} \rightarrow 0}$  corresponds to the scenario where mass transport in the matrix is driven solely by diffusion since  $\text{Pe} = 0$ ;  $\kappa_{f,\lambda \rightarrow \infty}$  corresponds to the case of diffusive transport in an impermeable matrix. The latter differs from Aris-Taylor dispersion in that the channel-porous interface is impermeable to flow, but permeable to mass. If  $\text{Pe} \rightarrow 0$ ,  $D_f^* = 1$  and

$$\kappa_{f,\text{Pe} \rightarrow 0} := \frac{\lim_{\text{Pe} \rightarrow 0} D_f^*}{D_{\text{AT}}} = \frac{105}{105 + 2\text{Pe}^2}. \quad (2.43)$$

Since  $\Lambda \rightarrow \infty$  when  $\lambda \rightarrow \infty$  for  $h \neq 0$ , then

$$\kappa_{f,\lambda \rightarrow \infty} := \frac{\lim_{\lambda \rightarrow \infty} D_f^*}{D_{\text{AT}}} = \frac{105 + \text{Pe}^2 \Psi^2}{105 + 2\text{Pe}^2}. \quad (2.44)$$

Combining (2.43) and (2.44) with (2.42), leads to the following expression for  $\kappa_f$ ,

$$\kappa_f = \kappa_{f,\text{Pe} \rightarrow 0} + g(\Lambda, \lambda) \cdot (\kappa_{f,\lambda \rightarrow \infty} - \kappa_{f,\text{Pe} \rightarrow 0}), \quad (2.45)$$

where  $g(\Lambda, h)$  is defined in (2.35). In order to isolate the dependence of  $\kappa_f$  from the matrix properties,  $\lambda$  and  $h$ , we define the normalized dimensionless dispersion coefficient  $\Pi$

$$\Pi := \frac{\kappa_f - \kappa_{f, \text{Pe} \rightarrow 0}}{\kappa_{f, \lambda \rightarrow \infty} - \kappa_{f, \text{Pe} \rightarrow 0}} \quad (2.46)$$

which satisfies

$$\Pi = g(\Lambda, \lambda) = -\frac{7}{3} \frac{U_{\text{slip}}}{\Psi}, \quad (2.47)$$

i.e. it is independent of Pe number. It is worth noticing that  $\Pi$  scales as  $U_{\text{slip}}$  normalized by  $\Psi$ . In Figure 2.2,  $\kappa_f$  reaches a Pe-independent threshold when  $\text{Pe} \rightarrow \infty$ . Since  $\lim_{\text{Pe} \rightarrow \infty} (\kappa_{f, \text{Pe} \rightarrow 0}) = 0$  and  $\lim_{\text{Pe} \rightarrow \infty} (\kappa_{f, \lambda \rightarrow \infty}) = \Psi^2/2$ , then

$$\lim_{\text{Pe} \rightarrow \infty} \kappa_f \sim \lim_{\text{Pe} \rightarrow \infty} \Pi. \quad (2.48)$$

From (2.47), we obtain

$$\kappa_f^{\text{threshold}} = \lim_{\text{Pe} \rightarrow \infty} \kappa_f = -\frac{7\Psi}{6} U_{\text{slip}} = \frac{\Psi^2}{2} \Pi, \quad (2.49)$$

i.e. in the advective limit the dispersion coefficient is controlled by the slip velocity at the interface between the porous matrix and the channel.

In the following, we study the scaling behaviour of  $\Pi$  (or  $U_{\text{slip}}/\Psi$ ) for thin ( $\Lambda \ll 1$ ) and thick ( $\Lambda \gg 1$ ) porous matrices.

#### 2.4.1 Thin porous matrix limit, $\Lambda \ll 1$

The asymptotic expansion of (2.47) about  $\Lambda = 0$ , leads to

$$\Pi = \frac{7}{3} \left[ \left( h + \frac{h^2}{2} \right) - \left( \frac{h}{3} + \frac{5h^2}{24} \right) \Lambda^2 + O(\Lambda^5) \right]. \quad (2.50)$$

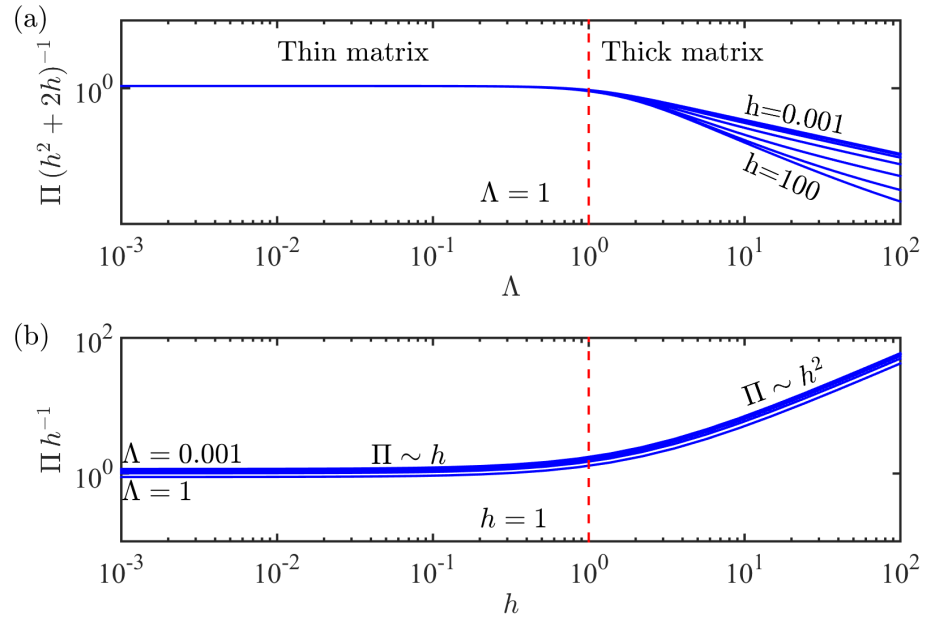


Figure 2.3: (a) Scaling behavior of the normalized dispersion coefficient  $\Pi$  defined in (2.46) for thin porous media ( $\Lambda \lesssim 1$ ) and (b)  $h < 1$  and  $h > 1$ . The coefficient  $\Pi$ , i.e. transverse dispersion, is controlled by the width  $h$  of the porous matrix when  $\Lambda \lesssim 1$ ; this dependence goes from linear to quadratic as  $h$  increases above the threshold  $h \approx 1$ .

since  $\tanh\Lambda \approx \Lambda - \Lambda^3/3 + O(\Lambda^5)$  and  $\operatorname{sech}\Lambda \approx 1 - \Lambda^2/2 + 5\Lambda^4/24 + O(\Lambda^6)$ . Retaining the leading order term, we obtain

$$\Pi \sim h \left(1 + \frac{h}{2}\right), \quad \text{for } \Lambda \ll 1, \quad (2.51)$$

which shows that dispersion is controlled by the matrix thickness  $h$  for thin porous layers. Figure 2.3(a) shows the scaling behavior of  $\Pi(h^2 + 2h)^{-1}$  versus  $\Lambda$  and suggests that the scaling (2.51) be a valid approximation for  $\Lambda \rightarrow 1$  as well, i.e.

$$\Pi \sim h \left(1 + \frac{h}{2}\right), \quad \text{for } \Lambda \lesssim 1. \quad (2.52)$$

Further, two scaling regimes exist for  $h \ll 1$  and  $h \gg 1$ , i.e.

$$\Pi \sim h, \quad \text{for } \Lambda \lesssim 1, \quad h \ll 1 \quad (2.53a)$$

$$\Pi \sim h^2, \quad \text{for } \Lambda \lesssim 1, \quad h \gg 1 \quad (2.53b)$$

In Figure 2.3(b), we plot  $\Pi h^{-1}$  as a function of  $h$  for different  $\Lambda \in [0.001, 1]$ . As expected  $\Pi h^{-1}$  is constant when  $h \ll 1$  and grows linearly with  $h$  when  $h \gg 1$ . This result suggests that transversal mixing in a channel with a thin porous coating ( $\Lambda \ll 1$ ) is controlled by  $h$ , and is more sensitive to the matrix width when  $h \gg 1$ , i.e. for a given increase in  $H$ ,  $\Delta H$ , better mixing can be achieved if  $H > b$ .

## 2.4.2 Thick porous matrix limit, $\Lambda \gg 1$

In the limit  $\Lambda \gg 1$ , i.e. for thick porous matrices, we expand (2.47) about  $1/\Lambda = 0$  and obtain

$$\Pi = \frac{7}{3} \frac{(h\Lambda^{-1} + h^2\Lambda^{-2})e^{2\Lambda} - h^2\Lambda^{-2}e^\Lambda - h\Lambda^{-1}}{1 + e^{2\Lambda}} + O(\Lambda^{-2}), \quad (2.54)$$



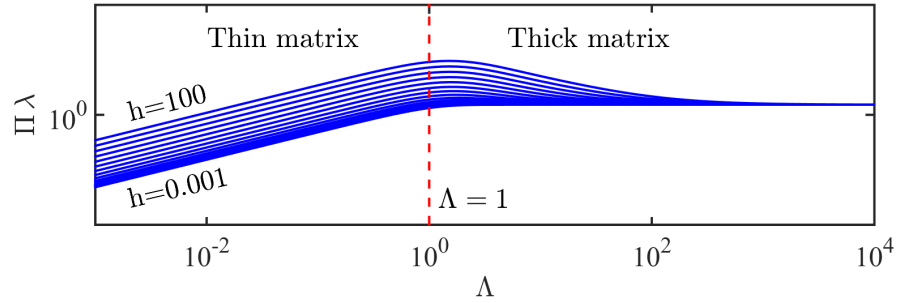


Figure 2.4: Scaling behavior of the normalized dispersion coefficient  $\Pi$  defined in (2.46) for thick porous media ( $\Lambda \gg 1$ ). The normalized dispersion coefficient is controlled by matrix permeability only, when  $\Lambda \gg 1$ .

since  $e^\Lambda(1 + e^{2\Lambda})^{-1} \rightarrow 0$  and  $e^{2\Lambda}(1 + e^{2\Lambda})^{-1} \rightarrow 1$  when  $\Lambda \rightarrow \infty$ . At the leading order

$$\Pi \sim \frac{1}{\lambda}, \quad \text{for } \Lambda \gg 1, \quad (2.55)$$

i.e. the normalized dispersion is controlled by matrix permeability only. Figure 2.4 shows that  $\Pi\lambda$  reaches a  $\Lambda$ -independent value for  $\Lambda \gg 1$ , as suggested by (2.55). This analysis shows that when increasing the thickness of the matrix for a given  $\lambda$ , further increments of  $h$  will no longer affect the slip velocity when  $\Lambda \gg 1$ . In this regime, the bottom wall of the matrix (located at  $y = -h$ ) becomes “invisible” to the flow and transport in the channel, and changes in  $h$  will not influence the channel dynamics. For a given channel-matrix system with  $\Lambda \gg 1$  an effective control of the dispersion can be achieved by modifying the permeability of the porous medium.

## 2.5 Validation and Model Accuracy: Numerical Experiments

The system (3.6) is composed of two one-dimensional transient coupled up-scaled equations. The coupling is due to the mass exchange at the interface between the channel and the matrix. Here, we solve the coupled system (3.6) numerically. We test the accuracy of the upscaling approximation (3.6a) and (3.6b) by comparison with the averaged 2D solution obtained from numerically solving (2.18a) and (2.18b).

### 2.5.1 Code validation

For the discretization of the 1D equations (3.6), we use implicit Euler in time and second-order central finite differences discretization in space. For the 2D equations (2.18), we use backward Euler for the time discretization and second-order discretization in space, with upwinding for the advective term and central finite differences for the other terms. A convergence study is performed on the 1D solver by refining the grid size and time step. We validate the 2D solver by setting  $\phi = 1$ ,  $D_f = D_{mx} = D_{my}$  and  $u_f = u_m = u^*$  in (2.18). This corresponds to passive transport in a single channel (and no porous medium) with uniform velocity  $u^*$  for which a closed form analytical solution is available [233]. We compare the numerical average of the pore-scale concentration  $c_f$  with the analytical solution for the continuous injection

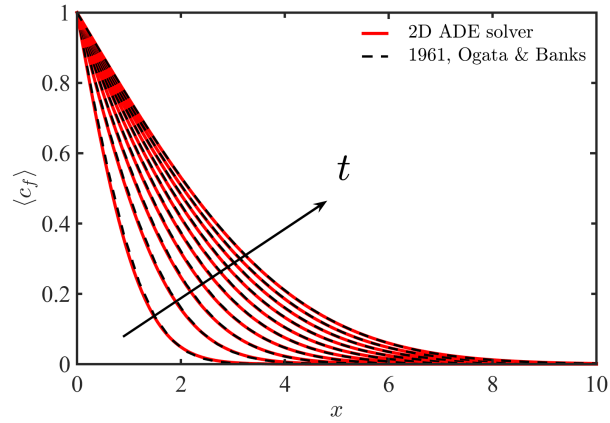


Figure 2.5: Comparison between the averaged 2D concentration in the channel and the 1D analytical solution, equation (2.56) [233], for passive scalar transport in a single channel with uniform velocity and constant injection. The average concentration  $\langle c_f \rangle$  is plotted in terms of the dimensionless distance from the channel inlet at different instances in time  $\tilde{t}$ .  $h = 10$ ,  $\phi = 1$ ,  $\epsilon = 0.01$ ,  $D_f = D_{mx} = D_{my} = 1$  and  $u_f = u_m = u^* = 0.01$ .

of a passive solute. The mean concentration profile satisfies [233]

$$\langle c_f \rangle(x, t) = \frac{1}{2} \left[ \operatorname{erfc} \left( \frac{x - u^* t}{2\sqrt{D_f t}} \right) + \exp \left( \frac{u^* x}{D_f} \right) \operatorname{erfc} \left( \frac{x + u^* t}{2\sqrt{D_f t}} \right) \right]. \quad (2.56)$$

Figure 2.5 shows the match between the numerically upscaled 2D concentration and the analytical solution (2.56).

## 2.5.2 Upscaled Model's Accuracy and Predictivity

We verify the accuracy of the upscaling procedure by comparing the macroscale concentrations  $\langle c_f \rangle_{1D}$  and  $\langle c_m \rangle_{1D}$  obtained from (3.6) with the numerical averages

of the microscale two-dimensional concentrations obtained from (2.18),  $\langle c_f \rangle_{2D}$  and  $\langle c_m \rangle_{2D}$ . The upscaled model (3.6) is considered predictive of pore-scale behavior if the absolute error between upscaled and microscale quantities is bounded by  $\sqrt{\epsilon}$ , as prescribed by the homogenization procedure. All parameters in the 2D pore-scale equations are uniquely mapped onto the effective parameters of the corresponding macroscopic system.

Without loss of generality, we consider a continuous injection at the channel inlet, i.e.  $c_f(x = 0, y, t) = 1$  and  $\partial_x c_m(x = 0, y, t) = 0$ . This corresponds to the inlet boundary conditions  $\langle c_f \rangle(x = 0, t) = 1$  and  $\partial_x \langle c_m \rangle(x = 0, t) = 0$  in the upscaled model.

In Figure 2.6, we compare the averaged fully-resolved two-dimensional and the upscaled approximated solutions  $\langle c_f \rangle_{2D}(x, t)$  and  $\langle c_f \rangle_{1D}(x, t)$ , respectively, for different values of Péclet,  $Pe = \{0.1, 10, 100, 1000\}$ , and porosity,  $\phi = \{0.01, 0.1\}$ , and plot the absolute error  $E_f(x, t) := |\langle c_f \rangle_{2D} - \langle c_f \rangle_{1D}|$ . The simulations in Figure 2.6 are run for  $\epsilon = 0.02$ ,  $\lambda = 10$  and  $\phi = 0.1$ . As predicted, the 1D equations capture the pore-scale dynamics within errors of order  $\sqrt{\epsilon}$  for  $Pe < \epsilon^{-1/2} \approx 7$ . Importantly, for  $10 < Pe < 100$ , the 1D simulation is still accurate. For  $Pe = 1000$ , the error is not bounded by  $\sqrt{\epsilon}$  at early times, but the 1D model's accuracy is recovered at later times. The simulations parameters are  $\epsilon = 0.02$ ,  $\lambda = 10$ ,  $\Psi = -0.78$ ,  $\phi = 0.1$ ,  $D_f = 1$ ,  $D_{mx} = 0.1$ ,  $D_{my} = 0.1$ ,  $h = 10$ .

In Figure 2.6, we show that the absolute error between the 2D and the 1D models decreases with increasing time and distance from the inlet for all scenarios. More specifically, the macroscopic 1D model performs within the expected accuracy

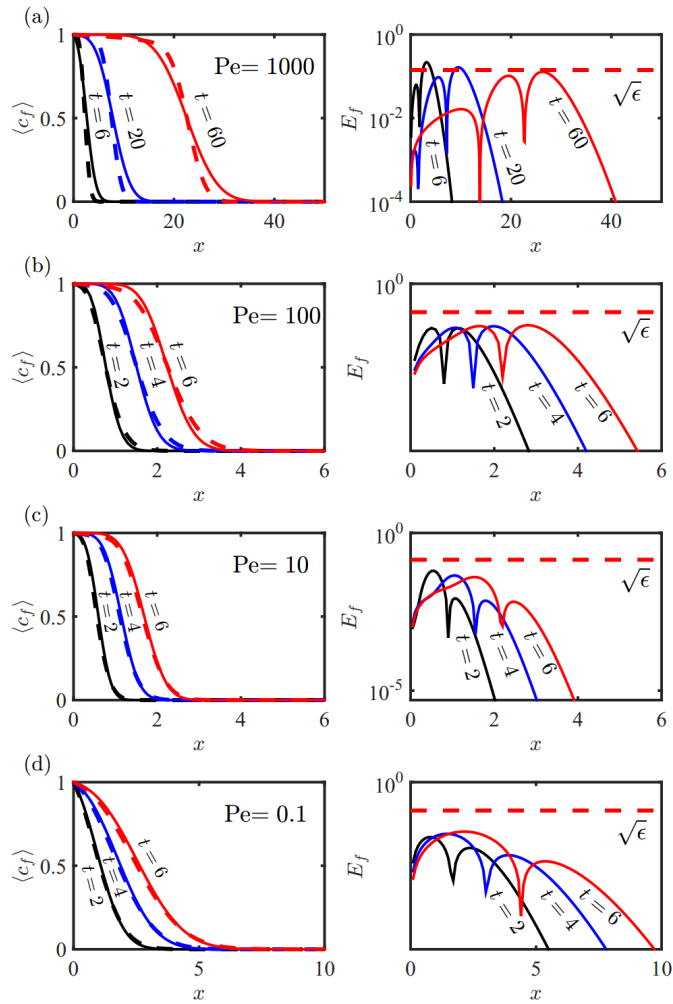


Figure 2.6: (Left) Average concentration profiles  $\langle c_f \rangle$  along the channel obtained either from the upscaled 1D (solid lines) or the pore-scale 2D equations (dashed lines) for different instances in time and Péclet numbers, i.e.  $Pe = \{0.1, 10, 100, 1000\}$ . (Right) Absolute error  $E_f(x, t) := |\langle c_f \rangle_{2D} - \langle c_f \rangle_{1D}|$  corresponding to each simulation. The dashed horizontal line represents the error bound  $\sqrt{\epsilon}$  prescribed by homogenization theory.

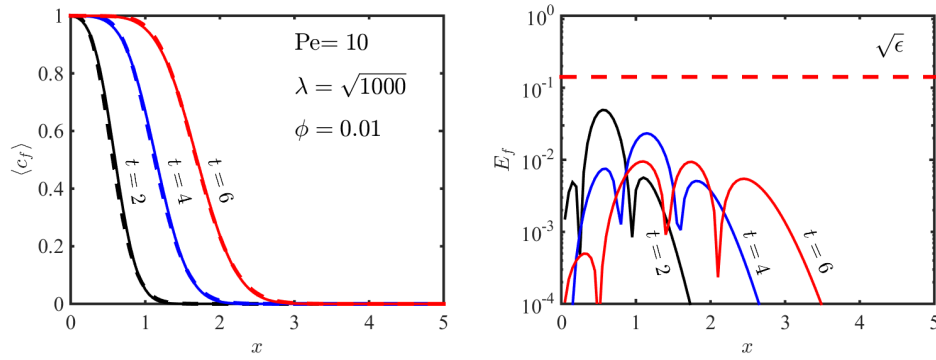


Figure 2.7: Simulation parameters:  $\epsilon = 0.02$ ,  $\lambda = 31.6$ ,  $\phi = 0.1$ ,  $\Psi = -0.78$ ,  $D_f = 1$ ,  $D_{m_x} = 0.1$ ,  $D_{m_y} = 0.1$ ,  $h = 10$ . (Left) Average concentration profiles  $\langle c_f \rangle$  along the channel obtained either from the upscaled 1D (solid lines) or the pore-scale 2D equations (dashed lines) for different instances in time. (Right) Absolute error  $E_f(x, t) := |\langle c_f \rangle_{2D} - \langle c_f \rangle_{1D}|$  corresponding to each simulation. The dashed horizontal line represents the error bound  $\sqrt{\epsilon}$  prescribed by homogenization theory.

for  $Pe < \epsilon^{-1/2}$  ( $\approx 7$  for  $\epsilon = 0.02$ ), i.e.  $E_f(x, t)$  is bounded by  $\sqrt{\epsilon}$ , see Figure 2.6(d). The error bound is satisfied even when the constraints on the Péclet number are relaxed, i.e.  $\mathcal{O}(\epsilon^{-1/2}) \leq Pe \leq \mathcal{O}(\epsilon^{-1})$ , or  $10 \leq Pe \leq Pe^*$  in Figures 2.6(b) and (c). This result highlights that the conditions (1) and (2) are sufficient, but not necessary, to guarantee that error bounds prescribed by homogenization theory are realized. For  $Pe > \mathcal{O}(\epsilon^{-1})$  (or  $Pe > Pe^*$ ),  $E_f(x, t) > \sqrt{\epsilon}$  for early times; the 1D model regains its accuracy at late (dimensionless) times  $t > \epsilon Pe$ , i.e.  $t > 20$  in Figure 2.6(a).

In Figure 2.7, we plot the profiles of the average concentration in the channel obtained from the numerically averaged 2D equations and the 1D upscaled equations. The simulations are run for  $\lambda = 31.6$  and  $\phi = 0.1$ . The error between the microscale

and the macroscale equations, Figure 2.7(right), is lower compared to the scenario with the same Péclet number and higher permeability and porosity, specifically Figure 2.6(c). This is consistent with the upscaling approach, where higher-order terms in the transverse direction are neglected, thus leading to increased error for highly permeable matrix.

To further investigate the accuracy of the upscaled equations in different regimes and the temporal dependence of the error, we plot the solute breakthrough curves at a given location  $x = x^*$  along the channel.

In Figure 2.8, we plot the concentration profile for three Péclet numbers and two values of dimensionless permeability,  $\lambda = \sqrt{10^2}$  and  $\lambda = \sqrt{10^3}$ . For  $Pe \ll 1$ , there is an excellent agreement between the upscaled and two-dimensional solutions for all times and both permeability values. The match is within the expected error bounds, Figure 2.8, top. For higher Péclet numbers,  $Pe = 1$  (Figure 2.8, middle) and  $Pe = 1000$  (Figure 2.8, bottom), the upscaled solution can still capture the averaged pore-scale concentration despite condition (2) is violated for  $Pe = 1000$ . Good performance of the model in regimes where (2) is violated can be expected since such a constraint is simply a sufficient (and not necessary) condition to guarantee that the upscaled equation (3.6) describe spatially averaged pore-scale processes within errors of order  $\sqrt{\epsilon}$ . For  $Pe = 1000$  the match between the upscaled and the averaged pore scale solution improves at later times. Since condition (2) is violated, the transient terms in the expansion, specifically  $\partial_t c_f^{(0)}$  and  $\partial_t c_m^{(0)}$ , in (A.3a), are not negligible and should be accounted for at the leading order. Failing to do so yields to a slightly higher

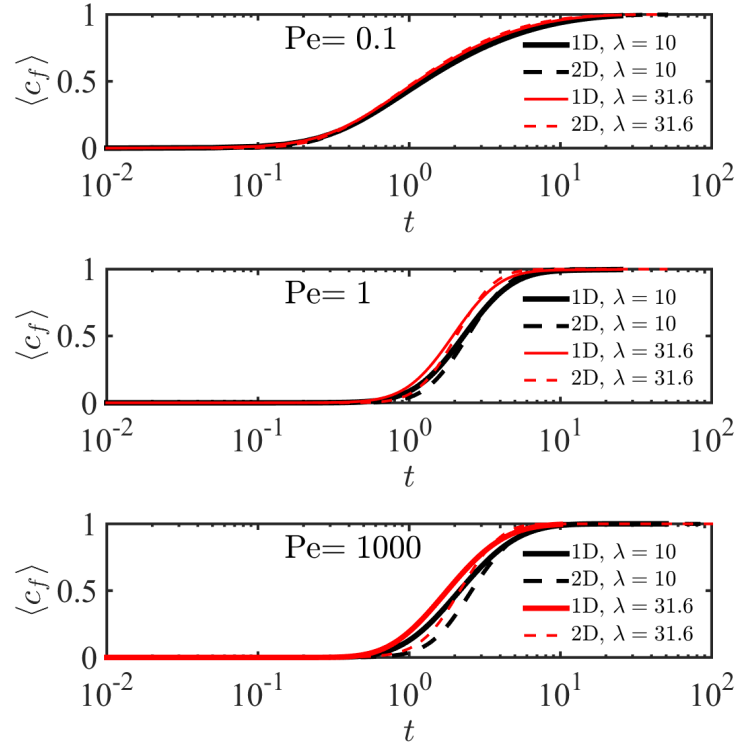


Figure 2.8: Time evolution of the channel average concentration  $\langle c_f \rangle$  calculated at location  $x^* = b$  for different  $\lambda$  and Péclet numbers. The parameters used in the simulations are  $\phi = 0.01$ ,  $\Psi = -0.78$ ,  $\epsilon = 0.01$ ,  $D_f = 1$ , and  $h = 10$ .



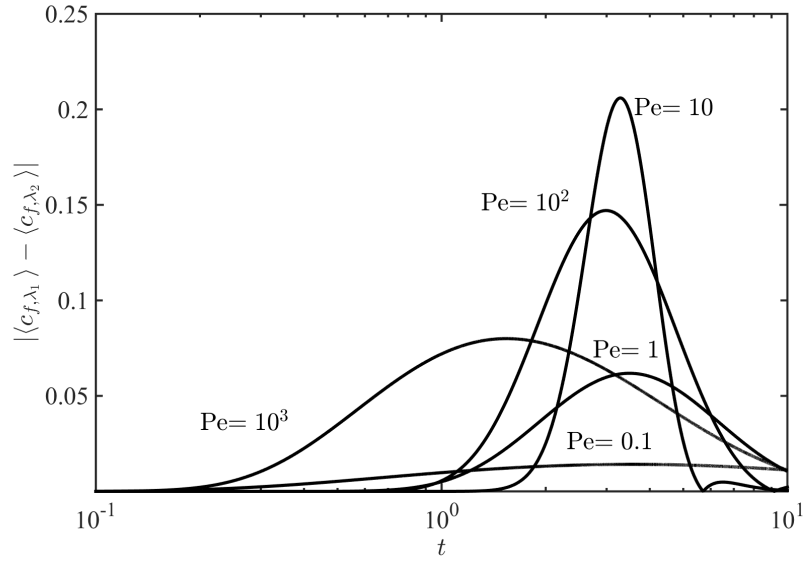


Figure 2.9: Difference between the average concentration in the channel  $\langle c_f \rangle$  for two values of dimensionless permeability  $\lambda = \sqrt{10^2}$  and  $\lambda = \sqrt{10^3}$  and different Péclet numbers, obtained from (3.6). A set of parameters used in the simulations is:  $\phi = 0.5$ ,  $\Psi = -0.78$ ,  $\epsilon = 0.02$ ,  $D_f = 1$ ,  $D_{mx} = 0.1$ ,  $D_{my} = 0.1$ ,  $h = 10$ . Concentration  $\langle c_f \rangle$  is measured at  $x = 1$ .

approximation error, which decreases in time as the solution approaches the steady state and the transient terms become increasingly small, i.e.  $\partial_t c_f^{(0)} \rightarrow 0$  and  $\partial_t c_m^{(0)} \rightarrow 0$  as  $t \rightarrow \infty$ .

### 2.5.3 Upscaled model results

Figure 2.9 shows the difference between the average concentrations in the channel calculated from (3.6) for two values of  $\lambda$ ,  $\lambda = \sqrt{10^2}$  and  $\lambda = \sqrt{10^3}$  at a given location along the channel, and for different Péclet numbers. Figure 2.9 shows how

differences in matrix permeability become more relevant for intermediate Péclet numbers, i.e.,  $Pe \in (1, Pe^*)$ , when the interplay between advective and diffusive mass transfer is strongly controlled by matrix properties. For  $Pe < 1$ , diffusive transport is dominant. In this scenario, the geometrical characteristics of the matrix have a small impact on transport. Similarly, for  $Pe > Pe^*$ , the impact of matrix permeability decreases. In advection-dominated regimes, concentration reaches saturation ( $c_f = 1$ ) in a short period of time: this leads to a weak dependence of the macroscale concentration on the matrix topological features.

Figure 2.10 shows the temporal evolution of the macroscopic concentration in the channel and the matrix at a given location along the flow direction. In diffusion-dominated regimes, i.e. when  $Pe < 1$ , Figure 2.10 (top), the concentration difference in the matrix and the channel is very small. Fast diffusive mass transport enhances transversal mixing at the interface between the matrix and the channel, and leads to decreased differences in concentration between the former and the latter. For high Péclet numbers, Figure 2.10 (bottom), the difference in the average concentration in the matrix and the channel increases due to the delay in advective mass transfer in the matrix. As a result, the concentration gradient, and therefore the mass flux, across the matrix-channel interface increases with  $Pe$  for a given permeability value.

#### 2.5.4 Comparison with existing models

In this section, we compare the proposed model with that introduced by Dejam *et al.*, who assume that mass transport in the porous matrix is purely diffusive and

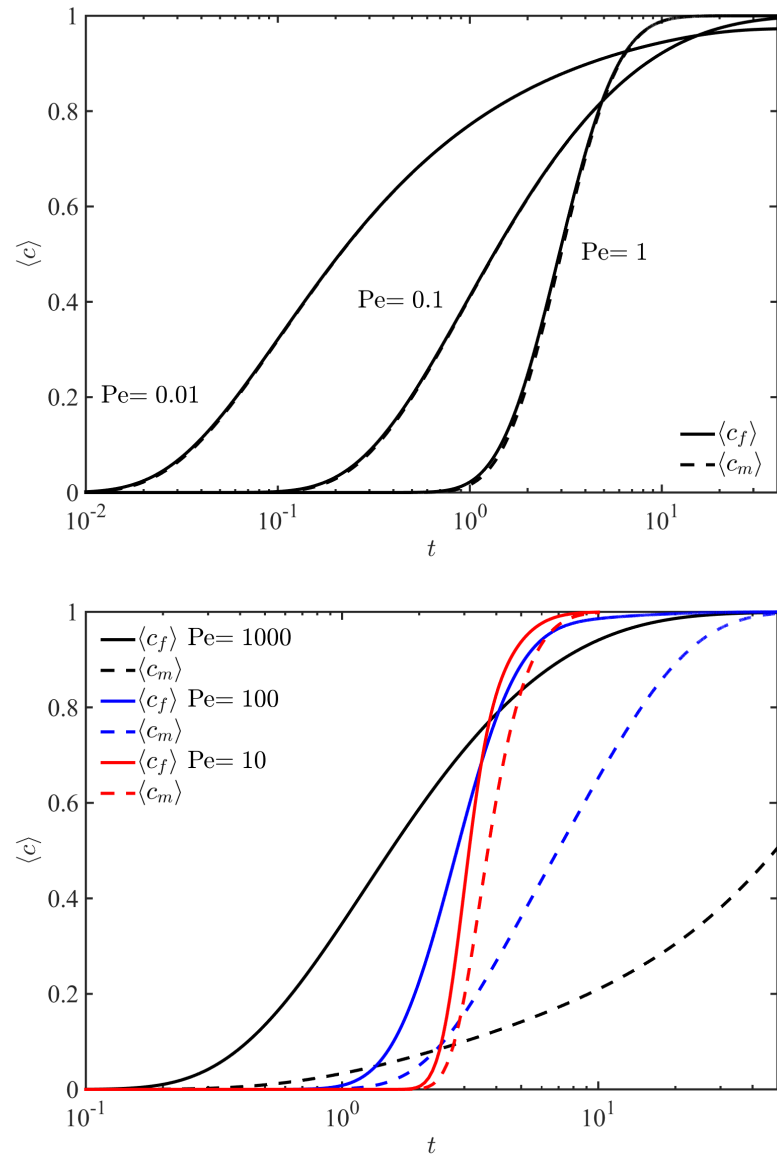


Figure 2.10: Comparison between  $\langle c_f \rangle$  (solid lines) and  $\langle c_m \rangle$  (dashed lines) for low (top) and (high) Péclet numbers. The simulation parameters are  $\phi = 0.5$ ,  $\Psi = -0.78$ ,  $\epsilon = 0.02$ ,  $D_f = 1$ ,  $D_{mx} = 0.1$ ,  $D_{my} = 0.1$ ,  $h = 10$ . Concentration  $\langle c_f \rangle$  and  $\langle c_m \rangle$  are measured at  $x = 1$ .

transverse to flow (i.e.  $y$ -direction). This corresponds to the  $k = 0$  (or  $\lambda \rightarrow \infty$ ) limit in the present model. To analyze differences and/or similarities in performance between the two models, we consider two configurations: a highly permeable ( $\lambda = 0.3$ ) and a nearly impermeable ( $\lambda = 100$ ) matrix. Dejam *et al.*'s solution for the average concentration in the fracture  $\langle c \rangle_{f,\text{DHC}}$  is [79]

$$\langle c \rangle_{f,\text{DHC}}(x, t_D) = \frac{e^{\alpha t_D}}{t_D} \left\{ \frac{1}{2} \hat{C}_{f,\text{DHC}}(x, \alpha) + \Re \left[ \sum_{l=1}^n (-1)^l \hat{C}_{f,\text{DHC}} \left( x, \alpha + \frac{l\pi}{t_D} \sqrt{-1} \right) \right] \right\} \quad (2.57)$$

where  $\Re[\cdot]$  represents the real part of a complex function,  $\alpha$  controls the accuracy of the numerical Laplace transform and  $t_D = \tilde{t}/(b^2/D_{my})$ . In the following comparative study, we use the dimensionless time defined in (2.24), instead. Also, we set  $\alpha t_D = 4$  and use  $n = 1e5$  terms in the summation.

In Figure 2.11 we compare the models (3.6a) and (2.57) (by Dejam *et al.*) with the macroscopic concentration obtained from averaging the pore-scale solution. For low Péclet numbers, both models perform well independently of matrix permeability. For high Péclet number ( $Pe = 100$ ) and low permeability (or high  $\lambda$ ), Dejam *et al.*'s solution shows a better accuracy than the upscaled model proposed here. This is apparent from the error  $E_f$  plotted in Figure 2.11 as a function of time: while model (3.6a) can be still considered predictive since  $E_f$  is bounded by  $\sqrt{\epsilon}$ , Dejam *et al.*'s solution has a lower maximum error. Instead, for  $Pe = 100$  and high permeability values (or low  $\lambda$ ), our upscaled equation (3.6a) is more accurate than (2.57). Importantly, in this scenario, the error in Dejam *et al.*'s solution is not bounded by  $\sqrt{\epsilon}$ , i.e. the error is larger than that prescribed by the upscaling procedure. Finally, for very

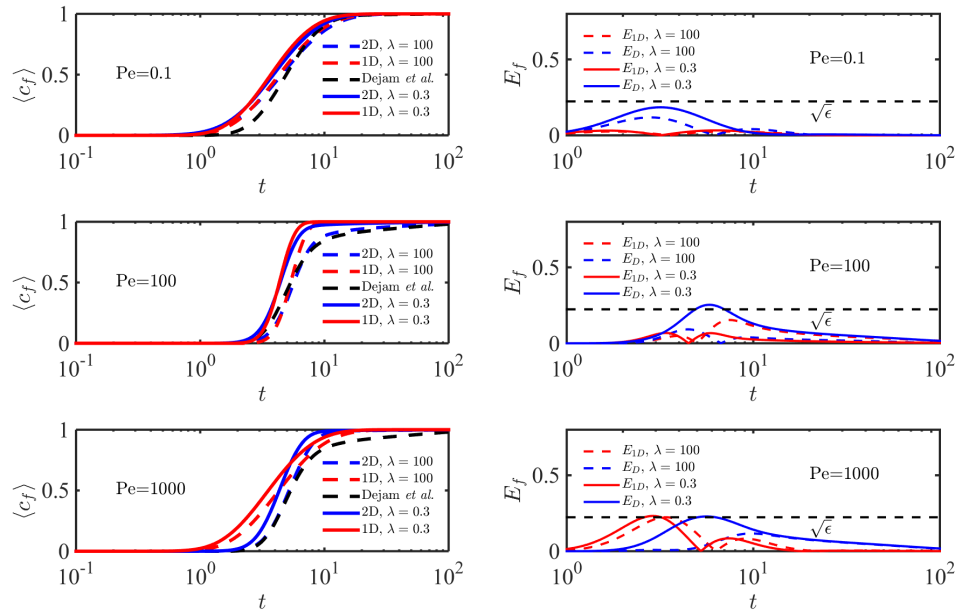


Figure 2.11: (Left) Comparison between the breakthrough curves obtained from (3.6a) and (2.57) (by Dejam *et al.*) with the averaged pore-scale solution for two permeability values,  $\lambda = 0.3$  and  $\lambda = 100$ . (Right) Absolute errors between up-scaled solutions (3.6a) and (2.57) and the averaged pore-scale solution  $E_{1D}(x, t; \lambda) := |\langle c_f \rangle_{2D} - \langle c \rangle_{f,1D}|$  and  $E_D(x, t; \lambda) := |\langle c_f \rangle_{2D} - \langle c \rangle_{f,Dejam \text{ et al.}}|$ , respectively. The simulation parameters are:  $\epsilon = 0.02$ ,  $\phi = 0.1$ ,  $\Psi = -1$ ,  $D_f = 1$ ,  $D_{mx} = 0.1$ ,  $D_{my} = 0.01$ ,  $h = 10$ .

large  $Pe$  ( $Pe = 1000$ ), both models give higher errors at early times, regardless of the permeability value. This analysis demonstrates that the model described by (3.6a) and Dejam *et al.*'s solution are complementary to each other since the former can accurately describe macroscopic mass transport in advection-dominated regimes in coupled systems with highly permeable matrices, while the latter captures transverse diffusion into the matrix only in the low permeability case.

## 2.6 Conclusions

Flow and transport above micro-patterned and porous surfaces occur in a variety of systems, ranging from engineered surfaces to bioreactor devices. The achievement of optimal macroscopic properties, e.g. improved mixing, in a number of such applications is hampered by the lack of understanding of how surface/matrix properties (e.g. porosity, permeability and thickness) relates to the system- or macro-scale.

In this work, we use perturbation methods to study passive scalar transport in a coupled channel-matrix system and obtain an analytical relationship between matrix properties and solute transverse dispersion. To the best of our knowledge, this is the first analytical relationship that establishes a connection between macroscopic transport features, matrix properties and transport regimes (i.e. Péclet number). We accomplish this by deriving upscaled equations for mass transport in a channel-matrix coupled system, while accounting for two-dimensional diffusion and non-uniform velocity field both in the channel and the matrix. The average velocity profile

in the coupled system, as well as the slip velocity at the channel-matrix interface, is determined by a two-domain approach where the Stokes' and Darcy-Brinkman equations are coupled to describe flow in the channel and the permeable matrix, respectively.

Our results show that the impact of matrix properties on solute transversal mixing and, more specifically, on the macroscopic dispersion coefficient is controlled by the magnitude of Péclet number. In particular, for  $Pe < 1$ , transport in the channel-matrix system is dominated by diffusion, and matrix properties have little to no impact on macroscopic transport. In this regime, mixing is controlled by diffusion in the direction transverse to the mean flow and the dimensionless dispersion coefficient is independent of both  $Pe$  number and matrix permeability. When  $1 < Pe < Pe^*$ , solute transport is controlled by both diffusion and advection. The interplay between these mass transport mechanisms is strongly dependent on both matrix permeability and Péclet number. In this regime, macroscale dispersion can be controlled both by active and passive mechanisms: the former consist in modifying the operating flow conditions of the device (i.e. Péclet number), while the latter are based on modifying the surface coating properties (i.e. permeability). For  $Pe > Pe^*$ , mass transport is dominated by advection and the dispersion coefficient reaches a constant value independent of Péclet number and function of matrix permeability only. By means of asymptotic analysis, we demonstrate that different scaling regimes of the normalized dispersion coefficient  $\Pi$  exist for thin ( $\Lambda \lesssim 1$ ) and thick porous layers ( $\Lambda \gg 1$ ). In particular,  $\Pi$  is controlled by the dimensionless width  $h$  of the porous matrix, when

$\Lambda \lesssim 1$ , and scales linearly or quadratically with  $h$ , when  $h < 1$  or  $h > 1$ , respectively. In the thick porous medium regime,  $\Pi$  is controlled by matrix permeability  $\lambda$ . This provides specific design guidelines to optimize mixing in channel-porous systems.

The upscaled model was validated against numerical simulations of the fully resolved two-dimensional channel-matrix coupled system. The upscaled solution agrees with the average concentration obtained from the exact two-dimensional ADEs within the error bound prescribed by the homogenization approach and performs well for large  $Pe$ , despite condition (2) is violated. This is to be expected since the latter is a sufficient (and not necessary) condition to guarantee that the upscaled equation (3.6) describe spatially averaged pore-scale processes within errors of order  $\sqrt{\epsilon}$ .

Finally, a detailed comparison between our model and that of Dejam *et al.* [79], which only considers one-dimensional transverse diffusion in the matrix, shows that the two models are complementary to each other. For systems with permeable matrices, we found our model to be superior to Dejam *et al.*'s for all considered Péclet numbers. Instead, unlike Dejam *et al.*'s, our model cannot accurately capture the tailing effect introduced by the purely diffuse interfacial mass flux in impermeable matrices.

To the best of our knowledge, this is the first study, which provides (i) a rigorous basis to relate matrix permeability to dispersion coefficient in coupled channel-matrix systems and (ii) quantitative guidelines for the design of porous/micro-patterned surfaces. The analysis also shows the possibility of controlling dispersion by either active (i.e. changing the operating conditions) or passive mechanisms (i.e. controlling



matrix properties) in the appropriate range of Péclet numbers.

Ling, B., Tartakovsky, A., Battiato, I., (2016), 'Dispersion controlled by permeable surfaces: surface properties and scaling'. *Journal of Fluid Mechanics*, 801, 13-42.

## **Chapter 3**

# **Patterned microchannels as benchmark experiments for transport in fracture-matrix systems**

### **3.1 Introduction**

Microfluidic devices are widely used to study transport in porous media. Pore-scale experiments on microchips are in fact routinely employed to test and validate macroscopic approximations and models. One of the many advantages of using micromodels is the possibility of controlling the micro-scale topology of the medium and, consequently, studying the impact of pore-scale topological features on system-scale (macroscale) phenomena, e.g. flow and transport as well as solute mixing and reactions[351, 368]. Combined with advanced imaging methods[343], solute concen-

tration field can be measured at a fine temporal resolution (10 ~ 100 ms per frame). The underlying assumption to relate flow and (reactive) transport processes at the pore-scale with their macroscale counterpart (i.e. system-scale response) is the (minimum) requirement that separation of geometrical length-scales between the micro and the macro-scale must exist, i.e. the typical length scale associated with the obstacles, e.g. their mean diameter  $d$ , should be much smaller than a characteristic length at the macroscale, e.g. the length of the microfluidic chip  $L$ . This effectively translates in the possibility of defining a Representative Elementary Volume (or REV), i.e. an averaging volume whose characteristic scale  $W$  is associated with the width of the microfluidic chip (or the porous layer) such that  $d \ll W < L$ . This condition can be easily enforced by design when the microchip is occupied by solid obstacles throughout its width. For example Willingham *et al.*'s and Zhang *et al.*'s microchips [351, 368] have  $d \approx 200 - 300 \mu\text{m}$ ,  $W = 1 \text{ cm}$  and  $L = 2 \text{ cm}$ . Numerous other studies have used similar configurations to investigate, e.g., the impact of pore-scale geometry on macroscopic reaction rates, mixing dynamics, multiphase flow displacement etc.

Systems with a fracture embedded in a matrix with interfaces allowing exchange of mass/momentum between the two regions exist in a variety of natural and industrial processes. Some examples include nutrient uptake from roots [197, 110], contaminant transport in fractured rocks, flows over sediments beds [112, 229, 32, 188], slippery liquid-infused porous surfaces [71, 137], flows above carbon nanotube forests [78, 26, 28], ultrafiltration of colloids [200], nutrient delivery in micro-fluidic bioreactor devices [121, 118] and chaotic mixing in microchannels [298, 297]. Coupled

fracture-matrix systems present unexpected experimental and theoretical challenges both in terms of controlled pore-scale experiments and macroscale models validation and verification, compared to the study of more classical Darcy-type experiments on microchips. Theoretically, the difficulty of studying solute transport in such systems lies in the dynamic coupling between the two regions (fracture of aperture  $2b$  and matrix of width  $W$ ) and in the need to incorporate different geometrical properties of the matrix into solute transport models at the macroscale. Both objectives are addressed, though partially, by employing upscaling methods (e.g. homogenization method, stochastic homogenization, volume averaging) to derive 1D macroscopic models for the average concentration in the fracture  $\langle c_f \rangle$  (and the matrix  $\langle c_m \rangle$ ) under the assumption of a thin fracture (i.e.  $b \ll L$ ), and to determine the effective dispersion coefficient in the fracture in terms of the effective matrix properties (generally porosity only). Yet, most one-dimensional thin fracture models [303, 79], as well as two-dimensional dispersion models [269], assume purely diffusive transport in the matrix, and routinely neglect permeability of and dispersive transport in the matrix. Only recently, attempts to account for matrix permeability have been undertaken [118, 187]. Ling and *et al.*[187] utilize perturbation theory and upscaling techniques to obtain the fracture dispersion coefficient in terms of matrix porosity and permeability. Notwithstanding the variety of proposed models, there is no experimental evidence of their validity, or regimes of applicability. While experiments on real fractured porous media can be conducted, there is little control on porous matrix topology. As a result, identification of a relationship between pore-scale matrix structure and fracture dis-

persion becomes challenging. Experiments on microfluidic devices would overcome such a difficulty. Yet, the challenge of employing microchips to study fracture-matrix systems and validate corresponding theoretical models lies in (i) the presence of a ‘virtual’ interface between the fracture and the patterns, (ii) the open question of whether or not few layers of discrete obstacles can be modelled as an effective medium and (iii) how to properly define a REV across interfaces with discontinuous properties.

In this work, we compare experimental data from microfluidic cells patterned with different topologies (transverse riblets and arrays of cylinders) with the macroscopic models by Dejam *et al.*[79] and Ling *et al.*[187], that account for purely diffusive and dispersive transport in the matrix, respectively. The scope of the study is twofold. On the one hand, we demonstrate that patterned microfluidic chips can be used as experimental surrogates of fracture-matrix systems, and on the other, we examine the influence of pore-scale matrix topology on macro-scale (continuum-scale) solute dispersion. The experiments are designed to highlight the significance and influence of matrix geometry on the accuracy of the theoretical solutions in different Péclet number regimes, and to develop a phase diagram to identify the applicability conditions of each macroscopic solution.

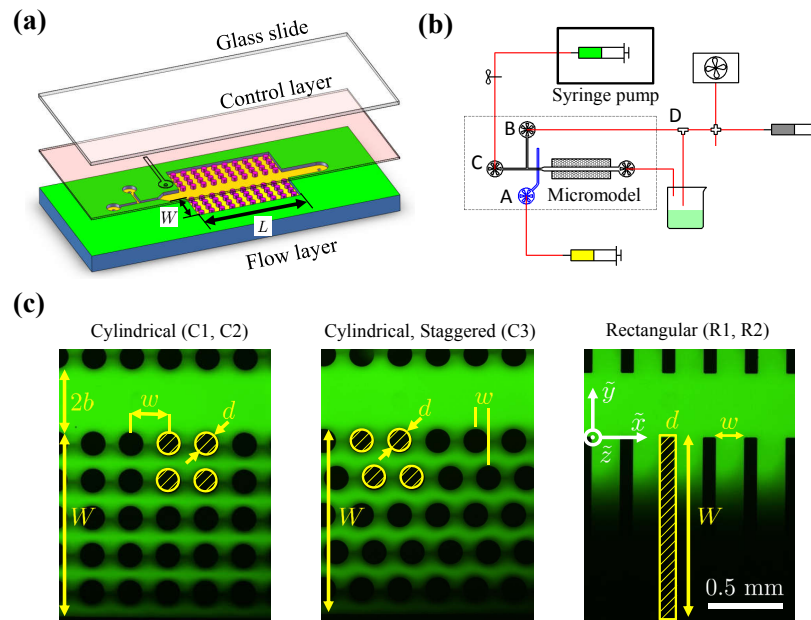


Figure 3.1: Schematics of the experimental setup: (a) micromodel design with valve system, (b) exterior flow system, and (c) an example of measured concentration distribution, where the dye concentration increases with the intensity of the green colour.

## 3.2 Material and Methods

### 3.2.1 Micromodels

The micromodels used in this study have been fabricated at the Pacific Northwest National Laboratory, applying standard microphotolithography techniques. First, the flow layer features, including the fracture and the porous matrix are printed on a mask, Figure 3.1(a). A separate silicon wafer is then spin-coated with SU-8 photoresist

before the wafer is exposed to UV light with the printed mask placed on top of it. The exact same pattern is created on the silicon wafer during the developing process. The silicon wafer is subsequently placed on a hot plate for heat treatment at a temperature of  $180^{\circ}\text{C}$  and kept for 30mins. After this treatment, the developed features have a depth  $H_z = 28.0\mu\text{m}$ . A mixture of polydimethylsiloxane (PDMS) base and PDMS curing agent is employed to produce replicas of the silicon micromodels using the wafer as the mold. PDMS is poured onto the wafer and, after the curing process, the flow layer of the micromodel is obtained, Figure 3.1(a). A control layer is bound to the flow layer to keep the interior surfaces uniform and to control the inlet flow. The control layer is patterned with an air valve, a thin elastomeric membrane which deforms when air pressure ( $\sim 10$  psi) is applied. The deformed membrane seals the flow channel to prevent flow coming from the inlet. In the final step, the micromodel is bounded to a glass slide using plasma and cured for 12 hours at  $75^{\circ}\text{C}$ .

### 3.2.2 Visualization and Measurement

Alexa Flour 488 (ThermoFisher Scientific Inc., San Diego, CA), a green fluorescent dye, is used for visualization and measurement of the concentration in the micromodels. The initial concentration ( $c_0$ ) of the dye solution is  $34.40\ \mu\text{mol}\cdot\text{L}^{-1}$ . The molecular diffusion coefficient of Alexa 488 in water is  $D_0 = 4.35 \times 10^{-10}\ \text{m}^2\text{s}^{-1}$  at  $20^{\circ}\text{C}$  [245]. Other properties (e.g. viscosity and density) of the dilute dye solution are considered the same as those of DI-water. In all experiments, the laboratory temperature is set to  $21 \pm 0.5^{\circ}\text{C}$ . Thus, all fluid and transport properties are assumed to

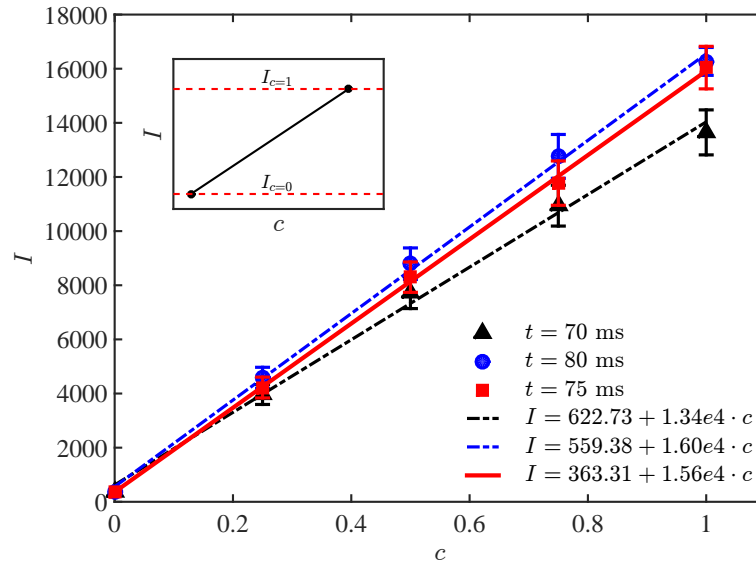


Figure 3.2: Intensity-concentration relations for three exposure times. The error bar represents three standard deviations.

be the same for all experiments. The micromodels are placed on a motorized stage (Prior Scientific Instrument Inc., Rockland, MA), controlled by NIS-Element (Nikon, Melville, NY) software, and Images of fluorescent intensity fields are recorded by a CCD camera attached to a Nikon Ti Epi-fluorescence microscope (Nikon, Melville, NY) with a 4X objective. During each experiment, typically lasting approximately 30 minutes, 500-1500 pictures are taken. In every experiment, the micromodel is first saturated with DI-water, using inlet B before injection of the dye solution, see Figure 3.1(b). After visual inspection of the saturation, water injection is interrupted. To prevent pre-mixing during this phase in the exterior tubing system, the air valve (A in Figure 3.1(b)) is kept closed. Dye solution is then injected from inlet C (Figure 3.1-b)



by a syringe pump (New Era, Farmingdale, NY) at a constant volumetric flow rate ( $Q$ ). Since the dye solution would occupy the tubing components between valves A, B, and C, at the beginning of the dye injection experiment, valve A is opened while B is closed. After each experiment, the tubing system and the micromodel are thoroughly cleaned.

### 3.2.3 Data Analysis

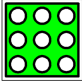
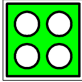
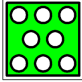
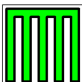
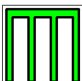
In this study, fluorescence concentration is computed using intensity concentration calibration curves,  $c(I)$ , where  $c$  [-] is the concentration normalized by the inlet concentration  $c_0$ , and  $I$  [-] is the light intensity. To prevent ambient light pollution during the measurement, the micromodel is covered by black foil. First, we test several exposure times to determine those that lead to the best linear relationship between light intensity,  $I$ , and concentration,  $c$ , as shown in Figure 3.2. The calibration is performed using the linear relationship

$$I_1 = I_0 + \alpha c, \quad (3.1)$$

where  $\alpha$  is the calibration constant, and  $I_0$  and  $I_1$  are the light intensities measured in zero-concentration and fully fluorescence saturated domains (inset of Figure 3.2). The results show that an exposure time of 75ms yields the best linearity (with  $\alpha=1.56e4$  [-]). As a result, the exposure time was set to 75ms in all experiments.

### 3.2.4 Porous Structure and Experiment Matrix

Table 3.1: Overview of experimental conditions: volumetric flow rate  $Q$ , Péclet number  $Pe$ , structure porosity  $\phi$ , and obstacles dimensions  $d$  and  $w$ , as defined in Figure 3.1. For all micromodels, the chip's length and depth are  $L = 15$  mm and  $H_z = 28.0 \mu\text{m}$ , respectively, the porous matrix width is  $W = 1.5$  mm, and the fracture aperture is  $b = 0.25$  mm.

		$Q$ ( $\mu\text{L hr}^{-1}$ )	$Pe$ (-)	$\phi$ (-)	$d$ (mm)	$w$ (mm)
	<b>C1-10</b>	10	40.3			
	<b>C1-50</b>	50	201.9	0.65	0.08	0.12
	<b>C1-100</b>	100	403.7			
	<b>C2-10</b>	10	40.3			
	<b>C2-50</b>	50	201.9	0.48	0.24	0.3
	<b>C2-100</b>	100	403.7			
	<b>C3-10</b>	10	40.3			
	<b>C3-50</b>	50	201.9	0.65	0.08	0.04
	<b>C3-100</b>	100	403.7			
	<b>R1-10</b>	10	40.3			
	<b>R1-50</b>	50	201.9	0.65	0.11	0.2
	<b>R1-100</b>	100	403.7			
	<b>R2-10</b>	10	40.3			
	<b>R2-50</b>	50	201.9	0.48	0.11	0.1
	<b>R2-100</b>	100	403.7			

To test the ability of patterned microchannels to act as surrogates of coupled channels/porous media flow systems, we design different pattern geometries to represent both highly permeable and nearly impermeable matrices (Table 3.1): (i) aligned and staggered cylindrical posts (referred to as C structures), and (ii) rectangular riblets perpendicular to the main flow direction (referred to as R structures), respectively. The different matrix structures and obstacles' dimensions are illustrated in Table 3.1. The transverse riblets can model matrices with zero longitudinal permeability since the net flux through the pattern is zero in the flow direction. Experiments are performed at three different Péclet numbers,  $Pe$ , for each configuration with

$$Pe := \frac{Ub}{D_0} \quad (3.2)$$

where  $U = Q/(2bH_z)$  is the inlet mean velocity,  $b$  and  $H_z$  the channel half-width and depth, respectively, and  $D_0$  the molecular diffusion coefficient. Concentration transect data at two different locations along the flow direction (near the inlet, at  $\tilde{x} = 2$  mm, and near the center of the channel, at  $\tilde{x} = 8$  mm) are collected.

### 3.2.5 Analytical Models

We investigate and quantify how representative the micropatterns are of porous matrices with different permeabilities by comparing the collected transport data with two analytical solutions for transport and dispersion in channels/fractures embedded in non-permeable [79] and permeable [187] matrices. Both solutions describe the spatio-temporal evolution of the dimensionless concentration in the channel and the

matrix averaged over the channel and matrix width,  $\langle c_f \rangle$  and  $\langle c_m \rangle$ , where  $\langle \cdot \rangle$  defines an averaging operator

$$\langle \cdot \rangle = \frac{1}{L^*} \int_0^{L^*} \cdot dy \quad (3.3)$$

with  $L^* = 1$  for the fracture and  $L^* = -h$  for the matrix, and  $h = W/b$  the dimensionless matrix width. The model proposed by Dejam and *et al.*[79] under the assumption of only diffusive transport in an otherwise impermeable matrix is here referred to as ‘diffusive matrix model’ for simplicity. It is described by

$$\epsilon \text{Pe} \frac{\partial \langle c_f \rangle}{\partial t} + \epsilon \text{Pe} \frac{7}{5} V_m \frac{\partial \langle c_f \rangle}{\partial x} = \epsilon^2 D_d \frac{\partial^2 \langle c_f \rangle}{\partial x^2} - 3(\langle c_f \rangle - \langle c_m \rangle), \quad (3.4a)$$

$$\epsilon \text{Pe} \frac{\partial \langle c_m \rangle}{\partial t} = D_m \frac{\partial^2 \langle c_m \rangle}{\partial y^2}, \quad (3.4b)$$

where  $\epsilon = b/L$ ,  $V_m$  is the dimensionless average velocity,  $D_m$  is the effective molecular diffusion coefficient in the matrix normalized by  $D_0$ ,  $t = \tilde{t}U/L$ ,  $x = \tilde{x}/L$  and  $y = \tilde{y}/b$ .

The dispersion coefficient in the fracture is given by

$$D_d = 1 + \frac{1}{175} \text{Pe}^2. \quad (3.5)$$

The model proposed by Ling *et al.*[187] explicitly accounts for a permeable matrix with porosity  $\phi$  [-] and permeability  $k$  [ $L^2$ ], and is referred to as ‘dispersive matrix model’. It is governed by the dimensionless system of equations

$$\text{Pe} \left( \frac{\partial \langle c_f \rangle}{\partial t} + \langle u_f \rangle \frac{\partial \langle c_f \rangle}{\partial x} \right) = \epsilon D_f^* \frac{\partial^2 \langle c_f \rangle}{\partial x^2} + \phi \text{Pe} \langle u_m \rangle \frac{\partial \langle c_m \rangle}{\partial x} - \frac{3\phi D_{my}}{\epsilon^2 h} (\langle c_f \rangle - \langle c_m \rangle), \quad (3.6a)$$

$$\text{Pe} \left( \frac{\partial \langle c_m \rangle}{\partial t} + \langle u_m \rangle \frac{\partial \langle c_m \rangle}{\partial x} \right) = \epsilon D_m^* \frac{\partial^2 \langle c_m \rangle}{\partial x^2} - \frac{\text{Pe} \langle u_f \rangle}{\phi h} \frac{\partial \langle c_f \rangle}{\partial x} + \frac{3D_f}{\epsilon^2 \phi h} (\langle c_f \rangle - \langle c_m \rangle), \quad (3.6b)$$

where  $D_f$  is the dimensionless effective molecular diffusion coefficient in the fracture and  $D_{my}$  is the dimensionless effective molecular diffusion coefficient in the matrix in the  $y$ -direction [187]. In this study, we let  $D_f = D_{my} = 1$ . The velocities  $u_f$  and  $u_m$  in the fracture and matrix are obtained by solving the coupled Stokes' equation in the fracture and Darcy-Brinkman equation in the matrix[187]

$$u_f(y) = -\frac{\Psi}{2}(y^2 + Ay + B), \quad y \in [0, 1], \quad (3.7a)$$

$$u_m(y) = -\frac{\Psi}{\lambda^2}(1 + Ee^{\lambda y} + Fe^{-\lambda y}), \quad y \in [-h, 0], \quad (3.7b)$$

where  $\Psi = b^2 \nabla P / \mu U$  is the dimensionless pressure gradient (with  $\mu$  the dynamic viscosity and  $\nabla P$  the dimensional pressure drop),  $A = 2$ ,  $B = 2\lambda^{-2}(-1 + e^{\lambda h})(-1 + e^{\lambda h} + \lambda + \lambda e^{\lambda h})(1 + e^{2\lambda h})^{-1}$ ,  $E = e^{\lambda h}(-1 + \lambda e^{\lambda h})(1 + e^{2\lambda h})^{-1}$ ,  $F = (\lambda + e^{\lambda h})(1 + e^{2\lambda h})^{-1}$ , and

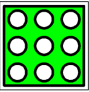
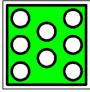
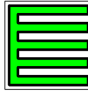
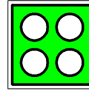
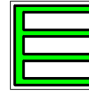
$$\lambda = \frac{b}{k} \quad (3.8)$$

is the inverse of the dimensionless permeability. The dispersion coefficients  $D_f^*$  and  $D_m^*$ , that explicitly depend on  $\lambda$ , are given by

$$D_i^* = 1 + \text{Pe}^2 I_i(\lambda, h, \Psi) \quad (3.9)$$

where  $I_i(\lambda, h, \Psi) = \langle u_i \int_0^y \int_0^y u'_i(y) dy dy \rangle$ ,  $u'_i = u_i - \langle u_i \rangle$ , is the velocity fluctuation and  $i = \{f, m\}$ . Each model has two fitting parameters. Due to the difficulty of precisely measuring small pressure gradients in microfluidic devices, and the lack of information about the relationship between topology and effective properties of the matrix, we treat  $V_m$  and  $\Psi$ , and  $D_m$  and  $\lambda$  as a fitting parameters in (3.4) and (3.6), respectively. The fitting parameters are determined by a least-square algorithm.

Table 3.2: Fitting parameters and modeling error for  $\tilde{x}_1 = 2$  mm and  $\tilde{x}_2 = 8$  mm.

Runs	Dispersive matrix model, Eq. (6)						Diffusive matrix model, Eq. (4)						
	$\lambda$	$\Psi$	$E(\times 10^{-2})$		$V_m$		$D_m$		$E(\times 10^{-2})$				
	$\tilde{x}_1$	$\tilde{x}_2$	$\tilde{x}_1$	$\tilde{x}_2$	$\tilde{x}_1$	$\tilde{x}_2$	$\tilde{x}_1$	$\tilde{x}_2$	$\tilde{x}_1$	$\tilde{x}_2$	$\tilde{x}_1$	$\tilde{x}_2$	
	<b>C1-10</b>	1.05	1.08	-26.5	-14	1.43	2.78	0.07	0.1	0.41	0.5	18.9	19.3
	<b>C1-50</b>	1.06	1.08	-45.5	-17	1.46	2.48	0.11	0.2	0.19	0.1	8.7	11.7
	<b>C1-100</b>	1.1	1.1	-85	-24.5	1.83	1.97	0.41	0.7	0.41	0.5	4.9	8.8
	<b>C3-10</b>	0.89	0.9	-26.5	-14	2.78	2.11	0.1	0.5	0.40	0.8	17.0	12.8
	<b>C3-50</b>	0.92	0.85	-31	-18	1.98	2.16	0.1	1.0	0.21	0.07	9.83	12.8
	<b>C1-100</b>	0.84	0.9	-65	-20.5	1.97	3.41	0.31	0.5	0.21	0.21	8.45	8.81
	<b>R1-10</b>	2.5	2.2	-45.5	-19	4.75	3.38	25	10	27	0.5	2.98	1.88
	<b>R1-50</b>	2.0	2.2	-45	-40	5.24	4.13	8	10	10	1	2.49	2.03
	<b>R1-100</b>	3.0	3.0	-55	-27	6.57	5.78	2	10	5	1	1.09	3.26
	<b>C2-10</b>	1.75	1.75	-30	-16.5	2.67	3.61	0.1	0.8	0.25	0.1	17.4	16.6
	<b>C2-50</b>	1.75	1.70	-25.5	-16	0.97	2.39	0.07	1	0.19	0.1	10.3	9.22
	<b>C2-100</b>	1.65	1.55	-76	-21.5	6.57	3.95	0.17	0.25	0.31	1.6	2.52	5.99
	<b>R2-10</b>	4	4.7	-38	-31	2.12	6.65	29	10	50	1.3	2.09	5.04
	<b>R2-50</b>	4	4.8	-40	-40	2.57	4.51	3	1	10	2.8	0.90	1.30
	<b>R2-100</b>	4	3.5	-40	-30	2.33	5.30	2	1.6	7	3.0	2.50	2.88

### 3.3 Results: comparison with experimental data

To evaluate the error between the analytical solutions and the experimental results, we first fit both analytical solutions with each available data set, and then calculate the mean absolute error,

$$E_j = \frac{\sum_{i=1}^N |\langle c_f \rangle_{i,j} - \langle c_f \rangle_{i,\text{Data}}|}{N}, \quad j = \{\text{Diff, Disp}\} \quad (3.10a)$$

where  $\langle c_f \rangle_{i,j}$  is the  $j$ -model fitted concentration at time  $t_i$ ,  $i = \{1, \dots, N\}$ , and the subscripts ‘Diff’ and ‘Disp’ refer to the model that accounts for a purely diffusive and dispersive matrix, described by Equations (3.4) and Equations (3.6), respectively. Figure 3.3 shows the ratio  $E_{\text{Disp}}/E_{\text{Diff}}$  for all considered geometries as a function of Péclet number. We find that the dispersive-matrix model (3.6) is more accurate than its diffusive counterpart for those structures with significant advective transport between obstacles (i.e. C1, C2 and C3). Instead, the diffusive-matrix model better performs on R1 and R2 structures, where the transverse riblets block any longitudinal advective flux through the pattern and the transport inside the microstructure is mostly diffusive. These results support the hypothesis that properly designed micropatterns can represent continuum-scale porous media in coupled fracture/matrix systems. Figure 3.3 shows that structures with smaller porosity exhibit smaller permeability (e.g. C1 and C2), and permeability decreases with increasing tortuosity, for a given porosity (e.g. C1 and C3).

Furthermore, when  $\lambda \lesssim 1$ , the fitted  $\lambda$  value has small variations for the same

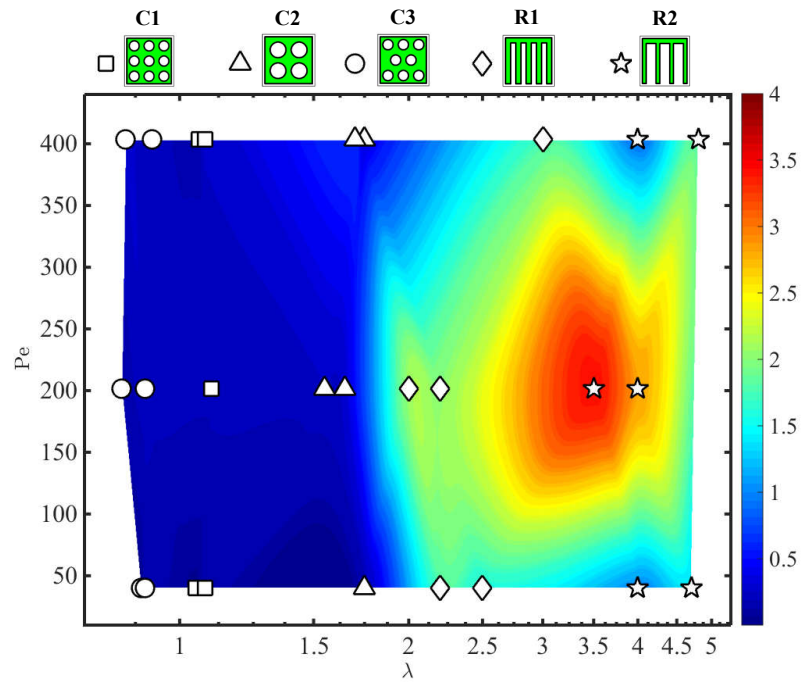


Figure 3.3: Error ratio  $E_{\text{Disp}}/E_{\text{Diff}}$  plotted in Péclet number (Pe) and dimensionless permeability ( $\lambda$ ) space. Dots are representing exact value of the ratio, colored space filled is cubic fitting based on the exact value points. Warm color corresponds to values that are larger than 1.

microstructure (C1, C2 and C3) at different Péclet. This suggests that a unique permeability value  $k$  (or its dimensionless counterpart  $\lambda$ ) can be experimentally determined for each microstructure. The scatter in fitted  $\lambda$  increases for R1 and R2 structure, where the effective property is ill-defined (i.e. the patterns are impermeable). In Figure 3.4 and 3.5, we plot the fitted analytical solutions for the riblet- and the cylinder-like patterns for different Péclet numbers. Importantly, Figure 3.5 shows an excellent



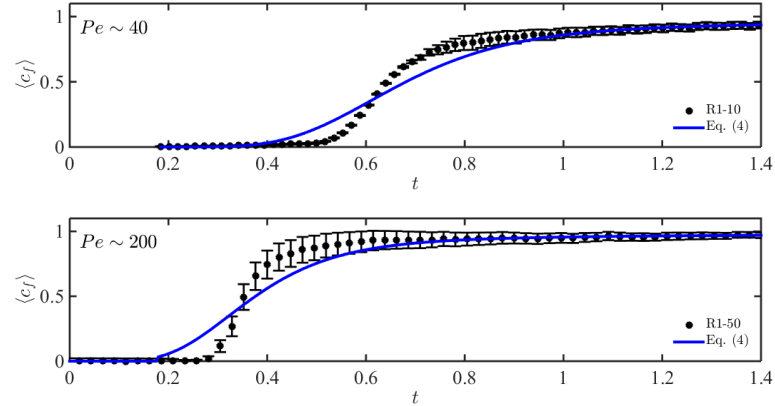


Figure 3.4: Comparison between experimental data collected at  $\tilde{x} = 2$  mm along the channel patterned by transverse R1 riblets (symbols) and the fitted analytical solution (3.4) (line) for different values of the Péclet number. The error bars represent one standard deviation of the average concentration from its mean value.

agreement between the experimental data and  $\langle c_f \rangle$  predicted by using the permeability (or  $\lambda$ ) value obtained as an arithmetic average of the fitted values at different Péclet numbers in any given geometry (e.g. C1 and C3). Such experiments (i) support the hypothesis that a relatively thin layer of obstacles (i.e. with a characteristic width smaller than a typical REV) can be modelled as a porous matrix, (ii) provide a methodology to measure of the effective properties of the micropattern and (iii). is a novel approach to determine permeability of a matrix in coupled fracture-matrix systems, different from traditional measurements where one needs to drill a core or take samples of the matrix and measure the permeability using Darcy experiment.

We can conclude that (i) patterned microfluidic channels can be used as bench-

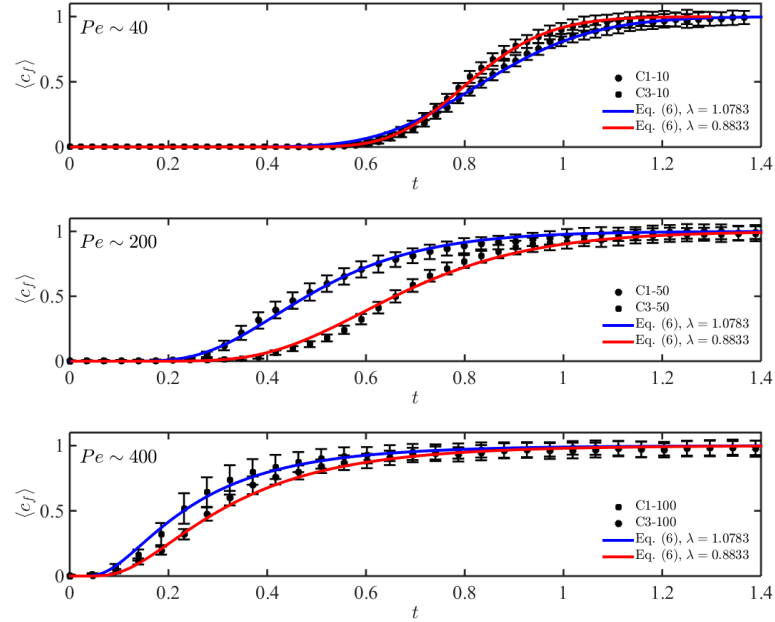


Figure 3.5: Comparison between experimental data collected at  $\tilde{x} = 2$  mm along the channel patterned by cylinder structures C1 (squares) and C3 (circles) and the fitted analytical solution (3.6) (line) for different values of the Péclet number. The error bars represent one standard deviation of the average concentration from its mean value.

mark experiments to model coupled channel/fracture-matrix systems, (ii) the upscaled model (3.6) can be successfully used to investigate non-reactive solute transport in fractured systems embedded permeable matrices for a wide range of Péclet numbers, (iii) the fitted permeability values in the macroscopic model are physical and correctly represent different topologies, i.e. permeability is lower for more tortuous patterns and higher for more porous topologies, and (iv) a unique matrix permeability can be determined from tracer experiments when  $\lambda \leq 1$ .

Ling, B., Oostrom, M., Tartakovsky, A., Battiato, I., (2016), 'Patterned microchannels as benchmark experiments for transport in fracture-matrix systems'. *Environmental Science and Technology*, Submission code: es-2016-05929v.

# Chapter 4

## Micro-scale Multi-phase Flow in Porous Media

### 4.1 Introduction

In the last several decades, porescale two-phase flow has attracted significant attention [39, 272, 180, 181, 130]. At the pore scale, multiphase flow is governed by the Navier-Stokes (NS) equations subject to the Young-Laplace boundary condition at the fluid-fluid interface and the Young condition at the fluid-fluid-solid interface[365]. These equations are highly non-linear because of the moving fluid-fluid and fluid-fluid-solid boundaries, which presents a significant challenge for obtaining accurate numerical solutions [218, 313]. A number of mathematical formulations have been proposed to simplify the solution of these equations, including methods that describe interface dynamics implicitly by means of a “color” function[329] (e.g., the

volume of fluid[133], density functional method, and phase-field method[295]). Various formulations have been used to describe the dynamics of a fluid-fluid-solid interface, including static and dynamic contact angles, energy-balance considerations, and pairwise forces. Various numerical methods, including mesh-based finite volume and mesh-less Smoothed Particle Hydrodynamics, have been used to solve the resulting Navier-Stokes equations. Other (so-called “mesoscale”) methods (e.g., Lattice-Boltzmann and Dissipative Particle Dynamics) have been also applied to model multiphase flow in porous media. The resulting models have different degrees of complexity in representing fluid-fluid-solid interactions, numerical accuracy, and the computational cost (for review of numerical methods for multiphase porescale flow see [207]).

A natural question to ask is, what model complexity and numerical accuracy are sufficient to correctly model multiphase flow on the pore scale? The qualifier “correctly” in this question is important because, in many studies, the porescale models are verified and validated only in a “weak” sense, i.e., by comparing the average solution (or its properties, such as pressure-saturation relationship) obtained from a numerical model and the corresponding experiment. Not that the comparison of average properties of solutions lacks merit; however, it is also reasonable to require a porescale numerical model to reproduce porescale properties of the solution accurately. Comparison with well-controlled, porescale multiphase flow experiments is a reasonable way to validate and verify a numerical model. The answer to the preceding question is complicated by, at least, three factors: 1) depending on the initial and

boundary conditions, the equations describing multiphase flow could be unstable, i.e., small perturbations in initial and boundary conditions may lead to large differences in the solution; 2) the exact geometry and roughness of the flow domain boundaries (i.e., the pore geometry), even when possible to precisely measure, are usually impractical to fully resolve; and 3) initial conditions are difficult to control in an experiment and exactly reproduce in the numerical model. Still, even if these challenges could be overcome, reproducible experimental results are needed to conduct a validation study.

Quasi-two-dimensional microfluidic cells are often used to experimentally study porescale flow[68, 370, 369]. They afford better control and monitoring of flow dynamics than three-dimensional small-column experiments. Therefore, the microcell experiments are perfect candidates to generate results for a validation study. Often, microfluidic studies use a pore geometry made of a uniform array of cylinders (e.g., [370]). Multiphase flows in such pore structures are particularly difficult to reproduce in both experiments and numerical simulations for several reasons: 1) small manufacturing defects brake “symmetry” and significantly affect the multiphase flow; 2) even if the actual manufactured geometry could be exactly measured, the differences between the prescribed (design) and actual geometry could be impractical to resolve in a numerical model; and 3) small time-variations in the flux rate generated by syringe pumps may lead to significant changes in the final distribution of fluid phases. In [97], multiphase flow in both heterogeneous and homogeneous pore structures was studied, and the “point-by-point” difference in displacement patterns, obtained experimentally and numerically, was found to be from 17 to 30% in the

heterogeneous porous structure and from 30 to 40% in the homogeneous domain depending on a numerical model used. The reproducibility of experimental results was not addressed in [97].

In the first part of this work, we study the question of reproducibility of experiments by repeating simulations in six microcells with the same (up to the manufacturing error) geometry. We use a microcell with highly non-uniform pore-size distribution to minimize the effect of small deviations from the design pore geometry and injection rate on the experimental results. In all experiments, a microcell is initially occupied with a wetting fluid, and a non-wetting fluid is injected through the left boundary for 15 s with a constant flux  $q$  using a high-precision pump (variations in the injections rate are less than 5% per manufacturer's specification). Then, a non-wetting fluid is injected through the right port until the saturation of the non-wetting fluid reaches steady state. Our study shows a significant variability in the porescale distribution of fluid phases, interface area, and saturation. In the second part of our study, we conduct two- and three-dimensional simulations with constant and randomly varying injection rates to capture average behavior and variability observed in the experiments. We use a commercial finite volume code STAR-CCM+ (CD-adapco, Melville, NY, USA) in our numerical study. Our results show that the three-dimensional simulation with a deterministic flux  $q$  better captures the mean behavior observed in the experiment than the two-dimensional model with the constant  $q$ . The two-dimensional simulations with randomly varying (around the prescribed in the experiments) flux capture the variability observed in the experiments, but the average behaviors, found

in the simulations and experiments, differ. We also determine that the average behavior of stochastic simulations differs from the corresponding deterministic simulations because of strong non-linearity of the governing equations.

## 4.2 Microfluidic experiments

### 4.2.1 Design and photolithography

The reproducibility of pore-scale multiphase flow experiments was investigated in a microfluidic device shown in Figure 4.1-a. For this study, six replicas were manufactured of the device and up five experiments were conducted for each replica. To minimize the effect of pore-geometry deviations (manufacturing defects) from the prescribed geometry, pore-scale heterogeneity is introduced in the form of a preferential flow path with a width  $w_{t1}$ . An exterior piping system is connected to the inlet and outlet, which have the width  $w_{t2}$ . The design dimensions of the micromodel are provided in Table 4.1.

The micromodels (Figure 4.1-b) were fabricated using standard photolithographic techniques. The six replicas of the designed pore geometry were printed on a single photomask. Then, an SU-8 negative photo-resistant material was coated onto a 4-inch diameter silicon wafer. The cell base was made from the hydrophobic polydimethylsiloxane (PDMS) material “baked” in an oven for over 12 hours at  $75^{\circ}C$  (Figure 4.1-b). To make the wetting properties of the cell’s glass top the same as



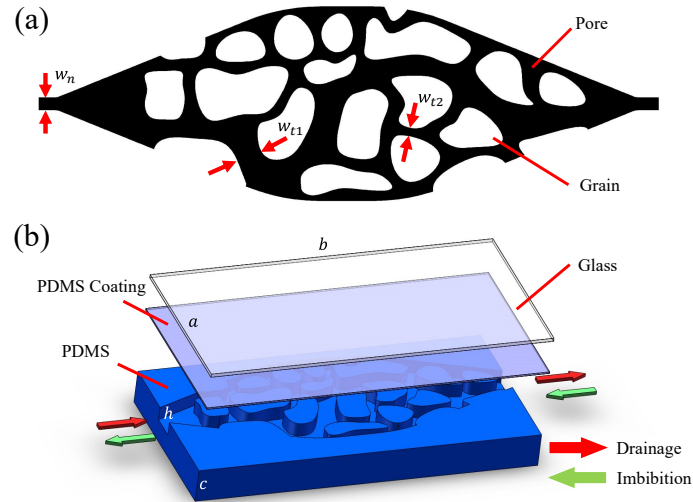


Figure 4.1: (a) Pore Structure. Pore spaces are shown in black, and the solid phase is in white; (b) Three-dimensional configuration.

that of the PDMS base, the glass was also coated with a thin layer of PDMS. To achieve chemically-stable hydrophobic interior surfaces, the assembled cells are placed for an additional 48 hours in an oven at  $200^{\circ}C$ .

#### 4.2.2 Experimental design

The fluids were injected and removed from a micromodel using a piping system shown in Figure 4.2. To perform drainage and imbibition phases of the experiment, glass syringes (1 mL Glass Syringe, Hamilton) containing the wetting fluid (hexadecane) and the non-wetting fluid (DI-water) were used. A series of valves were used to enable and disable flow paths during these phases (Figure 4.2-c). This experimental design allowed for a smooth switching from the drainage to the imbibition phase

Table 4.1: Micromodel Dimensions

Symbols (Figure 4.1)	Length ( $mm$ )
$a \times b \times c$	$5 \times 18 \times 5$
$h$	0.03
$w_n$	0.1
$w_{t1}$	$\sim 0.4 - 0.5$
$w_{t2}$	$\sim 0.1$

without cross- contamination, while preventing formation of air bubbles. A precision syringe pump (NE-4002X, New Era Pump System) was used to produce a constant injection rate.

To conduct an experiment, a micromodel was placed horizontally on a microscope stage (Prior Scientific Instruments LTD.) to minimize the effect of gravity. Fluid displacement was visualized by a microscope (Nikon Eclipse-2000TiE) with a  $4\times$  magnifying lens and a  $3.23\mu m$  spatial resolution. Light is provided by a high-intensity light source (Nikon Intensilight C-HGFIE), and images are recorded using a monochrome digital charge-coupled device (CCD) camera. All devices are connected to a computer, and the recording speed, exposure time, and shutter time are set by the imaging software NIS-Elements (Nikon). Before the start of each experiment, the micromodel was first saturated with the wetting fluid (hexadecane). Then, during the drainage phase, the non-wetting fluid (DI water) is injected for 15 s. Subsequently, the piping system

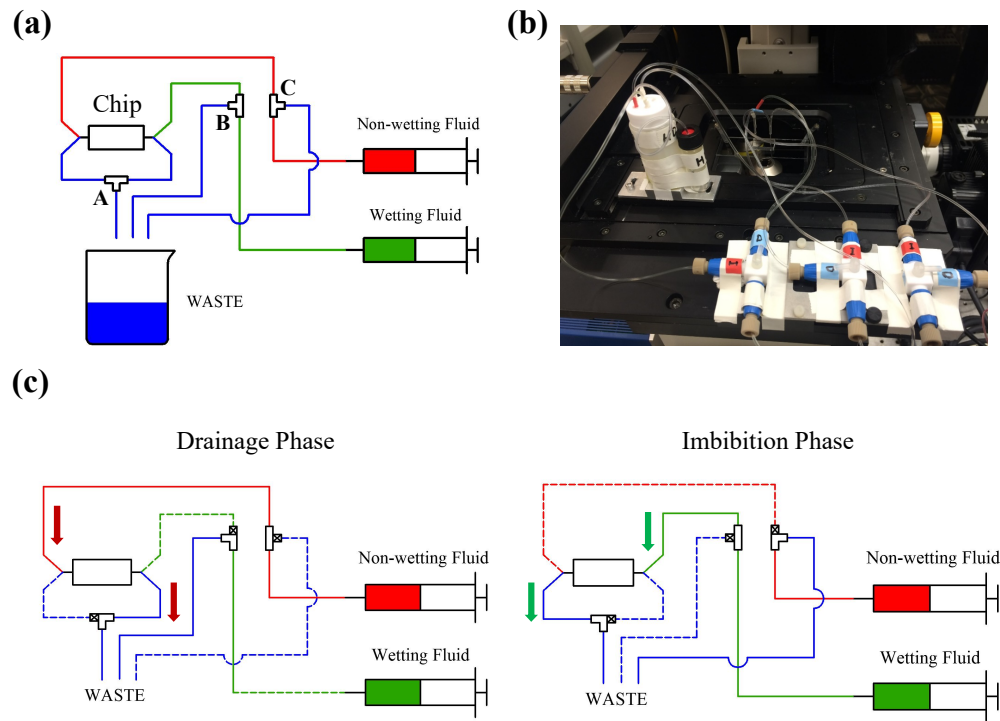


Figure 4.2: (a) Illustration of the piping system; (b) Realization; (c) Flow path in different phases of the experiment.

is switched for imbibition, and the wetting fluid is injected until the steady state is reached.

Table 4.2 includes the properties of both fluids, prescribed injection velocity, and the resulting viscosity ratio ( $M = \mu_{nw}/\mu_w$ ) and capillary number ( $Ca = \mu_{nw}U/\sigma$ ). The static contact angle ( $\theta$ ) between the two fluids and PDMS surface was measured in the cell inlet (Figure 3) from an auxiliary experiment where wetting fluid was injected for a short period of time. The measured values of  $\theta$  are between  $16^\circ$  to  $18^\circ$ , with an

averaged value of  $16.8^\circ$ .

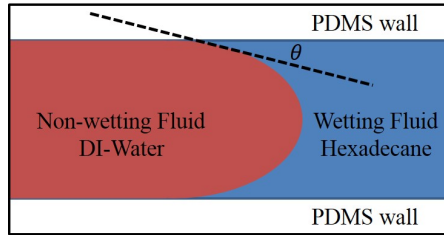


Figure 4.3: Definition of the Non-wetting/wetting fluid and contact angle.

Table 4.2: Wetting (hexadecane) and non-wetting (DI water) fluid properties

Property	Value
non-wetting fluid viscosity ( $\mu_{nw}, cP$ )	1.02
wetting fluid viscosity ( $\mu_w, cP$ )	3.34
surface tension ( $\sigma, mN/m$ )	52.00
contact angle ( $\theta, deg$ )	16.79
injection velocity ( $U, m/s$ )	$9.24 \times 10^{-4}$
$\log(M)$	-0.51
$\log(Ca)$	-4.74

### 4.3 Experimental results

Figure 4.4 shows the results of five experiments in one of the cells (cell D). The first column displays fluids distribution at the drainage cycle end, and the second column displays fluids distribution at the imbibition cycle end. In all experiments at

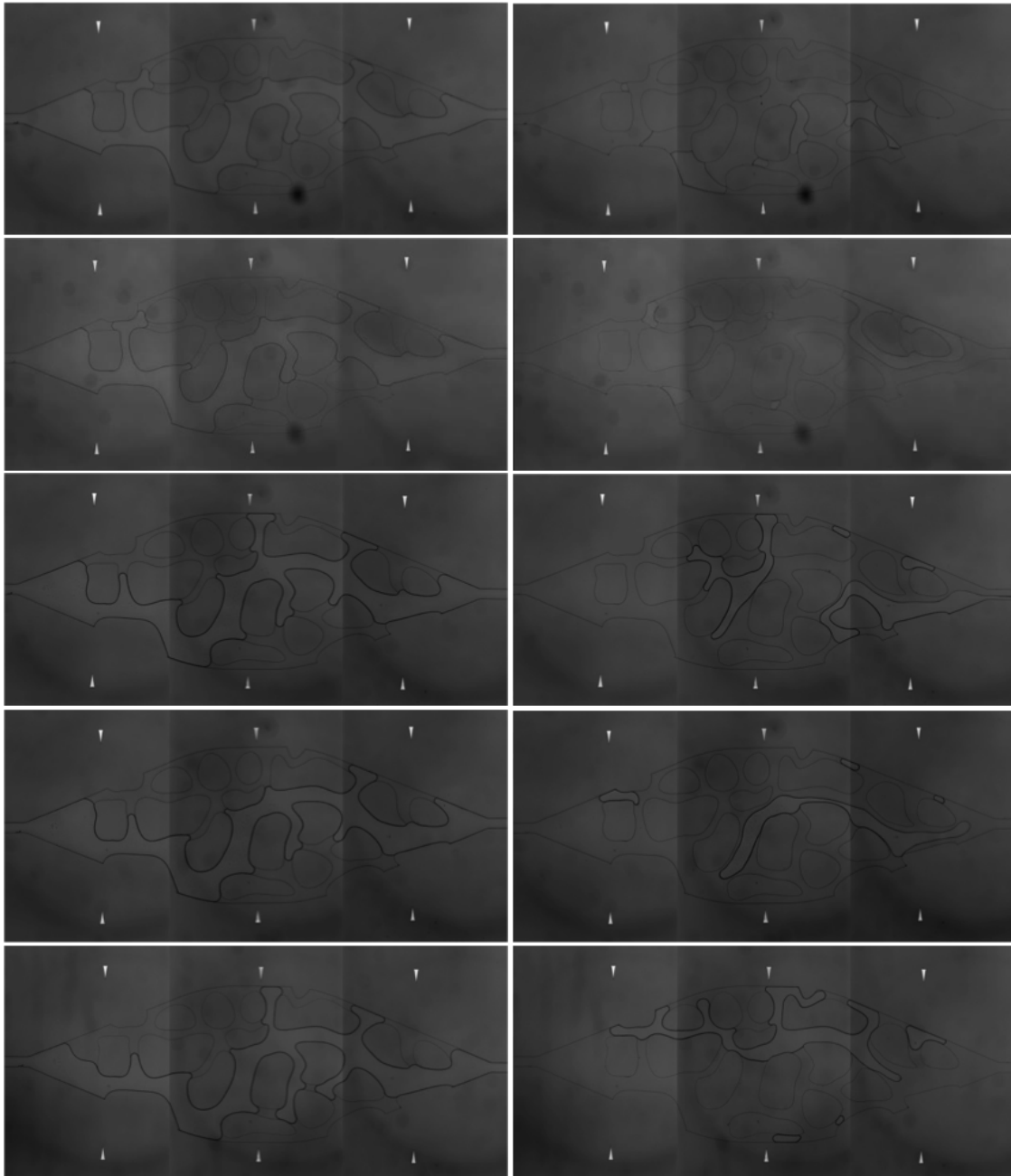


Figure 4.4: Five repetitions (first, second, third, fourth, and fifth rows, respectively) of drainage (first column) and imbibition (second column) in the microcell D.

the drainage cycle end, we observe a similar displacement pattern with the injected non-wetting fluid moving through the “preferential flow path” and forming small “side

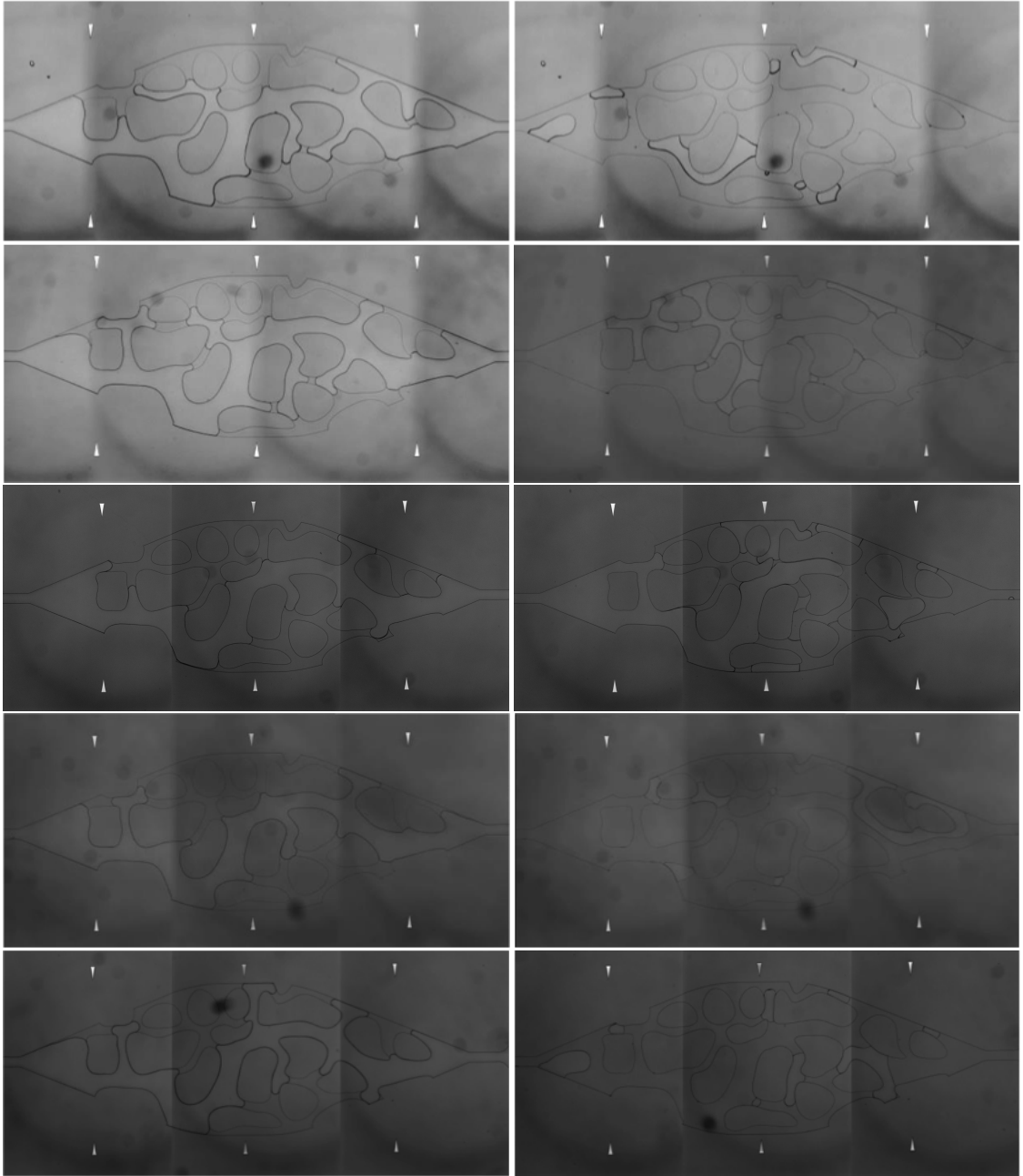


Figure 4.5: The second repetition in cell A (first row), cell B (second row), cell C (third row), cell E (fourth row), and cell F (fifth row) of drainage (first column) and imbibition (second column).

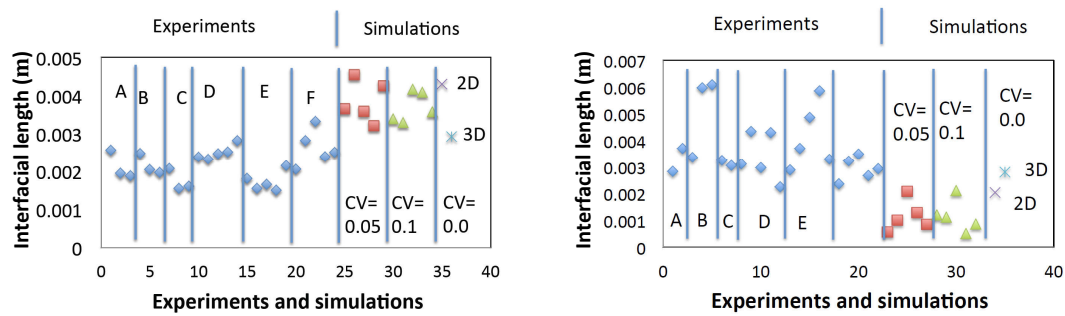


Figure 4.6: Interfacial length at the end of the drainage (left) and imbibition (right) cycles obtained in the experiments and numerical simulations.

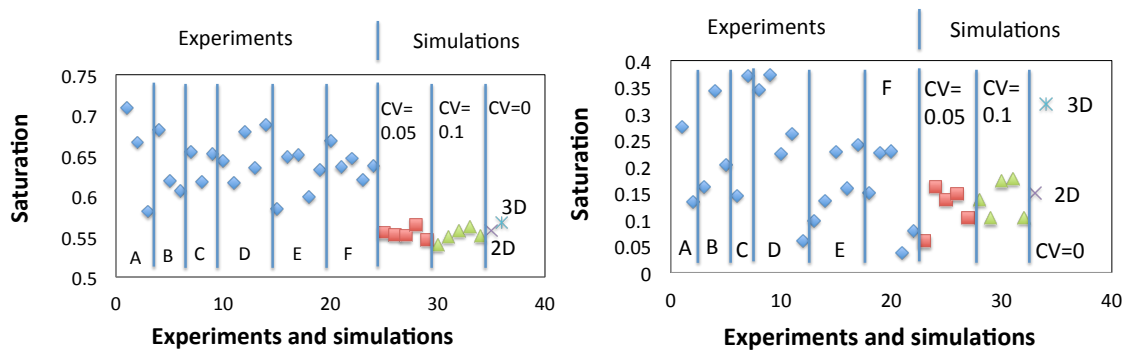


Figure 4.7: Saturation at the end of the drainage (left) and imbibition (right) cycles obtained in the experiments and numerical simulations.

fingers.” The main difference between the experiments is the location and size of the side fingers. The displacement patterns at the imbibition cycle end are completely different in these experiments, with different volume of the non-wetting fluid becoming trapped in different locations. Figure 4.5 shows the drainage and imbibition patterns observed in five different cells. As in Figure 4.4, here the fluid distribution is more repeatable at the drainage cycle end and less repeatable at the imbibition cycle end.

Figures 4.6 and 4.7 show the interface length (in mm) and saturation of the non-wetting fluid at the end of the drainage and imbibition cycles observed in different experiments in all six cells. It is evident that variability in the experiments is higher across different cells than within individual cells, which we attribute to the small deviations in the cells' pore geometry from the design geometry that stems from manufacturing defects.

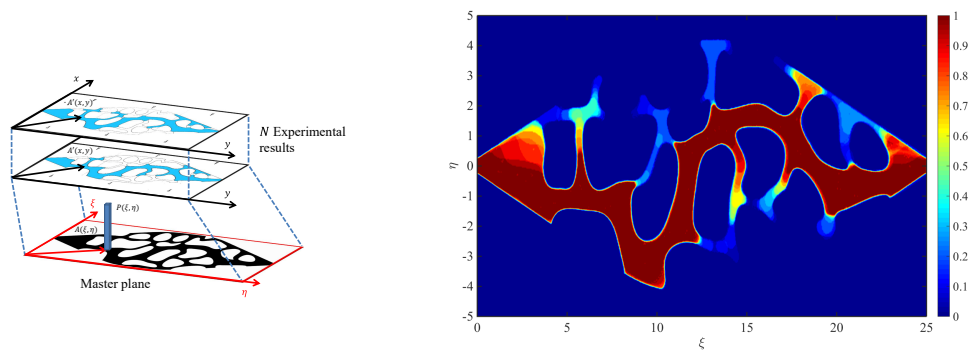


Figure 4.8: **Left:** Definition of the master plane and the mapping process; **Right:**  $p(\xi, \eta)$  of all the experimental results.

To quantify variability in drainage experiments, we divide the domain in a lattice with indices  $\xi$  and  $\eta$ , map the fluid distributions at the end of the drainage cycle, and construct a histogram  $p(\xi, \eta)$  of a non-wetting fluid occupying each lattice point (Figure 4.8). The histogram shows that the largest variability between the experiments is in the size of the side fingers.



## 4.4 Numerical simulations

To understand the source of variability observed in the experiments, we model them using the software package STAR-CCM+. STAR-CCM+ employs a finite volume discretization on unstructured grids and the volume of fluid method to implicitly track the interface between two fluids. Previous studies (e.g., [327, 362]) have demonstrated the accuracy of STAR-CCM+ for pore-scale modeling in complex pore geometries.

### 4.4.1 Deterministic two- and three-dimensional simulations

It is common to assume that flow in (three-dimensional) microfluidic cells can be accurately described by the two-dimensional Navier-Stokes equations, given that the cell depth is much smaller than the smallest pore throat. To test this assumption for the studied system, we simulate the experiment with a fully resolved three-dimensional model and the corresponding depth-averaged two-dimensional model. The fluids distributions obtained from these simulations are shown in Figures 4.9 and 4.10, respectively.

The two dimensional simulations have 37,000 elements, and the three dimensional simulation has 150,000 elements. In both two- and three-dimensional simulations, the time step is  $1e-5$  sec.

We see the same general pattern in the simulations as in the experiments, i.e., the non-wetting fluid follows the same preferential path as in the experiments. However, we can also see some qualitative differences. In the three-dimensional sim-

ulation, the non-wetting fluid completely displaces wetting fluid in the preferential path during the drainage cycle, which is close to what we observe in the experiments. On the other hand, in the two-dimensional simulation, large “lenses” of the wetting fluid are left behind. No such lenses are observed in the experiments. Figures 4.6 and 4.7 show the interface length and saturation of the non-wetting fluid at the end of the drainage and infiltration cycles calculated from the two- and three-dimensional simulations. In the three-dimensional simulation, the interface length agrees better with the mean length in the experiments than the interface length in the two-dimensional simulation. The same is true for the saturation results at the drainage cycle end. The two-dimensional model does slightly better than the three-dimensional model in predicting saturation at the imbibition cycle end. Still, given the large variability of the imbibition displacement patterns in the experiments, this easily could be a coincidence. Therefore, we conclude that the three-dimensional model describes the experimental results more accurately than the two-dimensional model. We should note that both the two- and three-dimensional models predict significantly larger volumes of the wetting fluid trapped in the “corners” of the preferential path during drainage than observed in the experiments. We attribute this to the fact that, because of the manufacturing defects, the corners in the cells are not as sharp as designed (and modeled in the simulations).

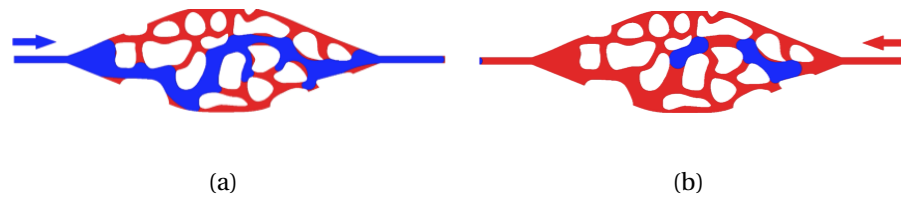


Figure 4.9: Three-dimensional simulation of (a) drainage and (b) imbibition with constant injection velocity  $9.24 \times 10^{-4}$  m/s.

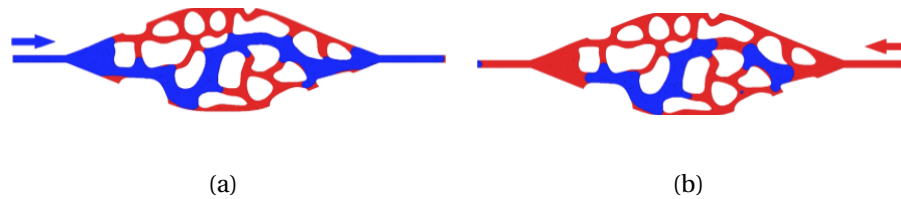


Figure 4.10: Two-dimensional simulation of (a) drainage and (b) imbibition with constant injection velocity  $9.24 \times 10^{-4}$  m/s.

#### 4.4.2 Stochastic two-dimensional simulations

Variability in different experiments in the same cells can be attributed to small variations in the injection rate of syringe pumps. To test this hypothesis, we simulate the experiment with a randomly varying injection rate. We conduct two sets of five simulations with the coefficient of variance of the injection rate set to 0.05 (Figure 4.11) and 0.1 (Figure 4.12).

The coefficient of variance (CV) of 0.05 corresponds to the pump accuracy (the syringe pump used in this study has a regular accuracy  $\pm 1 \sim 5\%$  based in the flow rate). Because of the high computational cost of the three-dimensional model, we only use the two-dimensional model in this study. Both figures show the same pattern as in

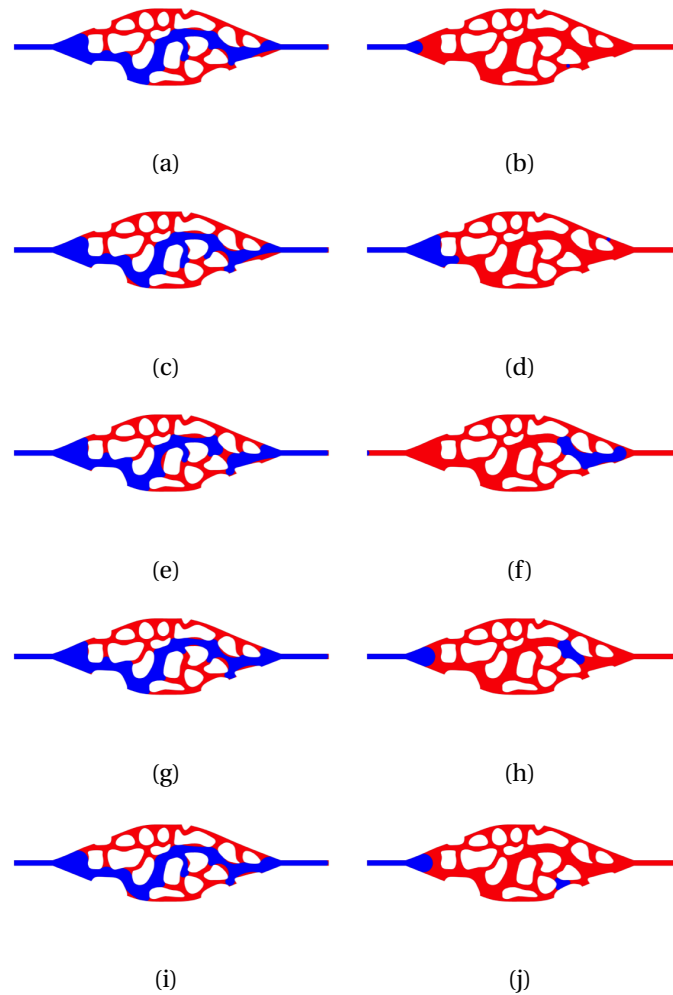


Figure 4.11: Two-dimensional simulation of (left column) drainage and (right column) imbibition with random injection velocity with mean  $9.24 \times 10^{-4}$  m/s and  $CV=0.05$ . Different rows are different realizations.

the experiments. During drainage, the non-wetting fluid saturates the preferential path and forms side fingers, which vary in different (stochastic) simulations. At the imbibition cycle end, there is very high variability in the amount and location of the trapped non-wetting phase. Figures 4.6 and 4.7 show the interface length and saturation of the non-wetting fluid at the end of the drainage and infiltration cycles

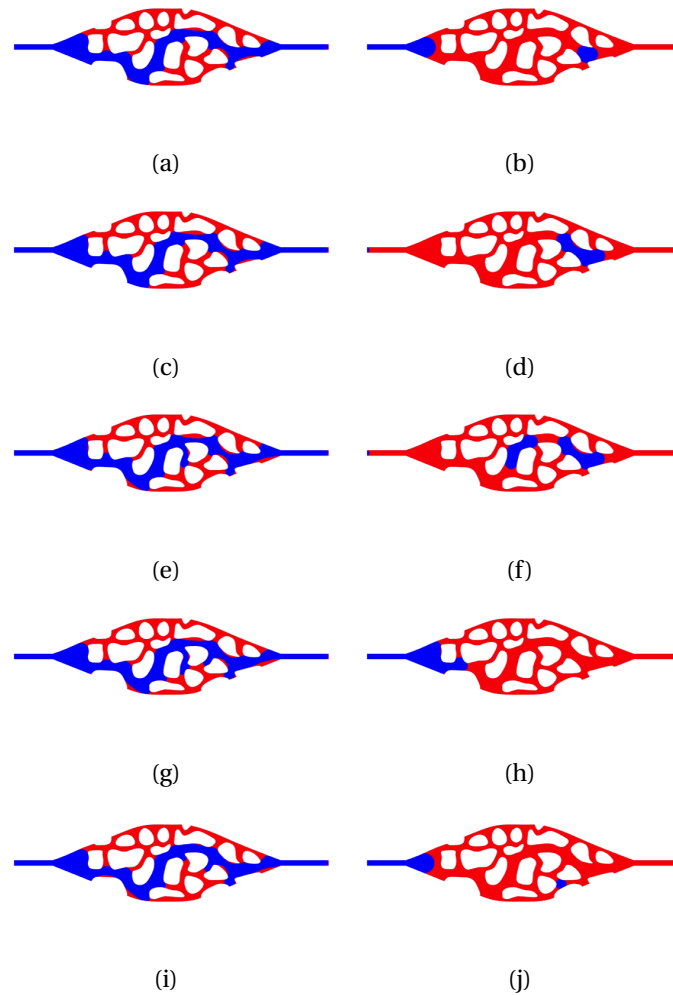


Figure 4.12: Two-dimensional simulation of (left column) drainage and (right column) imbibition with random injection velocity with mean  $9.24 \times 10^{-4}$  m/s and CV=0.1. Different rows are different realizations.

calculated from the stochastic simulations. Figure 4.13 shows CV of the interface length at the end of the drainage and imbibition cycles obtained in experiments and stochastic simulations. We can see that CV differs for each experimental cell. For the drainage cycle, the CVs obtained from stochastic simulations are within the range of CVs observed in the experiments. For imbibition, the simulations overestimate CV. The

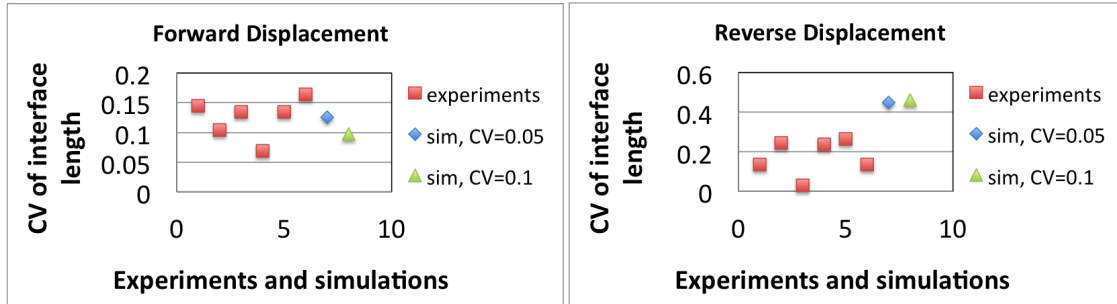


Figure 4.13: Coefficient of variance of the interface length at the end of drainage (left) and imbibition (right) cycles observed in the experiments and computed from the stochastic simulations.

simulations with different CVs of the injection rate result in approximately the same CV of the interface length. It is also important to note that the mean interface length and saturation obtained from the stochastic simulations differs from the “mean-field” interface length and saturation obtained from the two-dimensional deterministic simulation. Our results also show that the mean of stochastic simulations agrees better with the average behavior observed in the experiments than the results of the two-dimensional deterministic simulation.

The capillary number in the experiments (and the previously presented simulations) is  $Ca = 1.82 \times 10^{-5}$ . It is known that instability of immiscible flow increases with the decreasing  $Ca$ . In Figure 4.14, we show the results of five stochastic simulations with  $Ca = 1.82 \times 10^{-3}$ , which is 100 times larger than in the experiments. The fluid distribution at the displacement cycle end is nearly the same in all simulations. On the other hand, the fluids distribution at the imbibition cycle end significantly varies between simulations, even for this relatively large  $Ca$ .

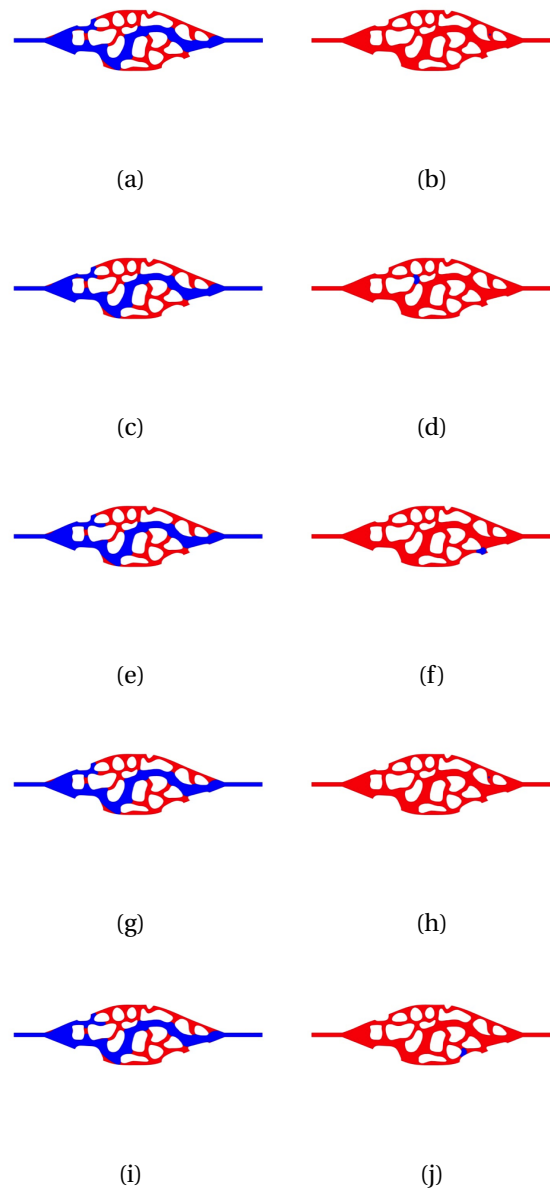


Figure 4.14: Two-dimensional simulation of (left column) drainage and (right column) imbibition with random injection velocity with mean  $9.24 \times 10^{-1}$  m/s and CV=0.1. Different rows are different realizations.

The “point-wise” histogram of the non-wetting fluid distribution at the drainage cycle end, obtained from the stochastic simulations, is shown in Figure 4.15. As in

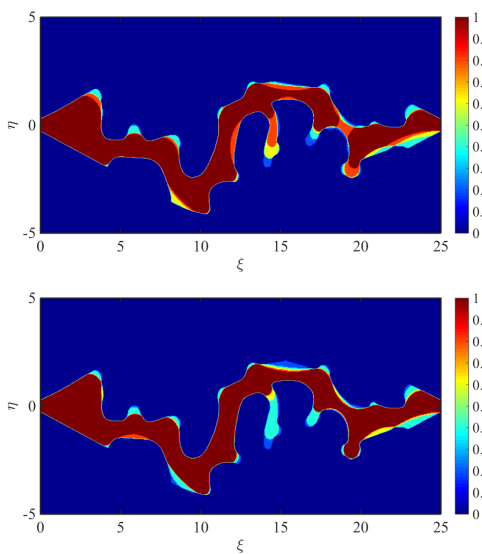


Figure 4.15: **Top:**  $p(\xi, \eta)$  of simulation with variance of 0.05; **Bottom:**  $p(\xi, \eta)$  of simulation with variance of 0.1.

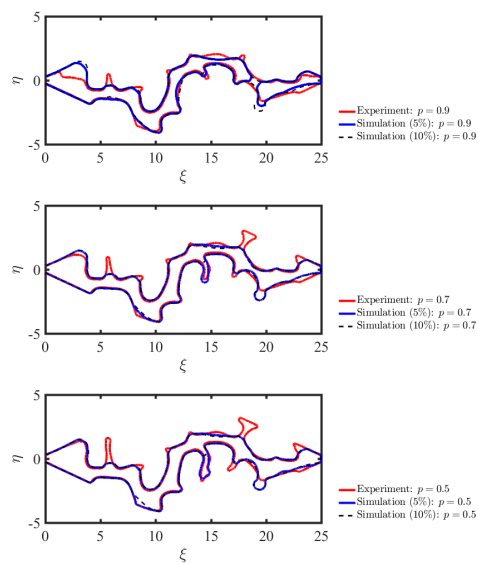


Figure 4.16: Contour lines with  $p = 0.9$ ,  $p = 0.7$ ,  $p = 0.5$ .



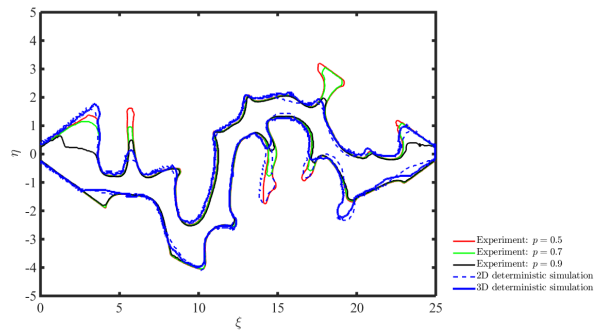


Figure 4.17: Contour lines comparison between the deterministic simulations with the experimental results with different  $p$  values.

the experiments, variability in the stochastic simulations is mainly in the side fingers size. Experiments also exhibit variability in the fluids distribution in the preferential flow path, including breakup and detachment from the solid grains of the non-wetting fluid in some simulations. Unexpectedly, the variability is more pronounced in the simulations with the smaller variance of the injection rate.

In Figure 4.16, we compare the contour lines of simulation and experimental histograms for several  $p$  values. There is a significant difference between the simulation and experimental  $p = 0.9$  contour lines. Contour lines corresponding to  $p = 0.5$  and  $0.7$  agree within 5% for the side fingers at the lower part of the domain, but they disagree for the upper side fingers. A similar comparison (Figure 4.17) between the deterministic simulations and experimental results shows that the three-dimensional simulation predicts the experimental results more accurately than the two-dimensional simulation.

## 4.5 Conclusions

Our experimental and computational studies were conducted for the low capillary number  $Ca = 1.82 \times 10^{-5}$ . Improvement of reproducibility was shown with experiments performed using the same cell in the drainage phase. Large variability was observed when comparing experiments using different replicas of the same design. Even greater variation in the experimental results were noted at the imbibition cycle end.

Numerical simulations using the same parameters as the experiments were performed in the exact same geometry both in two and three dimensions. To reveal the impact of fluctuations in the pumping flow rate, we simulated the flow both deterministically and statistically. We found that the deterministic three-dimensional model is more accurate than the two-dimensional model.

Randomly varying (in time) the injection rate quantitatively captured the variability observed in the experiments. The average behavior of stochastic simulations was in better agreement from the corresponding deterministic simulation and better agrees with the average behavior observed in the experiments.

For the larger capillary number ( $Ca = 1.82 \times 10^{-3}$ ), we observed nearly zero variability in the results of stochastic numerical simulations of the drainage cycle, suggesting that the drainage experiments could be “reproducible” for higher  $Ca$ . Variability in the imbibition results remain high, even for this relatively large  $Ca$ . To confirm our conclusion that higher  $Ca$  is needed to obtain reproducible experimental

results, additional experimental studies are needed.

Ling, B., Bao, J., Oostrom, M., Battiato, I., Tartakovsky, A., (2016), 'Modeling variability of porescale multiphase flow experiments'. *Advanced Water Resource*, *Submission code: ADWR-2016-349*.

# Chapter 5

## Conclusions

This dissertation leads to the following major conclusions:

1. We show that by means of perturbation theory and asymptotic analysis, a set of upscaled equations describing mass transport in a coupled channel-porous matrix system can be derived, and an analytical expression relating the dispersion coefficient with the properties of the surface, namely porosity and permeability, can be achieved by perturbative expansion and homogenization method. Our analysis in Chapter 2 shows that impact of surface effective properties on the dispersion coefficient strongly depends on the magnitude of Péclet number, i.e., on the interplay between diffusive and advective mass transport. Additionally, we demonstrate different scaling behaviors of the dispersion coefficient for thin or thick porous matrices.
2. Our analysis shows the possibility of controlling the dispersion coefficient, i.e.

transversal mixing, by either active (i.e. changing the operating conditions) or passive mechanisms (i.e. controlling matrix effective properties) for a given Péclet number. By elucidating the impact of matrix porosity and permeability on solute transport, our upscaled model lays the foundation for the improved understanding, control and design of microporous coatings with targeted macroscopic transport features.

3. We run a series of pore-scale transport experiments on polydimethylsiloxane (PDMS) micromodels with surfaces patterned with different microstructures (e.g. pillars and riblets) to test the hypothesis that such micromodels can be used as benchmark experiments for validation of flow and transport models in coupled channel/matrix systems. Temporal and spatial high resolution data are collected at the pore scale, and used to calculate averaged (continuum-scale) quantities. The latter, in the form of tracer benchmark experiments, are used in conjunction with the theoretical models developed in the first part of the thesis to determine effective geometrical properties of the micropattern (i.e. its effective medium representation). Our approach (i) provides an alternative way of measuring permeability of micropatterned surfaces while circumventing the difficulty of achieving precise measurements of pressure gradient in micromodels using traditional methods, (ii) supports the hypothesis that micropatterned surfaces can be represented as effective media, and experiments on patterned microchannels employed as benchmarks for coupled fracture/matrix systems.

The latter result is confirmed for both permeable (arrays of cylinders) and nearly impermeable (transverse riblets) microstructures.

4. Lack of reproducibility is a notorious and intrinsic challenge of multiphase transport in porous media experiments due to the inherently unstable nature of multiphase flow dynamics. In the second part of the thesis, we investigate the reproducibility of multiphase flow experiments in porous media and the possible use of microfluidic data for validation of pore-scale multiphase numerical codes. Specifically, we perform a set of drainage and imbibition experiments in six identical microfluidic cells. We observe significant variations in the experimental results, which are smaller during the drainage stage and larger during the imbibition stage. We are able to improve the overall reproducibility by introducing heterogeneity in the pore structure at a length scale larger than the characteristic length scale associated to sub-pore scale roughness, which controls unstable displacement in perfectly regular (homogenous) pore-structures.
5. Finally, we establish a general framework to quantify the variability in multiphase flow experiments. By means of image recognition techniques and stochastic analysis, we propose a phase map at the pore-scale which shows the pointwise experimental probability that any given point be occupied by a certain (wetting or nonwetting) fluid. Computational simulations are then conducted using commercial software STAR-CCM+ both with constant and randomly varying injection rates. Stochastic simulations are able to capture the experimental

variability and appear to be a more appropriate framework to describe unstable pore-scale displacement in multiphase transport.

# Appendix A

## Derivation of the upscaled equations

### A.1 Asymptotic Expansion

Substituting (2.26) into (2.24a) and (2.24b) leads to

$$\begin{aligned}
 & \epsilon^{1-\alpha} \left( \frac{\partial c_f^{(0)}}{\partial t} + \sqrt{\epsilon} \frac{\partial c_f^{(1)}}{\partial t} + \epsilon \frac{\partial c_f^{(2)}}{\partial t} \right) + \epsilon^{1/2-\alpha} \left( u_f \frac{\partial c_f^{(0)}}{\partial \xi} + \sqrt{\epsilon} u_f \frac{\partial c_f^{(1)}}{\partial \xi} + \epsilon u_f \frac{\partial c_f^{(2)}}{\partial \xi} \right) \\
 & = \epsilon D_f \left( \frac{\partial^2 c_f^{(0)}}{\partial \xi^2} + \sqrt{\epsilon} \frac{\partial^2 c_f^{(1)}}{\partial \xi^2} + \epsilon \frac{\partial^2 c_f^{(2)}}{\partial \xi^2} \right) + D_f \left( \sqrt{\epsilon} \frac{\partial^2 c_f^{(1)}}{\partial y^2} + \epsilon \frac{\partial^2 c_f^{(2)}}{\partial y^2} \right) \quad (\text{A.1})
 \end{aligned}$$

and

$$\begin{aligned}
 & \epsilon^{1-\alpha} \left( \frac{\partial c_m^{(0)}}{\partial t} + \sqrt{\epsilon} \frac{\partial c_m^{(1)}}{\partial t} + \epsilon \frac{\partial c_m^{(2)}}{\partial t} \right) + \epsilon^{1/2-\alpha} \left( u_m \frac{\partial c_m^{(0)}}{\partial \xi} + \sqrt{\epsilon} u_m \frac{\partial c_m^{(1)}}{\partial \xi} + \epsilon u_m \frac{\partial c_m^{(2)}}{\partial \xi} \right) \\
 & = \epsilon D_{mx} \left( \frac{\partial^2 c_m^{(0)}}{\partial \xi^2} + \sqrt{\epsilon} \frac{\partial^2 c_m^{(1)}}{\partial \xi^2} + \epsilon \frac{\partial^2 c_m^{(2)}}{\partial \xi^2} \right) + D_{my} \left( \sqrt{\epsilon} \frac{\partial^2 c_m^{(1)}}{\partial y^2} + \epsilon \frac{\partial^2 c_m^{(2)}}{\partial y^2} \right) \quad (\text{A.2})
 \end{aligned}$$



respectively. Given  $\alpha < 1/2$ , we collect terms of like-power of  $\epsilon$  as follows,

$$\begin{aligned} & \sqrt{\epsilon} \left( \epsilon^{-\alpha} u_f \frac{\partial c_f^{(0)}}{\partial \xi} - D_f \frac{\partial^2 c_f^{(1)}}{\partial y^2} \right) + \epsilon \left( \epsilon^{-\alpha} \frac{\partial c_f^{(0)}}{\partial t} + \epsilon^{-\alpha} u_f \frac{\partial c_f^{(1)}}{\partial \xi} - D_f \frac{\partial^2 c_f^{(0)}}{\partial \xi^2} - D_f \frac{\partial^2 c_f^{(2)}}{\partial y^2} \right) \\ & + \epsilon \sqrt{\epsilon} \left( \epsilon^{-\alpha} \frac{\partial c_f^{(1)}}{\partial t} + \epsilon^{-\alpha} u_f \frac{\partial c_f^{(2)}}{\partial \xi} - D_f \frac{\partial^2 c_f^{(1)}}{\partial \xi^2} \right) = O(\epsilon^2), \end{aligned} \quad (\text{A.3a})$$

$$\sqrt{\epsilon} \left( \epsilon^{-\alpha} u_m \frac{\partial c_m^{(0)}}{\partial \xi} - D_{my} \frac{\partial^2 c_m^{(1)}}{\partial y^2} \right) \quad (\text{A.3b})$$

$$\begin{aligned} & + \epsilon \left( \epsilon^{-\alpha} \frac{\partial c_m^{(0)}}{\partial t} + \epsilon^{-\alpha} u_m \frac{\partial c_m^{(1)}}{\partial \xi} - D_{mx} \frac{\partial^2 c_m^{(0)}}{\partial \xi^2} - D_{my} \frac{\partial^2 c_m^{(2)}}{\partial y^2} \right) \\ & + \epsilon \sqrt{\epsilon} \left( \epsilon^{-\alpha} \frac{\partial c_m^{(1)}}{\partial t} + \epsilon^{-\alpha} u_m \frac{\partial c_m^{(2)}}{\partial \xi} - D_{mx} \frac{\partial^2 c_m^{(1)}}{\partial \xi^2} \right) = O(\epsilon^2). \end{aligned} \quad (\text{A.3c})$$

Equations (A.3a) and (A.3c) leads to a cascade of equations for the unknown functions

$c_j^{(i)}$ . Specifically, for  $c_f^{(i)}$  and  $c_m^{(i)}$  we obtain

$$\frac{\partial^2 c_f^{(1)}}{\partial y^2} = \epsilon^{-\alpha} \frac{u_f}{D_f} \frac{\partial c_f^{(0)}}{\partial \xi}, \quad (\text{A.4a})$$

$$\epsilon^{-\alpha} \frac{\partial c_f^{(0)}}{\partial t} + \epsilon^{-\alpha} u_f \frac{\partial c_f^{(1)}}{\partial \xi} = D_f \frac{\partial^2 c_f^{(0)}}{\partial \xi^2} + D_f \frac{\partial^2 c_f^{(2)}}{\partial y^2}, \quad (\text{A.4b})$$

$$\epsilon^{-\alpha} \frac{\partial c_f^{(1)}}{\partial t} + \epsilon^{-\alpha} u_f \frac{\partial c_f^{(2)}}{\partial \xi} = D_f \frac{\partial^2 c_f^{(1)}}{\partial \xi^2}, \quad (\text{A.4c})$$

and

$$\frac{\partial^2 c_m^{(1)}}{\partial y^2} = \epsilon^{-\alpha} \frac{u_m}{D_{my}} \frac{\partial c_m^{(0)}}{\partial \xi}, \quad (\text{A.5a})$$

$$\epsilon^{-\alpha} \frac{\partial c_m^{(0)}}{\partial t} + \epsilon^{-\alpha} u_m \frac{\partial c_m^{(1)}}{\partial \xi} = D_{mx} \frac{\partial^2 c_m^{(0)}}{\partial \xi^2} + D_{my} \frac{\partial^2 c_m^{(2)}}{\partial y^2}, \quad (\text{A.5b})$$

$$\epsilon^{-\alpha} \frac{\partial c_m^{(1)}}{\partial t} + \epsilon^{-\alpha} u_m \frac{\partial c_m^{(2)}}{\partial \xi} = D_{mx} \frac{\partial^2 c_m^{(1)}}{\partial \xi^2}, \quad (\text{A.5c})$$

respectively. Expanding the interface conditions (2.22) yields,

$$[c_f^{(0)} + \sqrt{\epsilon} c_f^{(1)} + \epsilon c_f^{(2)}]_{y=0} = [c_m^{(0)} + \sqrt{\epsilon} c_m^{(1)} + \epsilon c_m^{(2)}]_{y=0}, \quad (\text{A.6})$$

and

$$\left[ \sqrt{\epsilon} \frac{\partial c_f^{(1)}}{\partial y} + \epsilon \frac{\partial c_f^{(2)}}{\partial y} \right]_{y=0} = \left[ \sqrt{\epsilon} \frac{\phi D_{my}}{D_f} \frac{\partial c_m^{(1)}}{\partial y} + \epsilon \frac{\phi D_{my}}{D_f} \frac{\partial c_m^{(2)}}{\partial y} \right]_{y=0}. \quad (\text{A.7})$$

Matching like-powers of  $\epsilon$  in (A.7) leads to

$$\left[ \frac{\partial c_f^{(1)}}{\partial y} \right]_{y=0} = \frac{\phi D_{my}}{D_f} \left[ \frac{\partial c_m^{(1)}}{\partial y} \right]_{y=0}, \quad (\text{A.8})$$

$$\left[ \frac{\partial c_f^{(2)}}{\partial y} \right]_{y=0} = \frac{\phi D_{my}}{D_f} \left[ \frac{\partial c_m^{(2)}}{\partial y} \right]_{y=0}. \quad (\text{A.9})$$

The cascade of equations (A.4) and (A.5) subject to the boundary conditions (A.6) and (A.8) can be solved iteratively.

## A.2 Order $\mathcal{O}(\sqrt{\epsilon})$ : $c_f^{(1)}$ and $c_m^{(1)}$ solutions

Integrating equation (A.4a) with respect to  $y$  gives

$$\frac{\partial c_f^{(1)}}{\partial y} = \frac{\epsilon^{-\alpha}}{D_f} \left( \int_0^y u_f dy + M_1 \right) \frac{\partial c_f^{(0)}}{\partial \xi}, \quad (\text{A.10})$$

where the integration constant  $M_1$  is determined by using the no flux condition (2.20) and the velocity profile (3.7a),

$$M_1 = - \int_0^1 u_f dy = - \left( \frac{\Psi}{6} + \frac{A}{2} + B \right), \quad (\text{A.11})$$

and  $A$  and  $B$  are defined in (2.9). Integration of (A.10) yields to

$$c_f^{(1)} = \frac{\epsilon^{-\alpha}}{D_f} \frac{\partial c_f^{(0)}}{\partial \xi} \left( M_2 + M_1 y + \iint_0^y u_f d^2 y \right). \quad (\text{A.12})$$

By postulating  $\langle c_f^{(1)} \rangle = 0$  [216], we can solve for  $M_2$ ,

$$M_2 = - \left( \frac{\Psi}{120} + \frac{A}{24} + \frac{B}{2} + \frac{M_1}{2} \right). \quad (\text{A.13})$$

Inserting (A.13) and (A.11) in (A.12), leads to

$$c_f^{(1)} = M(y) \frac{\epsilon^{-\alpha}}{D_f} \frac{\partial c_f^{(0)}}{\partial \xi}, \quad (\text{A.14})$$

where

$$M(y) = \frac{\Psi}{24} y^4 + \frac{A}{6} y^3 + \frac{B}{2} y^2 + M_1 y + M_2. \quad (\text{A.15})$$

Similarly, double integration of (A.5b) yields to a solution for  $c_m^{(1)}$  in the following form,

$$c_m^{(1)} = \frac{\epsilon^{-\alpha}}{D_{my}} N(y) \frac{\partial c_m^{(0)}}{\partial \xi}, \quad (\text{A.16})$$

where

$$N(y) = \frac{E}{\lambda^2} e^{\lambda y} + \frac{F}{\lambda^2} e^{-\lambda y} - \frac{\Psi}{2\lambda^2} y^2 - \left( \frac{E}{\lambda} - \frac{F}{\lambda} \right) y + N_1 y + N_2, \quad (\text{A.17})$$

$E$  and  $F$  are defined in (2.9) and  $N_1$  and  $N_2$  are integration constants. Constant  $N_1$  is determined by imposing the boundary condition (2.20),

$$N_1 = \frac{E}{\lambda} (1 - e^{-\lambda h}) - \frac{F}{\lambda} (1 - e^{\lambda h}) + \frac{\Psi h}{\lambda^2}, \quad (\text{A.18})$$

and  $N_2$  is determined by imposing  $\langle c_m^{(1)} \rangle = 0$ ,

$$N_2 = - \left[ \frac{E}{h\lambda^3} (1 - e^{-\lambda h}) - \frac{F}{h\lambda^3} (1 - e^{\lambda h}) - \frac{\Psi}{6\lambda^2} h^2 + \frac{h}{2} \left( \frac{E}{\lambda} - \frac{F}{\lambda} \right) - \frac{N_1 h}{2} \right]. \quad (\text{A.19})$$

Equations (A.16), (A.18) and (A.19) fully define  $c_m^{(1)}$ .

### A.3 Order $\mathcal{O}(\epsilon)$ : $c_f^{(2)}$ and $c_m^{(2)}$ solutions

Inserting (A.14) into (A.4b), we obtain

$$\epsilon^{-\alpha} \frac{\partial c_f^{(0)}}{\partial t} + \frac{\epsilon^{-2\alpha}}{D_f} u_f M \frac{\partial^2 c_f^{(0)}}{\partial \xi^2} = D_f \frac{\partial^2 c_f^{(0)}}{\partial \xi^2} + D_f \frac{\partial^2 c_f^{(2)}}{\partial y^2}, \quad (\text{A.20})$$

which provides an equation for  $c_f^{(2)}$ . Averaging (A.20) gives

$$\epsilon^{-\alpha} \frac{\partial c_f^{(0)}}{\partial t} + \frac{\epsilon^{-2\alpha}}{D_f} \langle u_f M \rangle \frac{\partial^2 c_f^{(0)}}{\partial \xi^2} = D_f \frac{\partial^2 c_f^{(0)}}{\partial \xi^2} - D_f \left[ \frac{\partial c_f^{(2)}}{\partial y} \right]_{y=0}, \quad (\text{A.21})$$

Subtracting (A.21) from (A.20) yields

$$\frac{\epsilon^{-2\alpha}}{D_f} (u_f M - \langle u_f M \rangle) \frac{\partial^2 c_f^{(0)}}{\partial \xi^2} = D_f \frac{\partial^2 c_f^{(2)}}{\partial y^2} + D_f \left[ \frac{\partial c_f^{(2)}}{\partial y} \right]_{y=0}. \quad (\text{A.22})$$

where the boundary term can be rewritten using (A.9). This leads to

$$\frac{\partial^2 c_f^{(2)}}{\partial y^2} = \frac{\epsilon^{-2\alpha}}{D_f^2} (u_f M - \langle u_f M \rangle) \frac{\partial^2 c_f^{(0)}}{\partial \xi^2} - \frac{\phi D_{my}}{D_f} \left[ \frac{\partial c_m^{(2)}}{\partial y} \right]_{y=0}. \quad (\text{A.23})$$

Integration in  $y$  gives

$$\frac{\partial c_f^{(2)}}{\partial y} = \frac{\epsilon^{-2\alpha}}{D_f^2} \frac{\partial^2 c_f^{(0)}}{\partial \xi^2} \int_0^y (u_f M - \langle u_f M \rangle) dy + \frac{\phi D_{my}}{D_f} \left[ \frac{\partial c_m^{(2)}}{\partial y} \right]_{y=0} (K_1 - y), \quad (\text{A.24})$$

where  $K_1$  is an integration constant. Using the no-flux boundary condition at  $y = 1$  (2.20), while observing that  $\int_0^1 (u_f M - \langle u_f M \rangle) dy = \langle u_f M - \langle u_f M \rangle \rangle = 0$ , yields

$$K_1 = 1. \quad (\text{A.25})$$

Integrating (A.24) in  $y$  once more leads to

$$c_f^{(2)} = \frac{\epsilon^{-2\alpha}}{D_f^2} \frac{\partial^2 c_f^{(0)}}{\partial \xi^2} \iint_0^y (u_f M - \langle u_f M \rangle) d^2 y + \frac{\phi D_{my}}{D_f} \left[ \frac{\partial c_m^{(2)}}{\partial y} \right]_{y=0} (K_2 + y - \frac{1}{2} y^2). \quad (\text{A.26})$$

Since  $\langle c_f^{(2)} \rangle = 0$ , then

$$\int_0^1 (K_2 + y - \frac{1}{2} y^2) dy = 0 \quad \text{or} \quad K_2 = -\frac{1}{3}. \quad (\text{A.27})$$

Finally,

$$c_f^{(2)} = \frac{\epsilon^{-2\alpha}}{D_f^2} \frac{\partial^2 c_f^{(0)}}{\partial \xi^2} \iint_0^y (u_f M - \langle u_f M \rangle) d^2 y + \frac{\phi D_{my}}{D_f} \left[ \frac{\partial c_m^{(2)}}{\partial y} \right]_{y=0} (-\frac{1}{2} y^2 + y - \frac{1}{3}). \quad (\text{A.28})$$

A similar procedure leads to

$$c_m^{(2)} = \frac{\epsilon^{-2\alpha}}{D_{my}^2} \frac{\partial^2 c_m^{(0)}}{\partial \xi^2} \iint_0^y (u_m N - \langle u_m N \rangle) d^2 y + \frac{D_f}{\phi D_{my}} \left[ \frac{\partial c_f^{(2)}}{\partial y} \right]_{y=0} \left( -\frac{1}{2} y^2 - yh + \frac{1}{3} h^2 \right). \quad (\text{A.29})$$

## A.4 Upscaled Equations

Applying the averaging operator to (A.1) and (A.2) while accounting for the third boundary condition (2.20), leads to

$$\begin{aligned} \frac{\partial \langle c_f \rangle}{\partial t} + \epsilon^{-1/2} \langle u_f \rangle \frac{\partial c_f^{(0)}}{\partial \xi} + \langle u_f \frac{\partial c_f^{(1)}}{\partial \xi} \rangle + \epsilon^{-1/2} \langle u_f \frac{\partial c_f^{(2)}}{\partial \xi} \rangle \\ = \epsilon^\alpha D_f \frac{\partial^2 \langle c_f \rangle}{\partial \xi^2} - \epsilon^{\alpha-1/2} D_f \left[ \frac{\partial c_f^{(1)}}{\partial y} \right]_{y=0} - \epsilon^{\alpha-1} D_f \left[ \frac{\partial c_f^{(2)}}{\partial y} \right]_{y=0}, \end{aligned} \quad (\text{A.30})$$

and

$$\begin{aligned} \frac{\partial \langle c_m \rangle}{\partial t} + \epsilon^{-1/2} \langle u_m \rangle \frac{\partial c_m^{(0)}}{\partial \xi} + \langle u_m \frac{\partial c_m^{(1)}}{\partial \xi} \rangle + \epsilon^{1/2} \langle u_m \frac{\partial c_m^{(2)}}{\partial \xi} \rangle \\ = \epsilon^\alpha D_{mx} \frac{\partial^2 \langle c_m \rangle}{\partial \xi^2} - \epsilon^{\alpha-1/2} \frac{D_{my}}{h} \left[ \frac{\partial c_m^{(1)}}{\partial y} \right]_{y=0} - \epsilon^{\alpha-1} \frac{D_{my}}{h} \left[ \frac{\partial c_m^{(2)}}{\partial y} \right]_{y=0}, \end{aligned} \quad (\text{A.31})$$

respectively, since  $\langle c_j^{(1)} \rangle = \langle c_j^{(2)} \rangle = 0$  and  $\langle c_j \rangle = \langle c_j^{(0)} \rangle$  with  $j = \{f, m\}$ . In order to close (A.30) and (A.31), the nonlocal advective terms and the boundary terms ought to be expressed in terms of macroscale quantities. Averaging (A.4c) leads to

$$\langle u_f \frac{\partial c_f^{(2)}}{\partial \xi} \rangle = 0, \quad (\text{A.32})$$

since  $\langle c_f^{(1)} \rangle = 0$ . Inserting (A.14) in (A.30) while accounting for (A.32) gives

$$\begin{aligned} & \frac{\partial \langle c_f \rangle}{\partial t} + \epsilon^{-1/2} \langle u_f \rangle \frac{\partial c_f^{(0)}}{\partial \xi} + \epsilon^{-\alpha} \frac{\langle u_f M \rangle}{D_f} \frac{\partial^2 c_f^{(0)}}{\partial \xi^2} \\ &= \epsilon^\alpha D_f \frac{\partial^2 \langle c_f \rangle}{\partial \xi^2} - \epsilon^{\alpha-1/2} D_f \left[ \frac{\partial c_f^{(1)}}{\partial y} \right]_{y=0} - \epsilon^{\alpha-1} D_f \left[ \frac{\partial c_f^{(2)}}{\partial y} \right]_{y=0}, \end{aligned} \quad (\text{A.33})$$

Similarly, for the matrix we obtain

$$\begin{aligned} & \frac{\partial \langle c_m \rangle}{\partial t} + \epsilon^{-1/2} \langle u_m \rangle \frac{\partial c_m^{(0)}}{\partial \xi} + \epsilon^{-\alpha} \frac{\langle u_m N \rangle}{D_{my}} \frac{\partial^2 c_m^{(0)}}{\partial \xi^2} \\ &= \epsilon^\alpha D_{mx} \frac{\partial^2 \langle c_m \rangle}{\partial \xi^2} - \epsilon^{\alpha-1/2} \frac{D_{my}}{h} \left[ \frac{\partial c_m^{(1)}}{\partial y} \right]_{y=0} - \epsilon^{\alpha-1} \frac{D_{my}}{h} \left[ \frac{\partial c_m^{(2)}}{\partial y} \right]_{y=0}, \end{aligned} \quad (\text{A.34})$$

The last step to close (A.33) and (A.34) is to determine the boundary flux terms

$[\partial_y c_f^{(1)}]_{y=0}$  and  $[\partial_y c_f^{(2)}]_{y=0}$ . Combining the boundary condition (A.8) with (A.16) gives,

$$\frac{\partial c_m^{(1)}}{\partial y} = \epsilon^{-\alpha} \frac{N'}{D_{my}} \frac{\partial c_m^{(0)}}{\partial \xi} \quad (\text{A.35})$$

where  $N' = dN/dy$  and  $[N']_{y=0} = N_1$ , see (A.17). Therefore,

$$\left[ \frac{\partial c_m^{(1)}}{\partial y} \right]_{y=0} = \epsilon^{-\alpha} \frac{N_1}{D_{my}} \frac{\partial \langle c_m \rangle}{\partial \xi}. \quad (\text{A.36})$$

Combining (A.36) with (A.8) gives

$$\left[ \frac{\partial c_f^{(1)}}{\partial y} \right]_{y=0} = \epsilon^{-\alpha} \frac{\phi N_1}{D_f} \frac{\partial \langle c_m \rangle}{\partial \xi}. \quad (\text{A.37})$$

Similarly, for the matrix

$$\left[ \frac{\partial c_m^{(1)}}{\partial y} \right]_{y=0} = \epsilon^{-\alpha} \frac{M_1}{\phi D_{my}} \frac{\partial \langle c_f \rangle}{\partial \xi}. \quad (\text{A.38})$$

From (A.28) we obtain

$$\left[ \frac{\partial c_m^{(2)}}{\partial y} \right]_{y=0} = -\frac{3D_f}{\phi D_{my}} c_f^{(2)}(y=0). \quad (\text{A.39})$$

At the interface  $y = 0$ , continuity of concentration (A.6) imposes

$$\epsilon c_m^{(2)} = c_f^{(0)} - c_m^{(0)} + O(\sqrt{\epsilon}) \quad \text{and} \quad \epsilon c_f^{(2)} = c_m^{(0)} - c_f^{(0)} + O(\sqrt{\epsilon}). \quad (\text{A.40})$$

Hence,

$$\left[ \frac{\partial c_m^{(2)}}{\partial y} \right]_{y=0} = -\frac{3D_f}{\phi \epsilon D_{my}} (c_f^{(0)} - c_m^{(0)}) = -\frac{3D_f}{\phi \epsilon D_{my}} (\langle c_f \rangle - \langle c_m \rangle) \quad (\text{A.41})$$

$$\left[ \frac{\partial c_m^{(2)}}{\partial y} \right]_{y=0} = -\frac{3D_f}{\phi \epsilon D_{my}} (\langle c_f \rangle - \langle c_m \rangle) \quad (\text{A.42})$$

A similar relation can be found for the channel

$$\left[ \frac{\partial c_f^{(2)}}{\partial y} \right]_{y=0} = \frac{3\phi D_{my}}{\epsilon h D_f} (\langle c_f \rangle - \langle c_m \rangle). \quad (\text{A.43})$$

Inserting (A.37), (A.38) (A.41) and (A.43) into (A.33) and (A.34) gives

$$\begin{aligned} \frac{\partial \langle c_f \rangle}{\partial t} + \frac{1}{\sqrt{\epsilon}} \langle u_f \rangle \frac{\partial \langle c_f \rangle}{\partial \xi} + \frac{\epsilon^{-\alpha}}{D_f} \langle u_f M \rangle \frac{\partial^2 \langle c_f \rangle}{\partial \xi^2} \\ = \epsilon^\alpha D_f \frac{\partial^2 \langle c_f \rangle}{\partial \xi^2} - \epsilon^{\alpha-1} \sqrt{\epsilon} \phi \epsilon^{-\alpha} N_1 \frac{\partial \langle c_m \rangle}{\partial \xi} - \epsilon^{\alpha-1} \frac{3\phi D_{my}}{\epsilon h} (\langle c_f \rangle - \langle c_m \rangle), \end{aligned} \quad (\text{A.44})$$

and

$$\begin{aligned} \frac{\partial \langle c_m \rangle}{\partial t} + \frac{1}{\sqrt{\epsilon}} \langle u_m \rangle \frac{\partial \langle c_m \rangle}{\partial \xi} + \frac{\epsilon^{-\alpha}}{D_{my}} \langle u_m N \rangle \frac{\partial^2 \langle c_m \rangle}{\partial \xi^2} \\ = \epsilon^\alpha D_{mx} \frac{\partial^2 \langle c_m \rangle}{\partial \xi^2} + \frac{M_1}{\phi h \sqrt{\epsilon}} \frac{\partial \langle c_f \rangle}{\partial \xi} + \epsilon^{\alpha-1} \frac{D_{my}}{h} \frac{3D_f}{\phi \epsilon D_{my}} (\langle c_f \rangle - \langle c_m \rangle). \end{aligned} \quad (\text{A.45})$$

Rescaling the axis back to the physical coordinate  $x$ , multiplying both sides by  $\epsilon^{1-\alpha}$  and using the Péclet number definition, we obtain the macroscopic equations (3.6a) and (3.6b).

$$\epsilon \text{Pe} \left( \frac{\partial \langle c_f \rangle}{\partial t} + \langle u_f \rangle \frac{\partial \langle c_f \rangle}{\partial x} \right) = \epsilon^2 D_f^* \frac{\partial^2 \langle c_f \rangle}{\partial x^2} - \phi \left[ \epsilon \text{Pe} N_1 \frac{\partial \langle c_m \rangle}{\partial x} + \frac{3D_{my}}{\epsilon h} (\langle c_f \rangle - \langle c_m \rangle) \right], \quad (\text{A.46})$$

where

$$\begin{aligned} \frac{\partial \langle c_f \rangle}{\partial t} + \langle u_f \rangle \frac{\partial \langle c_f \rangle}{\partial x} + \frac{\epsilon^{1-\alpha}}{D_f} \langle u_f M \rangle \frac{\partial^2 \langle c_f \rangle}{\partial x^2} \\ = \epsilon^{1+\alpha} D_f \frac{\partial^2 \langle c_f \rangle}{\partial x^2} - \phi N_1 \frac{\partial \langle c_m \rangle}{\partial x} - \epsilon^{\alpha-1} \frac{3\phi D_{my}}{\epsilon h} (\langle c_f \rangle - \langle c_m \rangle), \end{aligned} \quad (\text{A.47})$$

leads to:

$$\begin{aligned} \frac{\partial \langle c_f \rangle}{\partial t} + \langle u_f \rangle \frac{\partial \langle c_f \rangle}{\partial x} = \epsilon^{1+\alpha} D_f \frac{\partial^2 \langle c_f \rangle}{\partial x^2} \\ - \frac{\epsilon^{1-\alpha}}{D_f} \langle u_f M \rangle \frac{\partial^2 \langle c_f \rangle}{\partial x^2} - \phi N_1 \frac{\partial \langle c_m \rangle}{\partial x} - \epsilon^{\alpha-1} \frac{3\phi D_{my}}{\epsilon h} (\langle c_f \rangle - \langle c_m \rangle), \end{aligned} \quad (\text{A.48})$$

Multiply  $\epsilon^{1-\alpha}$  on both sides:

$$\begin{aligned} \epsilon^{1-\alpha} \frac{\partial \langle c_f \rangle}{\partial t} + \epsilon^{1-\alpha} \langle u_f \rangle \frac{\partial \langle c_f \rangle}{\partial x} = \epsilon^2 D_f \frac{\partial^2 \langle c_f \rangle}{\partial x^2} \\ - \frac{\epsilon^{2-2\alpha}}{D_f} \langle u_f M \rangle \frac{\partial^2 \langle c_f \rangle}{\partial x^2} - \epsilon^{1-\alpha} \phi N_1 \frac{\partial \langle c_m \rangle}{\partial x} - \frac{3\phi D_{my}}{\epsilon h} (\langle c_f \rangle - \langle c_m \rangle), \end{aligned} \quad (\text{A.49})$$

Substitute the definition of Pe:

$$\begin{aligned} \epsilon \text{Pe} \frac{\partial \langle c_f \rangle}{\partial t} + \epsilon \text{Pe} \langle u_f \rangle \frac{\partial \langle c_f \rangle}{\partial x} = \epsilon^2 D_f \frac{\partial^2 \langle c_f \rangle}{\partial x^2} \\ - \text{Pe}^2 \frac{\epsilon^2}{D_f} \langle u_f M \rangle \frac{\partial^2 \langle c_f \rangle}{\partial x^2} - \epsilon \text{Pe} \phi N_1 \frac{\partial \langle c_m \rangle}{\partial x} - \frac{3\phi D_{my}}{\epsilon h} (\langle c_f \rangle - \langle c_m \rangle), \end{aligned} \quad (\text{A.50})$$



$$D_f^* = D_f - \text{Pe}^2 \frac{I_f}{D_f}, \quad (\text{A.51})$$

with

$$I_f = \langle u_f M \rangle = \int_0^1 u_f(y) M(y) dy \quad (\text{A.52})$$

With a similar procedure, we will have the upscaled equation for the matrix:

$$\epsilon \text{Pe} \left( \frac{\partial \langle c_m \rangle}{\partial t} + \langle u_m \rangle \frac{\partial \langle c_m \rangle}{\partial x} \right) = \epsilon^2 D_m^* \frac{\partial^2 \langle c_m \rangle}{\partial x^2} + \frac{1}{\phi} \left[ \epsilon \text{Pe} \frac{M_1}{h} \frac{\partial \langle c_f \rangle}{\partial x} + \frac{3D_f}{\epsilon} (\langle c_f \rangle - \langle c_m \rangle) \right], \quad (\text{A.53})$$

where:

$$D_m^* = D_{mx} - \text{Pe}^2 \frac{I_m}{D_{my}}, \quad (\text{A.54})$$

and:

$$I_m = \frac{1}{h} \int_{-h}^0 u_m(y) N(y) dy, \quad (\text{A.55})$$

$$I_m = \frac{1}{h} (I_{m,0} - I_{m,-h}), \quad (\text{A.56})$$

and

$$I_{m,0} = \frac{E^2}{2\lambda^3} - \frac{2E\Psi}{\lambda^5} - \frac{EN_1^*}{\lambda^2} + \frac{EN_2}{\lambda} - \frac{F^2}{2\lambda^3} - \frac{FN_1^*}{\lambda^2} - \frac{FN_2}{\lambda}, \quad (\text{A.57})$$

$$I_{m,-h} = \frac{E^2}{2\lambda^3} e^{-2\lambda h} - \frac{EFh}{\lambda^2} - \frac{E\Psi}{2\lambda^2} \left( \frac{h^2}{\lambda} + \frac{2h}{\lambda^2} + \frac{2}{\lambda^3} \right) e^{-\lambda h} \quad (\text{A.58})$$

$$\begin{aligned} &+ EN_1^* \left( -\frac{h}{\lambda} - \frac{1}{\lambda^2} \right) e^{-\lambda h} + \frac{EN_2}{\lambda} e^{\lambda h} - \frac{EFh}{\lambda^2} \\ &- \frac{F^2}{2\lambda^3} e^{2\lambda h} - \frac{F\Psi}{2\lambda^2} \left( -\frac{h^2}{\lambda} + \frac{2h}{\lambda^2} - \frac{2}{\lambda^3} \right) e^{\lambda h} \\ &+ FN_1^* \left( \frac{h}{\lambda} - \frac{1}{\lambda^2} \right) e^{\lambda h} - \frac{FN_2}{\lambda} e^{\lambda h} - \frac{E\Psi}{\lambda^5} e^{-\lambda h} + \frac{F\Psi}{\lambda^5} e^{\lambda h} \\ &- \frac{\Psi^2}{6\lambda^4} h^3 - \frac{\Psi N_1^*}{2\lambda^2} h^2 + \frac{\Psi N_2}{\lambda^2} h, \end{aligned}$$

$$N_1^* = N_1 - \left( \frac{E}{\lambda} - \frac{F}{\lambda} \right), \quad (\text{A.59})$$

$$(\text{A.60})$$

# Appendix B

## Thin Fracture Solution

### B.1 Tang *et al.*'s solution

Several analytical solutions have been developed since the 1980s. In this project, we present one developed by *Tang and et al.* [1981]. Tang's solution assumed a semi-infinite pore matrix and a single fracture embeds inside.

#### B.1.1 Equations and Boundary Conditions

Equation for the fracture, No radioactive reaction/decaying, No absorption on solid wall, use  $\frac{q}{2}$  as the correction for one-sided pore matrix:

$$\frac{\partial c_f}{\partial t} + U \frac{\partial c_f}{\partial z} - D_f \frac{\partial^2 c_f}{\partial z^2} + \frac{q}{2b} = 0 \quad (\text{B.1})$$

$c_f$  is concentration inside the fracture.  $U$  is the inlet velocity.  $D_f$  is the effective diffusion coefficient in the fracture.  $q$  is the flux. Equation for the pore-matrix:

$$\frac{\partial c_m}{\partial t} - D_m \frac{\partial^2 c_m}{\partial x^2} = 0 \quad (\text{B.2})$$

$c_m$  is concentration inside the fracture. Additionally:

$$D_f = U\alpha_L + D^* \quad (\text{B.3})$$

$$D_m = \tau D^* \quad (\text{B.4})$$

$$q = -\theta D_m \left[ \frac{\partial c_m}{\partial x} \right]_{x=b} \quad (\text{B.5})$$

$$(\text{B.6})$$

$\alpha_L$  is dispersivity.  $D^*$  is molecular diffusion coefficient.  $\theta$  is porosity.  $\tau$  is tortuosity.

Boundary conditions are:

$$c_f(0, t) = C_0 \quad (\text{B.7})$$

$$c_f(\infty, t) = 0 \quad (\text{B.8})$$

$$c_f(z, 0) = 0 \quad (\text{B.9})$$

$$c_m(b, z, t) = c(z, t) \quad (\text{B.10})$$

$$c_m(\infty, z, t) = 0 \quad (\text{B.11})$$

$$c_m(x, z, 0) = 0 \quad (\text{B.12})$$

## B.1.2 Dimensionless Form

Define scales:

$$C_0 : \text{Concentration} \quad (\text{B.13})$$

$$L : \text{Length} \quad (\text{B.14})$$

$$T : \text{Time} \quad (\text{B.15})$$

Pull out the order of magnitude for each term, inside the fracture:

$$\frac{C_0}{T} \frac{\partial \tilde{c}_f}{\partial \tilde{t}} + \frac{UC_0}{L} \frac{\partial \tilde{c}_f}{\partial \tilde{z}} - \frac{D_f C_0}{L^2} \frac{\partial^2 \tilde{c}_f}{\partial \tilde{z}^2} - \frac{\theta D_m C_0}{2bL} \left[ \frac{\partial \tilde{c}_m}{\partial \tilde{x}} \right]_{\tilde{x}=b/L} = 0 \quad (\text{B.16})$$

the last term on left hand side will be substituted later. For matrix:

$$\frac{C_0}{T} \frac{\partial \tilde{c}_m}{\partial \tilde{t}} - \frac{D_m C_0}{L^2} \frac{\partial^2 \tilde{c}_m}{\partial \tilde{x}^2} = 0 \quad (\text{B.17})$$

and dimensionless boundary conditions are:

$$\tilde{c}_f(0, \tilde{t}) = 1 \quad (\text{B.18})$$

$$\tilde{c}_f(\infty, \tilde{t}) = 0 \quad (\text{B.19})$$

$$\tilde{c}_f(\tilde{z}, 0) = 0 \quad (\text{B.20})$$

$$\tilde{c}_m(b/L, \tilde{z}, \tilde{t}) = \tilde{c}(\tilde{z}, \tilde{t}) \quad (\text{B.21})$$

$$\tilde{c}_m(\infty, \tilde{z}, \tilde{t}) = 0 \quad (\text{B.22})$$

$$\tilde{c}_m(\tilde{x}, \tilde{z}, 0) = 0 \quad (\text{B.23})$$

After erasing the tilde, and using simplified notation we will have the equations need to be solved (coupled with the boundary conditions above):

$$\frac{C_0}{T} \partial_t c_f + \frac{UC_0}{L} \partial_z c_f - \frac{D_f C_0}{L^2} \partial_{zz} c_f - \frac{\theta D_m C_0}{2bL} \left[ \frac{\partial c_m}{\partial x} \right]_{x=b/L} = 0 \quad (\text{B.24})$$

$$\frac{C_0}{T} \partial_t c_m - \frac{D_m C_0}{L^2} \partial_{xx} c_m = 0 \quad (\text{B.25})$$

### B.1.3 Solve the concentration for matrix

Start from equation (B.25), rearrange:

$$\frac{L^2}{\tau D^* T} \partial_t c_m - \partial_{xx} c_m = 0 \quad (\text{B.26})$$

Laplace transformation:

$$\mathcal{L} [\partial_t c_m] = \int_0^\infty e^{-st} c_m(x, z, t) dt$$

denote:

$$\mathcal{L} [f] = \bar{f}$$

we will have:

$$\mathcal{L} [\partial_t c_m] = s\bar{c}_m - c_m(x, z, 0)$$

use boundary condition:

$$\mathcal{L} [\partial_t c_m] = s\bar{c}_m$$

and Laplace transform doesn't affect spacial derivatives, we will have:

$$\frac{L^2}{\tau D^* T} s \bar{c}_m - \partial_{xx} \bar{c}_m = 0 \quad (\text{B.27})$$

by using the associated polynomial:

$$\lambda^2 - \frac{L^2}{\tau D^* T} s = 0$$

$$\lambda = \pm \sqrt{\frac{L^2}{\tau D^* T} s}$$

therefore, the physical solution will be:

$$\bar{c}_m = C_1 \exp \left[ -\sqrt{\frac{L^2}{\tau D^* T} s} \cdot \left(x - \frac{b}{L}\right) \right]$$

use the boundary condition, we can have:

$$\bar{c}_m = \bar{c}_f \exp \left[ -\sqrt{\frac{L^2}{\tau D^* T} s} \cdot \left(x - \frac{b}{L}\right) \right]$$

where  $\bar{c}_f$  is the Laplace transformation of  $c_f$ .

$$\left[ \frac{\partial c_m}{\partial x} \right]_{x=b/L} = -\sqrt{\frac{L^2}{\tau D^* T} s} \cdot \bar{c}_f \quad (\text{B.28})$$

#### B.1.4 solve concentration in fracture

use equation (B.24) rearrange:

$$\frac{L^2}{TD_f} \partial_t c_f + \frac{UL}{D_f} \partial_z c_f - \partial_{zz} c_f - \frac{\theta D_m L}{2bD_f} \left[ \frac{\partial c_m}{\partial x} \right]_{x=b/L} = 0$$

Laplace transform:

$$\frac{L^2}{TD_f} s \bar{c}_f + \frac{UL}{D_f} \partial_z \bar{c}_f - \partial_{zz} \bar{c}_f - \frac{\theta D_m L}{2bD_f} \left[ \frac{\partial \bar{c}_m}{\partial x} \right]_{x=b/L} = 0$$

use equation (B.28):

$$\frac{L^2 s}{TD_f} \bar{c}_f + \frac{UL}{D_f} \partial_z \bar{c}_f - \partial_{zz} \bar{c}_f + \frac{\theta D_m L}{2bD_f} \sqrt{\frac{L^2 s}{D_m T}} \cdot \bar{c}_f = 0$$

rearrange:

$$\partial_{zz} \bar{c}_f - \frac{UL}{D_f} \partial_z \bar{c}_f - \left[ \frac{\theta L^2}{2bD_f} \sqrt{\frac{D_m s}{T}} + \frac{L^2 s}{TD_f} \right] \cdot \bar{c}_f = 0$$

associated polynomial:

$$\lambda^2 - \frac{UL}{D_f} \lambda - \left[ \frac{\theta L^2}{2bD_f} \sqrt{\frac{D_m s}{T}} + \frac{L^2 s}{TD_f} \right] = 0$$

simply:

$$\lambda_{1,2} = \frac{\frac{UL}{D_f} \pm \sqrt{\left(\frac{UL}{D_f}\right)^2 + 4 \left[ \frac{\theta L^2}{2bD_f} \sqrt{\frac{D_m s}{T}} + \frac{L^2 s}{TD_f} \right]}}{2}$$

solution will be like:

$$\bar{c}_f = C_2 e^{\lambda_1 z} + C_3 e^{\lambda_2 z}$$

physical solution cannot go to infinity, the positive root is dropped:

$$\bar{c}_f = C_3 e^{\lambda_2 z}$$

which is:

$$\bar{c}_f = C_3 \exp \left\{ \left[ \frac{UL}{2D_f} - \sqrt{\left(\frac{UL}{2D_f}\right)^2 + \frac{\theta L^2}{2bD_f} \sqrt{\frac{D_m s}{T}} + \frac{L^2 s}{TD_f}} \right] \cdot z \right\}$$

to get the constant of integration, we perform Laplace transform on boundary condition, note that:

$$\mathcal{L}[1] = \frac{1}{s}$$



therefore:

$$\bar{c}_f(0, s) = \frac{1}{s}$$

substitute into the solution, we will have:

$$\bar{c}_f = \frac{1}{s} \exp \left\{ \left[ \frac{UL}{2D_f} - \sqrt{\left(\frac{UL}{2D_f}\right)^2 + \frac{\theta L^2}{2bD_f} \sqrt{\frac{D_m s}{T}} + \frac{L^2 s}{TD_f}} \right] \cdot z \right\}$$

which is:

$$\begin{aligned} \bar{c}_f &= \frac{1}{s} \exp \left[ \frac{UL}{2D_f} \cdot z \right] \exp \left[ -\sqrt{\left(\frac{UL}{2D_f}\right)^2 \left(1 + \frac{2\theta D_f}{bU^2} \sqrt{\frac{D_m s}{T}} + \frac{4D_f s}{TU^2}\right)} \cdot z \right] \\ \bar{c}_f &= \frac{1}{s} \exp \left[ \frac{UL}{2D_f} \cdot z \right] \exp \left[ -\left(\frac{UL}{2D_f}\right) \sqrt{\left(1 + \frac{2\theta D_f}{bU^2} \sqrt{\frac{D_m s}{T}} + \frac{4D_f s}{TU^2}\right)} \cdot z \right] \\ \bar{c}_f &= \frac{1}{s} \exp \left[ \frac{UL}{2D_f} \cdot z \right] \exp \left[ -\left(\frac{UL}{2D_f}\right) \sqrt{\left[1 + \frac{4D_f}{TU^2} \left(\frac{\sqrt{s}}{\frac{2b}{\theta\sqrt{D_m T}}} + s\right)\right]} \cdot z \right] \end{aligned} \quad (B.29)$$

at this point, the only thing left for us is to inverse Laplace transform this expression back to time domain. This form is same as the dimensional form on the paper without any substitution for the groups of parameters. Before proceeding, we may define some parameters as following:

$$v = \frac{UL}{2D_f} \quad (B.30)$$

$$\beta^2 = \frac{4D_f}{TU^2} \quad (B.31)$$

$$A = \frac{2b}{\theta\sqrt{D_m T}} \quad (B.32)$$

then:

$$\bar{c}_f = \frac{1}{s} \exp(vz) \exp \left[ -vz \left\{ 1 + \beta^2 \left( \frac{\sqrt{s}}{A} + s \right) \right\}^{0.5} \right] \quad (B.33)$$

### B.1.5 Inverse Laplace transform

Let's perform the inverse Laplace transform still with equation (B.33), note there is a square root inside the exponential function we can get rid of it with:

$$\frac{\sqrt{\pi}}{2} \exp(-2\chi) = \int_0^{\infty} \exp\left(-\xi^2 - \frac{\chi^2}{\xi^2}\right) d\xi$$

let:

$$-2\chi = -vz \left\{ 1 + \beta^2 \left( \frac{\sqrt{s}}{A} + s \right) \right\}^{0.5}$$

$$\chi = \frac{vz}{2} \left\{ 1 + \beta^2 \left( \frac{\sqrt{s}}{A} + s \right) \right\}^{0.5}$$

then, we have:

$$\exp\left[-vz \left\{ 1 + \beta^2 \left( \frac{\sqrt{s}}{A} + s \right) \right\}^{0.5}\right] = \frac{2}{\sqrt{\pi}} \int_0^{\infty} \exp\left(-\xi^2 - \frac{\left[ \frac{vz}{2} \left\{ 1 + \beta^2 \left( \frac{\sqrt{s}}{A} + s \right) \right\}^{0.5} \right]^2}{\xi^2}\right) d\xi$$

$$\frac{2}{\sqrt{\pi}} \int_0^{\infty} \exp\left(-\xi^2 - \frac{v^2 z^2 \left[ 1 + \beta^2 \left( \frac{\sqrt{s}}{A} + s \right) \right]}{4\xi^2}\right) d\xi$$

the solution becomes:

$$\bar{c}_f = \frac{2}{\sqrt{\pi}} \frac{1}{s} \exp(vz) \int_0^{\infty} \exp\left(-\xi^2 - \frac{v^2 z^2 \left[ 1 + \beta^2 \left( \frac{\sqrt{s}}{A} + s \right) \right]}{4\xi^2}\right) d\xi \quad (\text{B.34})$$

$$\bar{c}_f = \frac{2}{\sqrt{\pi}} \frac{1}{s} \exp(vz) \int_0^{\infty} \exp(-\xi^2) \exp\left(-\frac{v^2 z^2}{4\xi^2}\right) \exp\left[-\frac{v^2 z^2}{4\xi^2} \beta^2 \left( \frac{\sqrt{s}}{A} + s \right)\right] d\xi$$

apply inverse Laplace operator:

$$c_f(z, t) = \frac{2}{\sqrt{\pi}} \exp(vz) \int_0^{\infty} \exp(-\xi^2) \exp\left(-\frac{v^2 z^2}{4\xi^2}\right) \mathcal{L}^{-1}\left\{\frac{1}{s} \exp\left[-\frac{v^2 z^2}{4\xi^2} \beta^2 \left( \frac{\sqrt{s}}{A} + s \right)\right]\right\} d\xi$$

Also we can see:

$$\mathcal{L}^{-1}\{exp[(-s \cdot C) \cdot F(s)]\} = \mathcal{L}^{-1}[F(t - C)] \cdot U(t - C)$$

with Heaviside step function  $U(t - C)$ . So:

$$c_f(z, t) = \frac{2}{\sqrt{\pi}} exp(vz) \int_0^{\infty} exp(-\xi^2) exp\left(-\frac{v^2 z^2}{4\xi^2}\right) \mathcal{L}^{-1}\left\{\frac{1}{s} exp\left[-\frac{v^2 z^2 \beta^2 \sqrt{s}}{4\xi^2 A} - \frac{v^2 z^2 \beta^2}{4\xi^2} s\right]\right\} d\xi$$

$$c_f(z, t) = \frac{2}{\sqrt{\pi}} exp(vz) \int_0^{\infty} exp(-\xi^2) exp\left(-\frac{v^2 z^2}{4\xi^2}\right) \mathcal{L}^{-1}\left\{\frac{exp\left[-\frac{v^2 z^2 \beta^2 \sqrt{s}}{4\xi^2 A}\right]}{s} exp\left[-\frac{v^2 z^2 \beta^2}{4\xi^2} s\right]\right\} d\xi$$

The last piece of information is from a magical book: *p.245, Tables of Integral Transforms Vol.I, by Harry Bateman, 1954 McGraw-Hill Book*. Gives:

$$\mathcal{L}^{-1}\left[\frac{exp(-\sqrt{a}\sqrt{s})}{s}\right] = erfc\left(\frac{1}{2}\frac{\sqrt{a}}{\sqrt{t}}\right)$$

Now we can have the final answer:

$$c_f(z, t) = \frac{2exp(vz)}{\sqrt{\pi}} \int_0^{\infty} exp\left(-\xi^2 - \frac{v^2 z^2}{4\xi^2}\right) erfc\left(\frac{\frac{v^2 z^2 \beta^2}{4\xi^2 A}}{2\sqrt{t - \frac{v^2 z^2 \beta^2}{4\xi^2}}}\right) U\left(t - \frac{v^2 z^2 \beta^2}{4\xi^2}\right) d\xi$$

For the lower limit:

$$t > \frac{v^2 z^2 \beta^2}{4\xi^2} \Rightarrow \xi > \sqrt{\frac{v^2 z^2 \beta^2}{4t}}$$

$$c_f(z, t) = \frac{2}{\sqrt{\pi}} exp(vz) \int_l^{\infty} exp(-\xi^2 - K) erfc\left(\frac{K\beta^2}{2A\sqrt{t - K\beta^2}}\right) d\xi \quad (\text{B.35})$$

with:

$$l = \sqrt{\frac{v^2 z^2 \beta^2}{4t}}, K = \frac{v^2 z^2}{4\xi^2}$$

The most complete form (without no defined variables) with  $D_m = \tau D^*$  and  $D_f = \alpha_L U + D^*$ :

$$c_f(z, t) = \frac{2}{\sqrt{\pi}} \exp\left(\frac{UL}{2D_f} z\right) \int_l^\infty \exp\left(-\xi^2 - \frac{U^2 L^2 z^2}{16D_f^2 \xi^2}\right) \operatorname{erfc}\left(\frac{\frac{L^2 z^2 \theta}{2bTU\xi^2} \sqrt{\frac{D_m}{D_f}}}{\sqrt{t - \frac{L^2 z^2}{4TD_f \xi^2}}}\right) d\xi \quad (\text{B.36})$$

# Appendix C

## Derivation of the upscaled equations using flux model

### C.1 Velocity

#### C.1.1 fracture

Assumptions:

- 2D Stoke's flow;
- Velocity component ( $u_f$ ) is fully developed in x;
- pressure variation in y-direction is small:  $P_f \sim f(x)$ .

Start from the equation of Stokes' Flow for x-direction:

$$\frac{\partial P_f}{\partial x} = \mu \left( \frac{\partial^2 u_f}{\partial x^2} + \frac{\partial^2 u_f}{\partial y^2} \right)$$

based on the assumptions listed, we can have the equation for velocity in the fracture:

$$\frac{dP_f}{dx} = \mu \frac{d^2 u_f}{dy^2} \quad (\text{C.1})$$

Dimensionless form:

$$\frac{dP_f}{dx} = \frac{\mu U}{b^2} \frac{d^2 \tilde{u}_f}{d\tilde{y}^2} \quad (\text{C.2})$$

Neglect the tilde and let:

$$\boxed{\Psi_f = \frac{b^2}{\mu U} \frac{dP_f}{dx}} \quad (\text{C.3})$$

$$\Psi_f = \frac{d^2 u_f}{dy^2} \quad (\text{C.4})$$

Notice (C.4) is separable, therefore, the general solution can be written as:

$$\boxed{u_f(y) = \frac{\Psi_f}{2} y^2 + Ay + B, \quad y \in [0, 1]} \quad (\text{C.5})$$

### C.1.2 matrix

Assumptions:

- Darcy-Brinkman;
- Velocity component ( $u_m$ ) is fully developed in x;
- pressure variation in y-direction is small:  $P_m \sim f(x)$ .

Darcy-Brinkman equation for x-direction(1949,H.C.Brinkman):

$$\frac{\partial P_m}{\partial x} = -\frac{\mu_e}{k} u_m + \mu \left( \frac{\partial^2 u_m}{\partial x^2} + \frac{\partial^2 u_m}{\partial y^2} \right) \quad (\text{C.6})$$

where,  $k$  is the permeability. Apply the assumptions the dimensionless form can be written as:

$$\frac{dP_m}{dx} = -\frac{\mu_e U}{k} u_m + \frac{\mu_e U}{b^2} \frac{d^2 u_m}{dy^2} \quad (\text{C.7})$$

$$\frac{d^2 u_m}{dy^2} - \frac{b^2}{k} u_m = \frac{b^2}{\mu_e U} \frac{dP_m}{dx} \quad (\text{C.8})$$

Let:

$$\beta = \sqrt{\frac{b^2}{k}}, \quad \Psi_m = \frac{b^2}{\mu_e U} \frac{dP_m}{dx} \quad (\text{C.9})$$

then:

$$\frac{d^2 u_m}{dy^2} - \beta^2 u_m = \Psi_m \quad (\text{C.10})$$

This is a 2-order, constant coefficient, inhomogeneous ODE. We can write the solution as the sum of general solution for the homogeneous problem and the particular solution. Simply:

$$u_m = Ee^{\beta y} + Fe^{-\beta y} - \frac{\Psi_m}{\beta^2}, \quad y \in [-h, 0] \quad (\text{C.11})$$

where  $h = H/b$ ,  $H$  is the depth of the matrix.

### C.1.3 Symmetric top wall, pinned bottom wall

In consideration of symmetric profile, we can apply the boundary condition:

- Top wall:

$$\left. \frac{du_f}{dy} \right|_{y=1} = 0 \quad (\text{C.12})$$

$$\Rightarrow \Psi_f + A = 0 \quad (\text{C.13})$$

- Interface, 0<sup>th</sup> order continuity (continue in velocity):

$$u_f(0^+) = u_m(0^-) \quad (\text{C.14})$$

$$\Rightarrow B = E + F - \frac{\Psi_m}{\beta^2} \quad (\text{C.15})$$

- Interface, 1<sup>st</sup> order continuity (continue in shear stress):

$$\frac{du_f}{dy} \Big|_{y=0^+} = \frac{du_m}{dy} \Big|_{y=0^-} \quad (\text{C.16})$$

$$\Rightarrow A = E\beta - F\beta \quad (\text{C.17})$$

- Bottom wall, no slip:

$$u_m(-h) = 0 \quad (\text{C.18})$$

$$\Rightarrow Ee^{-h\beta} + Fe^{h\beta} - \frac{\Psi_m}{\beta^2} \quad (\text{C.19})$$

solved:

$$A = -\Psi_f \quad (\text{C.20})$$

$$B = 2 \frac{\frac{\Psi_m}{\beta^2} + \frac{\Psi_f}{\beta}}{1 + e^{2\beta h}} - \frac{\Psi_f}{\beta} - \frac{\Psi_m}{\beta^2} \quad (\text{C.21})$$

$$E = \frac{\frac{\Psi_m}{\beta^2} + \frac{\Psi_f}{\beta}}{1 + e^{2\beta h}} - \frac{\Psi_f}{\beta} \quad (\text{C.22})$$

$$F = \frac{\frac{\Psi_m}{\beta^2} + \frac{\Psi_f}{\beta}}{1 + e^{2\beta h}} \quad (\text{C.23})$$



## C.2 Solute Transport

### C.2.1 fracture

Advection-Diffusion Equation:

$$\frac{\partial C_f}{\partial t} + u_f \frac{\partial C_f}{\partial x} = D_f \left( \frac{\partial^2 C_f}{\partial x^2} + \frac{\partial^2 C_f}{\partial y^2} \right) \quad (\text{C.24})$$

We can extract the order of magnitude of each term. In the following equation, all the variables are dimensionless but for simplicity, we keep the notations the same:

$$\frac{C}{T} \frac{\partial C_f}{\partial t} + \frac{UC}{L} u_f \frac{\partial C_f}{\partial x} = \frac{D_f C}{L^2} \frac{\partial^2 C_f}{\partial x^2} + \frac{D_f C}{b^2} \frac{\partial^2 C_f}{\partial y^2} \quad (\text{C.25})$$

Namely:

$$\frac{b^2}{D_f T} \frac{\partial C_f}{\partial t} + \frac{Ub^2}{D_f L} u_f \frac{\partial C_f}{\partial x} = \frac{b^2}{L^2} \frac{\partial^2 C_f}{\partial x^2} + \frac{\partial^2 C_f}{\partial y^2} \quad (\text{C.26})$$

Let:  $\epsilon = \frac{b}{L}$ ,  $Pe_f = \frac{Ub}{D_f}$  we will have:

$$\frac{b^2}{D_f T} \frac{\partial C_f}{\partial t} + \epsilon Pe_f u_f \frac{\partial C_f}{\partial x} = \epsilon^2 \frac{\partial^2 C_f}{\partial x^2} + \frac{\partial^2 C_f}{\partial y^2} \quad (\text{C.27})$$

For the time scale, we have 2 choices. 1) select the diffusion time scale  $T_{dif,y} = \frac{b^2}{D_f}$  or  $T_{dif,x} = \frac{L^2}{D_f}$ ; 2) select the advection time scale  $T = T_{adv} = \frac{L}{U}$ , then:

$$\epsilon Pe_f \frac{\partial C_f}{\partial t} + \epsilon Pe_f u_f \frac{\partial C_f}{\partial x} = \epsilon^2 \frac{\partial^2 C_f}{\partial x^2} + \frac{\partial^2 C_f}{\partial y^2} \quad (\text{C.28})$$

We study the regime where the longitudinal diffusion is negligible compared with the advection and the transversal diffusion. Therefore we select the advection time scale.

We rescale the  $x$ -direction by:

$$x = \epsilon^{0.5} \xi \quad (\text{C.29})$$

Here,  $\delta$  is some real value. Therefore:

$$\frac{\partial}{\partial x} = \frac{\partial}{\partial \xi} \frac{\partial \xi}{\partial x} = \epsilon^{-0.5} \frac{\partial}{\partial \xi} \quad (\text{C.30})$$

$$\frac{\partial^2}{\partial x^2} = \frac{\partial}{\partial \xi} \frac{\partial \xi}{\partial x} \left( \epsilon^{-0.5} \frac{\partial}{\partial \xi} \right) = \epsilon^{-1} \frac{\partial^2}{\partial \xi^2} \quad (\text{C.31})$$

Expand  $C_f$ :

$$C_f(\xi, y, t) = C_f^{(0)}(\xi, t) + \epsilon^{0.5} C_f^{(1)}(\xi, y, t) + \epsilon C_f^{(2)}(\xi, y, t) + \dots \quad (\text{C.32})$$

Substitution will give us:

$$\epsilon Pe_f \frac{\partial C_f}{\partial t} = \epsilon Pe_f \frac{\partial C_f^{(0)}}{\partial t} + \epsilon^{1.5} Pe_f \frac{\partial C_f^{(1)}}{\partial t} + \sum_{n=2}^{\infty} Pe_f \epsilon^{0.5n+1} \frac{\partial C_f^{(n)}}{\partial t} \quad (\text{C.33})$$

$$\epsilon Pe_f u_f \frac{\partial C_f}{\partial x} = \sqrt{\epsilon} Pe_f u_f \frac{\partial C_f^{(0)}}{\partial \xi} + \epsilon Pe_f u_f \frac{\partial C_f^{(1)}}{\partial \xi} + \epsilon^{1.5} Pe_f u_f \frac{\partial C_f^{(2)}}{\partial \xi} \quad (\text{C.34})$$

$$\begin{aligned} & + \sum_{n=3}^{\infty} \epsilon^{0.5+0.5n} Pe_f u_f \frac{\partial C_f^{(n)}}{\partial \xi} \\ \epsilon^2 \frac{\partial^2 C_f}{\partial x^2} &= \epsilon \frac{\partial^2 C_f^{(0)}}{\partial \xi^2} + \epsilon^{1.5} \frac{\partial^2 C_f^{(1)}}{\partial \xi^2} + \sum_{n=2}^{\infty} \epsilon^{1+0.5n} \frac{\partial^2 C_f^{(n)}}{\partial \xi^2} \end{aligned} \quad (\text{C.35})$$

$$\frac{\partial^2 C_f}{\partial y^2} = 0 + \sqrt{\epsilon} \frac{\partial^2 C_f^{(1)}}{\partial y^2} + \epsilon \frac{\partial^2 C_f^{(2)}}{\partial y^2} \quad (\text{C.36})$$

$$+ \sum_{n=3}^{\infty} \epsilon^{0.5n} \frac{\partial^2 C_f^{(n)}}{\partial y^2}$$

Solve it up to the order of  $\epsilon^{1.5}$  and unknowns are:  $C_f^{(0)}(\xi, t)$ ,  $C_f^{(1)}(\xi, y, t)$ ,  $C_f^{(2)}(\xi, y, t)$ .

For  $O(\sqrt{\epsilon})$ :

$$\boxed{Pe_f u_f \frac{\partial C_f^{(0)}}{\partial \xi} = \frac{\partial^2 C_f^{(1)}}{\partial y^2}} \quad (\text{C.37})$$

For  $O(\epsilon)$ :

$$\boxed{Pe_f \frac{\partial C_f^{(0)}}{\partial t} + Pe_f u_f \frac{\partial C_f^{(1)}}{\partial \xi} = \frac{\partial^2 C_f^{(0)}}{\partial \xi^2} + \frac{\partial^2 C_f^{(2)}}{\partial y^2}} \quad (C.38)$$

For  $O(\epsilon^{1.5})$ :

$$\boxed{Pe_f \frac{\partial C_f^{(1)}}{\partial t} + Pe_f u_f \frac{\partial C_f^{(2)}}{\partial \xi} = \frac{\partial^2 C_f^{(1)}}{\partial \xi^2}} \quad (C.39)$$

## C.2.2 Matrix

Advection-Diffusion Equation:

$$\frac{\partial C_m}{\partial t} + u_m \frac{\partial C_m}{\partial x} = D_m \left( \frac{\partial^2 C_m}{\partial x^2} + \frac{\partial^2 C_m}{\partial y^2} \right) \quad (C.40)$$

Apply dimensional analysis similar as did for the fracture:

$$\frac{C}{T} \frac{\partial C_m}{\partial t} + \frac{UC}{L} u_m \frac{\partial C_m}{\partial x} = \frac{D_m C}{L^2} \frac{\partial^2 C_m}{\partial x^2} + \frac{D_m C}{b^2} \frac{\partial^2 C_m}{\partial y^2} \quad (C.41)$$

here we keep  $b$  as the vertical length scale. This gives:

$$\frac{b^2}{D_m T} \frac{\partial C_m}{\partial t} + \frac{Ub^2}{D_m L} u_m \frac{\partial C_m}{\partial x} = \frac{b^2}{L^2} \frac{\partial^2 C_m}{\partial x^2} + \frac{\partial^2 C_m}{\partial y^2} \quad (C.42)$$

Still use:  $\epsilon = \frac{b}{L}$ ,  $Pe_m = \frac{Ub}{D_m}$  and  $T = T_{adv} = \frac{L}{U}$  we will have:

$$\epsilon Pe_m \frac{\partial C_m}{\partial t} + \epsilon Pe_m u_m \frac{\partial C_m}{\partial x} = \epsilon^2 \frac{\partial^2 C_m}{\partial x^2} + \frac{\partial^2 C_m}{\partial y^2} \quad (C.43)$$

Rescale the axis:

$$x = \epsilon^{0.5} \xi \quad (C.44)$$

Expand  $C_m$ :

$$C_m(\xi, y, t) = C_m^{(0)}(\xi, t) + \epsilon^{0.5} C_m^{(1)}(\xi, y, t) + \epsilon C_m^{(2)}(\xi, y, t) + \dots \quad (\text{C.45})$$

Similarly: For  $O(\epsilon^{0.5})$ :

$$\boxed{Pe_m u_m \frac{\partial C_m^{(0)}}{\partial \xi} = \frac{\partial^2 C_m^{(1)}}{\partial y^2}} \quad (\text{C.46})$$

For  $O(\epsilon)$ :

$$\boxed{Pe_m \frac{\partial C_m^{(0)}}{\partial t} + Pe_m u_m \frac{\partial C_m^{(1)}}{\partial \xi} = \frac{\partial^2 C_m^{(0)}}{\partial \xi^2} + \frac{\partial^2 C_m^{(2)}}{\partial y^2}} \quad (\text{C.47})$$

For  $O(\epsilon^{1.5})$ :

$$\boxed{Pe_m \frac{\partial C_m^{(1)}}{\partial t} + Pe_m u_m \frac{\partial C_m^{(2)}}{\partial \xi} = \frac{\partial^2 C_m^{(1)}}{\partial \xi^2}} \quad (\text{C.48})$$

### C.2.3 Boundary condition and Interface condition

- Inlet, constant concentration:

$$C_f(0, y, t) = 1 \quad (\text{C.49})$$

- Initially 0 everywhere:

$$C_f(\xi, y, 0) = 0 \quad (\text{C.50})$$

$$C_m(\xi, y, 0) = 0 \quad (\text{C.51})$$

- On symmetric axis, no flux:

$$\left. \frac{\partial C_f}{\partial y} \right|_{y=1} = 0 \quad (\text{C.52})$$

- Bottom wall, no flux:

$$\left. \frac{\partial C_m}{\partial y} \right|_{y=-h} = 0 \quad (\text{C.53})$$

- Continuity of the concentration on the interface:

$$C_f(\xi, 0, t) = C_m(\xi, 0, t) \quad (\text{C.54})$$

gives:

$$C_f^{(0)} + \epsilon^{0.5} C_f^{(1)} + \epsilon C_f^{(2)} = C_m^{(0)} + \epsilon^{0.5} C_m^{(1)} + \epsilon C_m^{(2)} \quad (\text{C.55})$$

- continuity of the flux on the interface:

$$\left[ \frac{D_f C}{b} \frac{\partial C_f}{\partial y} \right]_{y=0} = \left[ \phi \frac{D_m C}{b} \frac{\partial C_m}{\partial y} \right]_{y=0} \quad (\text{C.56})$$

$$\left[ \frac{\partial C_f}{\partial y} \right]_{y=0} = \left[ \phi \frac{D_m}{D_f} \frac{\partial C_m}{\partial y} \right]_{y=0} \quad (\text{C.57})$$

gives:

$$\left[ \frac{\partial}{\partial y} (C_f^{(0)} + \epsilon^{0.5} C_f^{(1)} + \epsilon C_f^{(2)}) \right]_{y=0} = \left[ \phi \frac{D_m}{D_f} \frac{\partial}{\partial y} (C_m^{(0)} + \epsilon^{0.5} C_m^{(1)} - \epsilon C_m^{(2)}) \right]_{y=0} \quad (\text{C.58})$$

finally:

$$\left[ \epsilon^{0.5} \frac{\partial C_f^{(1)}}{\partial y} + \epsilon \frac{\partial C_f^{(2)}}{\partial y} \right]_{y=0} = \left[ \epsilon^{0.5} \phi \frac{D_m}{D_f} \frac{\partial C_m^{(1)}}{\partial y} - \epsilon \phi \frac{D_m}{D_f} \frac{\partial C_m^{(2)}}{\partial y} \right]_{y=0} \quad (\text{C.59})$$

### C.3 General Steps of solving

The equations can be solved in following steps:

1. Integrate Equation (C.37) with respect to  $y$ :

$$\frac{\partial C_f^{(1)}}{\partial y} = Pe_f \left[ \int u_f(y) dy + M_1(\xi, t) \right] \frac{\partial C_f^{(0)}}{\partial \xi} \quad (C.60)$$

2. Integrate again:

$$C_f^{(1)}(\xi, y, t) = Pe_f \left[ \int \int u_f(y) dy dy + M_1(\xi, t)y + M_2(\xi, t) \right] \frac{\partial C_f^{(0)}}{\partial \xi} \quad (C.61)$$

let:  $M(y) = \int \int u_f(y) dy dy$ :

$$C_f^{(1)}(\xi, y, t) = Pe_f [M(y) + M_1(\xi, t)y + M_2(\xi, t)] \frac{\partial C_f^{(0)}}{\partial \xi} \quad (C.62)$$

3. No flux on the symmetric axis ( $y = 1$ ):

$$\left. \frac{\partial C_f^{(1)}}{\partial y} \right|_{y=1} = 0 \quad (C.63)$$

$$[M' + M_1(\xi, t)]_{y=1} = 0 \quad (C.64)$$

we can solve the  $M_1$ :

$$M_1(\xi, t) = -M' \Big|_{y=1} \quad (C.65)$$

Notice it is a constant. We can have:

$$\boxed{C_f^{(1)}(\xi, y, t) = Pe_f \mathbb{M} \frac{\partial C_f^{(0)}}{\partial \xi} + Pe_f M_2(\xi, t) \frac{\partial C_f^{(0)}}{\partial \xi}} \quad (C.66)$$

where:

$$\mathbb{M}(y, t) = M(y) + M_1 y \quad \text{and} \quad M_2(\xi, t) \frac{\partial C_f^{(0)}}{\partial \xi} \sim f(\xi, t) \quad (C.67)$$

4. Take derivative of both sides of equation (C.66) with respect to  $\xi$ :

$$\frac{\partial C_f^{(1)}}{\partial \xi} = Pe_f \mathbb{M} \frac{\partial^2 C_f^{(0)}}{\partial \xi^2} + Pe_f \frac{\partial}{\partial \xi} \left( M_2 \frac{\partial C_f^{(0)}}{\partial \xi} \right) \quad (\text{C.68})$$

5. Take derivative of both sides of equation (C.68) with respect to  $\xi$ :

$$\frac{\partial^2 C_f^{(1)}}{\partial \xi^2} = Pe_f \mathbb{M} \frac{\partial^3 C_f^{(0)}}{\partial \xi^3} + Pe_f \frac{\partial^2}{\partial \xi^2} \left( M_2 \frac{\partial C_f^{(0)}}{\partial \xi} \right) \quad (\text{C.69})$$

6. Take derivative of both sides of equation (C.66) with respect to  $t$ :

$$\frac{\partial C_f^{(1)}}{\partial t} = Pe_f \mathbb{M} \frac{\partial^2 C_f^{(0)}}{\partial \xi \partial t} + Pe_f \frac{\partial}{\partial t} \left( M_2 \frac{\partial C_f^{(0)}}{\partial \xi} \right) \quad (\text{C.70})$$

7. Substitute into (C.39)

$$\begin{aligned} & Pe_f \left[ Pe_f \mathbb{M} \frac{\partial^2 C_f^{(0)}}{\partial \xi \partial t} + Pe_f \frac{\partial}{\partial t} \left( M_2 \frac{\partial C_f^{(0)}}{\partial \xi} \right) \right] + Pe_f u_f \frac{\partial C_f^{(2)}}{\partial \xi} \\ & = Pe_f \mathbb{M} \frac{\partial^3 C_f^{(0)}}{\partial \xi^3} + Pe_f \frac{\partial^2}{\partial \xi^2} \left( M_2 \frac{\partial C_f^{(0)}}{\partial \xi} \right) \end{aligned} \quad (\text{C.71})$$

Cancel  $Pe_f$ :

$$Pe_f \mathbb{M} \frac{\partial^2 C_f^{(0)}}{\partial \xi \partial t} + \frac{\partial}{\partial t} \left( M_2 \frac{\partial C_f^{(0)}}{\partial \xi} \right) + u_f \frac{\partial C_f^{(2)}}{\partial \xi} = \mathbb{M} \frac{\partial^3 C_f^{(0)}}{\partial \xi^3} + \frac{\partial^2}{\partial \xi^2} \left( M_2 \frac{\partial C_f^{(0)}}{\partial \xi} \right) \quad (\text{C.72})$$

8. integrate with respect to  $\xi$  ( $\int_0^\xi d\xi$ ):

$$\begin{aligned} Pe_f \mathbb{M} \frac{\partial C_f^{(0)}}{\partial t} + \int_0^\xi \frac{\partial}{\partial t} \left( M_2 \frac{\partial C_f^{(0)}}{\partial \xi} \right) d\xi + u_f C_f^{(2)} & = \mathbb{M} \frac{\partial^2 C_f^{(0)}}{\partial \xi^2} \\ & + \frac{\partial}{\partial \xi} \left( M_2 \frac{\partial C_f^{(0)}}{\partial \xi} \right) + f^*(y, t) \end{aligned} \quad (\text{C.73})$$

We can have:

$$u_f C_f^{(2)} = \mathbb{M} \frac{\partial^2 C_f^{(0)}}{\partial \xi^2} - Pe_f \mathbb{M} \frac{\partial C_f^{(0)}}{\partial t} + \frac{\partial}{\partial \xi} \left( M_2 \frac{\partial C_f^{(0)}}{\partial \xi} \right) - \int_0^\xi \frac{\partial}{\partial t} \left( M_2 \frac{\partial C_f^{(0)}}{\partial \xi} \right) d\xi + f^*(y, t) \quad (\text{C.74})$$

$$C_f^{(2)} = \frac{\mathbb{M}}{u_f} \frac{\partial^2 C_f^{(0)}}{\partial \xi^2} - Pe_f \frac{\mathbb{M}}{u_f} \frac{\partial C_f^{(0)}}{\partial t} + \frac{1}{u_f} F(\xi, y, t) \quad (\text{C.75})$$

where:

$$F(\xi, y, t) = \frac{\partial}{\partial \xi} \left( M_2 \frac{\partial C_f^{(0)}}{\partial \xi} \right) - \int_0^\xi \frac{\partial}{\partial t} \left( M_2 \frac{\partial C_f^{(0)}}{\partial \xi} \right) d\xi + f^*(y, t) \quad (\text{C.76})$$

9. Take derivative with respect to  $y$ :

$$\frac{\partial C_f^{(2)}}{\partial y} = \left( \frac{\mathbb{M}}{u_f} \right)' \frac{\partial^2 C_f^{(0)}}{\partial \xi^2} - Pe_f \left( \frac{\mathbb{M}}{u_f} \right)' \frac{\partial C_f^{(0)}}{\partial t} + \frac{1}{u_f} \frac{\partial F}{\partial y} + \left( \frac{1}{u_f} \right)' F \quad (\text{C.77})$$

we will have:

$$\left( \frac{\mathbb{M}}{u_f} \right)' = \frac{\mathbb{M}' u_f - \mathbb{M} u_f'}{u_f^2}, \quad \left( \frac{1}{u_f} \right)' = \frac{-\mathbb{M} u_f'}{u_f^2} \quad (\text{C.78})$$

From equation (C.64) and (C.12) we know:

$$\mathbb{M}' \Big|_{y=1} = 0, \quad u_f' \Big|_{y=1} = 0 \quad (\text{C.79})$$

Therefore we can have:

$$\frac{\partial C_f^{(2)}}{\partial y} \Big|_{y=1} = 0 \quad \text{if} \quad \frac{\partial F}{\partial y} \Big|_{y=1} \quad (\text{C.80})$$

which requires:

$$\frac{\partial f^*}{\partial y} \Big|_{y=1} = 0 \quad (\text{C.81})$$



10. In order to solve  $C_f^{(0)}$ , we average the equation (C.38) over the cross-section

(denote:  $\langle \bullet \rangle = \int_0^1 \bullet dy$ ), gives:

$$Pe_f \frac{\partial C_f^{(0)}}{\partial t} + Pe_f \left\langle u_f \frac{\partial C_f^{(1)}}{\partial \xi} \right\rangle = \frac{\partial^2 C_f^{(0)}}{\partial \xi^2} + \left[ \frac{\partial C_f^{(2)}}{\partial y} \right]_{y=0}^{y=1} \quad (C.82)$$

11. on the wall,  $\frac{\partial C_f^{(2)}}{\partial y} \Big|_{y=1} = 0$ :

$$Pe_f \frac{\partial C_f^{(0)}}{\partial t} + Pe_f \left\langle u_f \frac{\partial C_f^{(1)}}{\partial \xi} \right\rangle = \frac{\partial^2 C_f^{(0)}}{\partial \xi^2} - \left[ \frac{\partial C_f^{(2)}}{\partial y} \right]_{y=0} \quad (C.83)$$

12. Substitute the equation (C.68) and (C.77):

$$Pe_f \frac{\partial C_f^{(0)}}{\partial t} + Pe_f \left\langle u_f Pe_f \mathbb{M} \frac{\partial^2 C_f^{(0)}}{\partial \xi^2} \right\rangle + Pe_f \left\langle Pe_f \frac{\partial}{\partial \xi} \left( M_2 \frac{\partial C_f^{(0)}}{\partial \xi} \right) \right\rangle = \quad (C.84)$$

$$\frac{\partial^2 C_f^{(0)}}{\partial \xi^2} - \left[ \left( \frac{\mathbb{M}}{u_f} \right)' \frac{\partial^2 C_f^{(0)}}{\partial \xi^2} - Pe_f \left( \frac{\mathbb{M}}{u_f} \right)' \frac{\partial C_f^{(0)}}{\partial t} \right]_{y=0}$$

$$- \left[ \frac{1}{u_f} \frac{\partial F}{\partial y} + \left( \frac{1}{u_f} \right)' F \right]_{y=0}$$

$$\frac{\partial C_f^{(0)}}{\partial t} + \left\langle u_f Pe_f \mathbb{M} \frac{\partial^2 C_f^{(0)}}{\partial \xi^2} \right\rangle = \frac{1}{Pe_f} \frac{\partial^2 C_f^{(0)}}{\partial \xi^2} \quad (C.85)$$

$$- \frac{1}{Pe_f} \left[ \left( \frac{\mathbb{M}}{u_f} \right)' \frac{\partial^2 C_f^{(0)}}{\partial \xi^2} - Pe_f \left( \frac{\mathbb{M}}{u_f} \right)' \frac{\partial C_f^{(0)}}{\partial t} \right]_{y=0} + Q$$

where:

$$Q(\xi, t) = - \frac{1}{Pe_f} \left[ \frac{1}{u_f} \frac{\partial F}{\partial y} + \left( \frac{1}{u_f} \right)' F \right]_{y=0} - Pe_f \left\langle \frac{\partial}{\partial \xi} \left( M_2 \frac{\partial C_f^{(0)}}{\partial \xi} \right) \right\rangle \quad (C.86)$$

Notice  $\langle f(\xi, t) \rangle = f(\xi, t)$  we will have:

$$\boxed{Q(\xi, t) = - \frac{1}{Pe_f} \left[ \frac{1}{u_f} \frac{\partial F}{\partial y} + \left( \frac{1}{u_f} \right)' F \right]_{y=0} - Pe_f \frac{\partial}{\partial \xi} \left( M_2 \frac{\partial C_f^{(0)}}{\partial \xi} \right)} \quad (C.87)$$

13. Collect terms:

$$\begin{aligned} \frac{\partial C_f^{(0)}}{\partial t} - \left[ \left( \frac{\mathbb{M}}{u_f} \right)' \frac{\partial C_f^{(0)}}{\partial t} \right]_{y=0} &= \frac{1}{Pe_f} \frac{\partial^2 C_f^{(0)}}{\partial \xi^2} - \frac{1}{Pe_f} \left[ \left( \frac{\mathbb{M}}{u_f} \right)' \frac{\partial^2 C_f^{(0)}}{\partial \xi^2} \right]_{y=0} \\ &\quad - Pe_f \langle u_f \mathbb{M} \rangle \frac{\partial^2 C_f^{(0)}}{\partial \xi^2} + Q(\xi, t) \end{aligned} \quad (\text{C.88})$$

which is:

$$\frac{\partial C_f^{(0)}}{\partial t} = \frac{1 - Pe_f^2 \langle u_f \mathbb{M} \rangle - \left( \frac{\mathbb{M}}{u_f} \right)' \Big|_{y=0}}{Pe_f - Pe_f \left( \frac{\mathbb{M}}{u_f} \right)' \Big|_{y=0}} \frac{\partial^2 C_f^{(0)}}{\partial \xi^2} + Q(\xi, t) \quad (\text{C.89})$$

Let:

$$\boxed{\mathbb{D}_f = - \langle u_f \mathbb{M} \rangle} \quad (\text{C.90})$$

and:

$$\boxed{\mathcal{D}_f = - \left( \frac{\mathbb{M}}{u_f} \right)' \Big|_{y=0}} \quad (\text{C.91})$$

we will have the equation for the leading order:

$$\frac{\partial C_f^{(0)}}{\partial t} = \kappa \frac{\partial^2 C_f^{(0)}}{\partial \xi^2} + Q(\xi, t) \quad (\text{C.92})$$

with:

$$\boxed{\kappa = \frac{1}{Pe_f} + Pe_f \frac{\mathbb{D}_f}{1 + \mathcal{D}_f}} \quad (\text{C.93})$$

## C.4 Calculate dispersion coefficient $\kappa$

We need:

$$\mathbb{D}_f = - \langle u_f \mathbb{M} \rangle \quad (\text{C.94})$$

we know:

$$u_f = \frac{\Psi_f}{2}y^2 + Ay + B \quad (\text{C.95})$$

$$\mathbb{M} = \int \int u_f(y) dy dy + M_1(\xi, t)y = \frac{\Psi_f}{24}y^4 + \frac{A}{6}y^3 + \frac{B}{2}y^2 + M_1(\xi)y \quad (\text{C.96})$$

For  $M_1$  (equation C.64):

$$\boxed{M_1 = -\frac{\Psi_f}{6} - \frac{A}{2} - B} \quad (\text{C.97})$$

Therefore:

$$\boxed{\mathbb{M} = \frac{\Psi_f}{24}y^4 + \frac{A}{6}y^3 + \frac{B}{2}y^2 + \left(-\frac{\Psi_f}{6} - \frac{A}{2} - B\right)y} \quad (\text{C.98})$$

then:

$$-\mathbb{D}_f = \int_0^1 \left( \frac{\Psi_f}{2}y^2 + Ay + B \right) \left[ \frac{\Psi_f}{24}y^4 + \frac{A}{6}y^3 + \frac{B}{2}y^2 + M_1y \right] dy \quad (\text{C.99})$$

open the first bracket:

$$\begin{aligned} -\mathbb{D}_f = & \int_0^1 \frac{\Psi_f}{2}y^2 \left[ \frac{\Psi_f}{24}y^4 + \frac{A}{6}y^3 + \frac{B}{2}y^2 + M_1y \right] \\ & + Ay \left[ \frac{\Psi_f}{24}y^4 + \frac{A}{6}y^3 + \frac{B}{2}y^2 + M_1y \right] \\ & + B \left[ \frac{\Psi_f}{24}y^4 + \frac{A}{6}y^3 + \frac{B}{2}y^2 + M_1y \right] dy \end{aligned} \quad (\text{C.100})$$

multiply all the terms:

$$\begin{aligned} -\mathbb{D}_f = & \int_0^1 \frac{1}{48}\Psi_f^2y^6 + \frac{1}{12}A\Psi_fy^5 + \frac{1}{4}B\Psi_fy^4 + \frac{1}{2}M_1\Psi_fy^3 \\ & + \frac{1}{24}A\Psi_fy^5 + \frac{1}{6}A^2y^4 + \frac{1}{2}ABy^3 + AM_1y^2 \\ & + \frac{1}{24}B\Psi_fy^4 + \frac{1}{6}ABy^3 + \frac{1}{2}B^2y^2 + BM_1y \quad dy \end{aligned} \quad (\text{C.101})$$

collect terms with the same order:

$$\begin{aligned}
 -\mathbb{D}_f = \int_0^1 & \frac{1}{48} \Psi_f^2 y^6 + \frac{1}{8} A \Psi_f y^5 + \left( \frac{1}{4} B \Psi_f + \frac{1}{6} A^2 + \frac{1}{24} B \Psi_f \right) y^4 \\
 & + \left( \frac{1}{2} M_1 \Psi_f + \frac{1}{2} AB + \frac{1}{6} AB \right) y^3 \\
 & + \left( AM_1 + \frac{1}{2} B^2 \right) y^2 + BM_1 y \quad dy
 \end{aligned} \tag{C.102}$$

integrate:

$$\begin{aligned}
 -\mathbb{D}_f = & \frac{1}{48} \frac{1}{7} \Psi_f^2 + \frac{1}{8} \frac{1}{6} A \Psi_f + \frac{1}{5} \left( \frac{1}{4} B \Psi_f + \frac{1}{6} A^2 + \frac{1}{24} B \Psi_f \right) \\
 & + \frac{1}{4} \left( \frac{1}{2} M_1 \Psi_f + \frac{1}{2} AB + \frac{1}{6} AB \right) + \frac{1}{3} \left( AM_1 + \frac{1}{2} B^2 \right) + \frac{1}{2} BM_1
 \end{aligned} \tag{C.103}$$

gives:

$$\begin{aligned}
 -\mathbb{D}_f = & \frac{1}{336} \Psi_f^2 + \frac{1}{48} A \Psi_f + \frac{1}{5} \left( \frac{7}{24} B \Psi_f + \frac{1}{6} A^2 \right) \\
 & + \frac{1}{4} \left( \frac{1}{2} M_1 \Psi_f + \frac{2}{3} AB \right) + \frac{1}{3} AM_1 + \frac{1}{6} B^2 + \frac{1}{2} BM_1
 \end{aligned} \tag{C.104}$$

open the bracket:

$$-\mathbb{D}_f = \frac{1}{336} \Psi_f^2 + \frac{1}{48} A \Psi_f + \frac{7}{120} B \Psi_f + \frac{1}{30} A^2 + \frac{1}{8} M_1 \Psi_f + \frac{1}{6} AB + \frac{1}{3} AM_1 + \frac{1}{6} B^2 + \frac{1}{2} BM_1 \tag{C.105}$$

substitute  $M_1$  we can have these multiplications:

$$M_1 \Psi_f = -\frac{1}{6} \Psi_f^2 - \frac{1}{2} A \Psi_f - B \Psi_f \tag{C.106}$$

$$M_1 A = -\frac{1}{6} A \Psi_f - \frac{1}{2} A^2 - AB \tag{C.107}$$

$$M_1 B = -\frac{1}{6} B \Psi_f - \frac{1}{2} AB - B^2 \tag{C.108}$$

then:

$$-\mathbb{D}_f = \frac{1}{336}\Psi_f^2 + \frac{1}{48}A\Psi_f + \frac{7}{120}B\Psi_f + \frac{1}{30}A^2 + \frac{1}{8}\left(-\frac{1}{6}\Psi_f^2 - \frac{1}{2}A\Psi_f - B\Psi_f\right) \quad (\text{C.109})$$

$$+ \frac{1}{6}AB + \frac{1}{3}\left(-\frac{1}{6}A\Psi_f - \frac{1}{2}A^2 - AB\right) + \frac{1}{6}B^2 + \frac{1}{2}\left(-\frac{1}{6}B\Psi_f - \frac{1}{2}AB - B^2\right)$$

$$-\mathbb{D}_f = \left(\frac{1}{336} - \frac{1}{48}\right)\Psi_f^2 + \left(\frac{1}{48} - \frac{1}{16} - \frac{1}{18}\right)A\Psi_f + \left(\frac{7}{120} - \frac{1}{8} - \frac{1}{12}\right)B\Psi_f \quad (\text{C.110})$$

$$+ \left(\frac{1}{30} - \frac{1}{6}\right)A^2 + \left(\frac{1}{6} - \frac{1}{2}\right)B^2 + \left(\frac{1}{6} - \frac{1}{3} - \frac{1}{4}\right)AB$$

$$\boxed{\mathbb{D}_f = \frac{1}{58}\Psi_f^2 + \frac{7}{72}A\Psi_f + \frac{3}{20}B\Psi_f + \frac{2}{15}A^2 + \frac{1}{3}B^2 + \frac{5}{12}AB} \quad (\text{C.111})$$

#### C.4.1 Calculate $\mathbb{D}_f$

we need:

$$\mathcal{D}_f = -\left(\frac{\mathbb{M}}{u_f}\right)' \Big|_{y=0} \quad (\text{C.112})$$

we know:

$$\mathcal{D}_f = -\left(\frac{\mathbb{M}'u_f - u_f'\mathbb{M}}{u_f^2}\right)_{y=0} \quad (\text{C.113})$$

and:

$$\mathbb{M}_{y=0} = 0 \quad (\text{C.114})$$

$$\mathbb{M}'_{y=0} = -\frac{\Psi_f}{6} - \frac{A}{2} - B \quad (\text{C.115})$$

$$(u_f)_{y=0} = B \quad (\text{C.116})$$

$$(u_f')_{y=0} = A \quad (\text{C.117})$$

therefore:

$$\mathcal{D}_f = \frac{1}{B^2} \left( \frac{1}{6} B \Psi_f + \frac{1}{2} AB + B^2 \right) \quad (\text{C.118})$$

finally:

$$\kappa = \frac{1}{Pe_f} + Pe_f \frac{\mathbb{D}_f}{1 + \mathcal{D}_f} \quad (\text{C.119})$$

leads to:

$$\kappa = \frac{1}{Pe_f} + Pe_f \frac{\frac{1}{58} \Psi_f^2 + \frac{7}{72} A \Psi_f + \frac{3}{20} B \Psi_f + \frac{2}{15} A^2 + \frac{1}{3} B^2 + \frac{5}{12} AB}{1 + \frac{1}{B^2} \left( \frac{1}{6} B \Psi_f + \frac{1}{2} AB + B^2 \right)} \quad (\text{C.120})$$

# Bibliography

- [1] Angel Abarca, Pilar Gomez-Sal, Avelino Martin, Miguel Mena, Josep Maria Poblet, and Carlos Yelamos. Ammonolysis of mono (pentamethylcyclopentadienyl) titanium iv derivatives. *Inorg. Chem.*, 39(4):642–651, 2000.
- [2] Colin D. Abernethy, Gareth M. Codd, Mark D. Spicer, and Michelle K. Taylor. A highly stable N-heterocyclic carbene complex of trichloro-oxo-vanadium(V) displaying novel Cl—C(carbene) bonding interactions. *J. Am. Chem. Soc.*, 125(5):1128–1129, 2003.
- [3] R. C. Acharya, S. E. A. T. M. Van der Zee, and A. Leijnse. Transport modeling of nonlinearly adsorbing solutes in physically heterogeneous pore networks. *Water Resour. Res.*, 41:W02020, 2005.
- [4] Tinku Acharya and Ajoy K Ray. *Image processing: principles and applications*. John Wiley & Sons, 2005.
- [5] P. M. Adler. *Porous Media: Geometry and Transports*. Butterworth-Heinemann, 1992.
- [6] Ronald J Adrian. Particle-imaging techniques for experimental fluid mechanics. *Annual review of fluid mechanics*, 23(1):261–304, 1991.
- [7] Michel Al-Chidiac, Parisa Mirbod, Yiannis Andreopoulos, and Sheldon Weinbaum. Dynamic compaction of soft compressible porous materials: experiments on air-solid phase interaction. *J. Porous Media*, 12(11), 2009.
- [8] F. J. Alexander, A. L. Garcia, and D. M. Tartakovsky. Algorithm refinement for stochastic partial differential equations: 1. Linear diffusion. *J. Comp. Phys.*, 182:47–66, 2002.
- [9] Leah N. Appelhans, Daniele Zuccaccia, Anes Kovacevic, Anthony R. Chianese, John R. Miecznikowski, Aleco Macchioni, Eric Clot, Odile Eisenstein, and Robert H. Crabtree. An anion-dependent switch in selectivity results from a change of C—H activation mechanism in the reaction of an imidazolium salt with  $\text{IrH}_5(\text{PPh}_3)_2$ . *J. Am. Chem. Soc.*, 127(46):16299–16311, 2005.

- [10] Anthony J. Arduengo, III, H. V. Rasika Dias, Richard L. Harlow, and Michael Kline. Electronic stabilization of nucleophilic carbenes. *J. Am. Chem. Soc.*, 114(14):5530–5534, 1992.
- [11] Anthony J. Arduengo, III, Siegfried F. Gamper, Joseph C. Calabrese, and Fredric Davidson. Low-coordinate carbene complexes of nickel(0) and platinum(0). *JACSAT*, 116(10):4391–4394, 1994.
- [12] R. Aris. On the dispersion of a solute in a fluid flowing through a tube. *P R. Soc. London*, 235(1200):67–77, 1956.
- [13] G. F. Arkin and E. R. Perrier. Vorticular air flow within an open row crop canopy. *Agric. meteorol.*, 13:359–374, 1974.
- [14] J.-L. Auriault. About the Beavers and Joseph boundary condition. *Transp. Porous Med.*, 2009.
- [15] J.-L. Auriault. On the domain of validity of Brinkman's equation. *Transp. Porous Med.*, 79:215–223, 2009.
- [16] J. L. Auriault and P. M. Adler. Taylor dispersion in porous media: Analysis by multiple scale expansions. *Adv. Water Resour.*, 18(4):217–226, 1995.
- [17] J.-L. Auriault and P. M. Adler. Taylor dispersion in porous media: analysis by multiple scale expansions. *Adv. Water Resour.*, 18(4):217–226, 1995.
- [18] J. L. Auriault, C. Geindreau, and C. Boutin. Filtration law in porous media with poor separation of scales. *Transp. Porous Med.*, 60:89–108, 2005.
- [19] J.-L. Auriault and J. Lewandowska. Effective Diffusion Coefficient: from Homogenization to Experiment. *Phil. Transp. Porous Media*, 27:205–223, 1997.
- [20] AA Ayon, RL Bayt, and KS Breuer. Deep reactive ion etching: a promising technology for micro- and nanosatellites. *Smart materials and structures*, 10(6):1135, 2001.
- [21] G. B. K. Baines. Turbulence in a wheat crop. *Agric. meteorol.*, 10:93–105, 1972.
- [22] Ron L Bardell, Nigel R Sharma, Fred K Forster, Martin A Afromowitz, Robert J Penney, et al. Designing high-performance micro-pumps based on non-moving-parts valves. *ASME-PUBLICATIONS-HTD*, 354:47–54, 1997.
- [23] G. I. Barenblatt, V. M. Entov, and V. M. Ryzhik. *Theory of fluid flows through natural rocks*. Kluwer, Boston, 1990.



- [24] Patrick Barreau, Henri Bertin, Didier Lasseux, Philippe Glénat, Alan Zaitoun, et al. Water control in producing wells: influence of an adsorbed-polymer layer on relative permeabilities and capillary pressure. *SPE Reservoir Engineering*, 12(04):234–239, 1997.
- [25] G. K. Batchelor. *An introduction to fluid dynamics*. Cambridge University Press, New York, USA, 2009.
- [26] I. Battiato. Self-similarity in coupled Brinkman/Navier-Stokes flows. *J. Fluid Mech.*, 699:94–114, 2012.
- [27] I. Battiato. Effective medium theory for drag-reducing micro-patterned surfaces in turbulent flows. *Eur. Phys. J. E*, 37(19), 2014.
- [28] I. Battiato, P. Bandaru, and D. M. Tartakovsky. Elastic response of carbon nanotube forests to aerodynamic stresses. *Phys. Rev. Lett.*, 105(144504), 2010.
- [29] I. Battiato and S. Rubol. Single-parameter model of vegetated aquatic flows. *Water Resour. Res.*, 50:doi:10.1002/2013WR015065, 2014.
- [30] I. Battiato and D. M. Tartakovsky. Applicability regimes for macroscopic models of reactive transport in porous media. *J. Contam. Hydrol.*, 120:18–26, 2011.
- [31] I. Battiato, D. M. Tartakovsky, A. M. Tartakovsky, and T. Scheibe. On breakdown of macroscopic models of mixing-controlled heterogeneous reactions in porous media. *Adv. Water Resour.*, 32:1664–1673, 2009.
- [32] I. Battiato and J. Vollmer. Flow-induced shear instabilities of cohesive granulates. *Phys. Rev. E*, 86(031301), 2012.
- [33] R.H. Baughman, A. A. Zakhidov, and W. A. de Heer. Carbon nanotubes-the route toward applications. *Science*, 297(2):787–793, 2002.
- [34] G. S. Beavers and D. D. Joseph. Boundary conditions at a naturally permeable wall. *J. Fluid Mech.*, 30(01):197–207, 1967.
- [35] F. P. Beer, J. E. R. Johnson, and J. T. De Wolf. *Mechanics of Materials*. McGraw Hill, Boston, 4th edition, 2006.
- [36] B. Berkowitz and H. Scher. The role of probabilistic approaches to transport theory in heterogeneous media. *Transport Porous Med.*, 42:241–263, 2001.
- [37] B. Berkowitz and J. Zhou. Reactive solute transport in a single fracture. *Water Resour. Res.*, 32(4):901–913, 1996.

- [38] Heinrich Blasius. Das Ähnlichkeitsgesetz bei Reibungsvorgängen in Flüssigkeiten. In *Mitteilungen über Forschungsarbeiten auf dem Gebiete des Ingenieurwesens*, pages 1–41. Springer, 1913.
- [39] Martin J Blunt. Flow in porous media—pore-network models and multiphase flow. *Current opinion in colloid & interface science*, 6(3):197–207, 2001.
- [40] J. Bodin, F. Delay, and G. De Marsily. Solute transport in a single fracture with negligible matrix permeability: 1. fundamental mechanisms. *Hydrogeol. J.*, 11(4):418–433, 2003.
- [41] R Bora, BB Maini, A Chakma, et al. Flow visualization studies of solution gas drive process in heavy oil reservoirs using a glass micromodel. In *International Thermal Operations and Heavy Oil Symposium*. Society of Petroleum Engineers, 1997.
- [42] F. Boso and I. Battiato. Homogenizability conditions of multicomponent reactive transport processes. *Adv. Water Resour.*, 62:254–265, 2013.
- [43] L. Bouquet and E. Lauga. A smooth future? *Nat. Mater.*, 10(334-337), 2011.
- [44] P. P. Brahma and T. C. Harmon. The effect of multicomponent diffusion on NAPL dissolution from spherical ternary mixtures. *J. Contam. Hydrol.*, 67, 2003. doi:10.1016/S0169-7722(03)00087-1.
- [45] H. Brenner. Dispersion resulting from flow through spatially periodic porous media. *Phil. Trans. R. Soc. Lond.*, A297:81–133, 1980.
- [46] H. Brenner. Dispersion resulting from flow through spatially periodic porous media. *Philos. T. Roy. Soc. A*, 297(1430):81–133, 1980.
- [47] H. Brenner. *Transport Processes in Porous Media*. McGraw-Hill, 1987.
- [48] Howard Brenner. *Macrotransport processes*. Elsevier, 2013.
- [49] S. L. Briant and K.E Thompson. Theory, modeling and experiments in reactive transport in porous media. *Curr. Opin. colloid Interface Sci.*, 6(3):217–222, 2001.
- [50] H. C. Brinkman. A calculation of the viscous force exerted by a flowing fluid on a dense swarm of particles. *Appl. Sci. Res.*, A1:27–34, 1949.
- [51] H. C. Brinkman. On the permeability of media consisting of closely packed porous particles. *Appl. Sci. Res.*, 1(1):81–86, 1949.
- [52] S. Broyda, M. Dentz, and D. M. Tartakovsky. Probability density functions for

- advective-reactive transport in radial flow. *Stoch. Environ. Res. Risk Assess.*, pages doi:10.1007/s00477-010-0401-4, 2010.
- [53] Y. Brunet, J.J. Finnigan, and M. R. Raupach. A wind tunnel study of air flow in waving wheat: single-point velocity statistics. *Bound.-Layer Meteorol.*, 70:95–132, 1994.
- [54] Patrick Bunton, D Marin, Simone Stewart, E Meiburg, and A De Wit. Schlieren imaging of viscous fingering in a horizontal hele-shaw cell. *Experiments in Fluids*, 57(2):1–11, 2016.
- [55] S. L. Candelaria, Y. Shao, W. Zhou, X. Li, J. Xiao, J. G. Zhang, Y. Wang, J. Liu, J. Li, and G. Cao. Nanostructured carbon for energy storage and conversion. *Nano Energy*, 1:195–220, 2012.
- [56] Liang-Cheng Chang, Hung-Hui Chen, Hsin-Yu Shan, and Jui-Pin Tsai. Effect of connectivity and wettability on the relative permeability of naps. *Environmental geology*, 56(7):1437–1447, 2009.
- [57] Alfred Chatenever, John C Calhoun Jr, et al. Visual examinations of fluid behavior in porous media-part i. *Journal of Petroleum Technology*, 4(06):149–156, 1952.
- [58] Il Chatzis, A Kantzas, FAL Dullien, et al. On the investigation of gravity-assisted inert gas injection using micromodels, long berea sandstone cores, and computer-assisted tomography. In *SPE Annual Technical Conference and Exhibition*. Society of Petroleum Engineers, 1988.
- [59] J-T Cheng and N Giordano. Fluid flow through nanometer-scale channels. *Physical review E*, 65(3):031206, 2002.
- [60] John M Christie and Alison Ord. Flow stress from microstructures of mylonites: example and current assessment. *Journal of Geophysical Research: Solid Earth*, 85(B11):6253–6262, 1980.
- [61] M.A. Christie. Upscaling for reservoir simulation. *J. Petrol. Technol.*, 48:1004–1010, 1996.
- [62] RL Chuoke, P Van Meurs, C van der Poel, et al. The instability of slow, immiscible, viscous liquid-liquid displacements in permeable media. *Society of Petroleum Engineers*, 1959.
- [63] O. Cirpka, E. Frind, and R. Helming. Numerical simulation of biodegradation controlled by transverse mixing. *J. Contam. Hydrol.*, 40:159–182, 1999.

- [64] Anne M. Coghill and Lorrin R. Garson, editors. *The ACS Style Guide*. Oxford University Press, Inc. and The American Chemical Society, New York, 3 edition, 2006.
- [65] Stephen H Conrad, John L Wilson, William R Mason, and William J Peplinski. Visualization of residual organic liquid trapped in aquifers. *Water Resources Research*, 28(2):467–478, 1992.
- [66] M. Corbella, C. Ayora, and E. Cardellach. Hydrothermal mixing, carbonate dissolution and sulfide precipitation in mississippi valley-type deposits. *Mineral Deposita*, 39:344–357, 2004.
- [67] S. Cornell and M. Droz. Steady-state reaction-diffusion front scaling for  $ma + nb \rightarrow$  [inert]. *Phys. Rev. Lett.*, 70:3824, 1993.
- [68] Christophe Cottin, Hugues Bodiguel, and Annie Colin. Drainage in two-dimensional porous media: From capillary fingering to viscous flow. *Physical Review E*, 82(4):046315, 2010.
- [69] Frank Albert Cotton, Geoffrey Wilkinson, Carlos A. Murillio, and Manfred Bochmann. *Advanced Inorganic Chemistry*. Wiley, Chichester, United Kingdom, 6 edition, 1999.
- [70] P. V. Coveney and P. W. Fowler. Modelling biological complexity: A physical scientist’s perspective. *J. R. Soc. Interface*, 2:267–280, 2005.
- [71] Jiayi Cui, Daniel Daniel, Alison Grinthal, Kaixiang Lin, and Joanna Aizenberg. Dynamic polymer systems with self-regulated secretion for the control of surface properties and material healing. *Nat. mater.*, 14(8):790–795, 2015.
- [72] W.A. Curtin and R.E. Miller. Atomistic/continuum coupling in computational materials science. *Modelling Simul. Mater. Sci. Eng.*, 11:R33–R68, 2003.
- [73] H. Darcy. Les fontaines publiques de la ville de dijon. *Victor Darmon*, Paris, 1856.
- [74] Henry Darcy. *Les fontaines publiques de la ville de Dijon: exposition et application...* Victor Dalmont, 1856.
- [75] A. M. J. Davis and E. Lauga. Hydrodynamic friction of fakir-like superhydrophobic surfaces. *J. Fluid Mech.*, 661:402–411, 2010.
- [76] G. de Marsily. *Quantitative Hydrogeology*. Academic Press, San Diego, California, 1986.

- [77] C.P. Deck, C. Ni, K. S. Vecchio, and P.R. Bandaru. The response of carbon nanotube ensembles to fluid flow: Applications to mechanical property measurement and diagnostics. *J. Appl. Phys.*, 106:074304, 2009.
- [78] CP Deck, C Ni, KS Vecchio, and PR Bandaru. The response of carbon nanotube ensembles to fluid flow: Applications to mechanical property measurement and diagnostics. *J. Appl. Physics*, 106(7):74304, 2009.
- [79] M. Dejam, H. Hassanzadeh, and Z. Chen. Shear dispersion in a fracture with porous walls. *Adv. Water Resour.*, 74:14–25, 2014.
- [80] Marco Dentz and Jesus Carrera. Mixing and spreading in stratified flow. *Physics of Fluids (1994-present)*, 19(1):017107, 2007.
- [81] P.A.M. Dirac. The lorentz transformation and absolute time. *Physica*, 19(1–12):888–896, 1953.
- [82] M.G. Doyle and R.L. Alien. Subsea-floor replacement in volcanic-hosted massive sulfide deposits. *Ore Geol. Rev.*, 23:183–222, 2003.
- [83] M. Droz. Fronts and Pattern Formation in Reaction-Diffusion Systems. In Springer, editor, *Anomalous diffusion from Basics to Applications*, pages 211–220. Springer, Berlin/Heidelberg, 1999.
- [84] C. J. Van Duijn and I. S. Pop. Crystal dissolution and precipitation in porous media: pore-scale analysis. *J. Reine Angew. Math.*, 577:171–211, 2004.
- [85] A Durandet, Y Arnal, J Pelletier, and C Pomot. Anisotropy and kinetics of the etching of tungsten in sf6 multipolar microwave plasma. *Journal of applied physics*, 67(5):2298–2302, 1990.
- [86] A Durandet, O Joubert, J Pelletier, and M Pichot. Effects of ion bombardment and chemical reaction on wafer temperature during plasma etching. *Journal of applied physics*, 67(8):3862–3866, 1990.
- [87] L. Durlofsky and J. F. Brady. Analysis of the brinkman equation as a model for flow in porous media. *Phys. Fluids*, 30(11):3329–3341, 2009.
- [88] W. E. B. Engquist, and Z. Huang. Heterogeneous multiscale method: a general methodology for multiscale modeling. *Phys. Rev. B*, 67(9):092101, 2003.
- [89] Y. Efendief and L. J. Durlofsky. Numerical modeling of subgrid heterogeneity in two phase flow simulations. *Water Resour. Res.*, 38(8), 2002. 10.1029/2000WR000190.

- [90] Y. Efendief and L. J. Durlofsky. A generalized convection-diffusion model for subgrid transport in porous media. *Multiscale Model. Simul.*, 1(3):504–526, 2003.
- [91] Y. Efendief, L. J. Durlofsky, and S. H. Lee. Modeling of subgrid effects in coarse-scale simulations of transport in heterogeneous porous media. *Water Resour. Res.*, 36(8):2031–2041, 2000.
- [92] S. Emmanuel and B. Berkovitz. Mixing-induced precipitation and porosity evolution in porous media. *Adv. Wat. Res.*, 28:337–344, 2005.
- [93] Arthur Erdélyi, Wilhelm Magnus, Fritz Oberhettinger, and Francesco G Tricomi. *Tables of Integral Transforms: Vol.: 1.* McGraw-Hill Book Company, Incorporated, 1954.
- [94] JP Esquivel, T Senn, P Hernández-Fernández, J Santander, M Lörger, S Rojas, B Löchel, C Cané, and N Sabaté. Towards a compact su-8 micro-direct methanol fuel cell. *Journal of Power Sources*, 195(24):8110–8115, 2010.
- [95] M. R. Falvo, G. J. Clary, R. M. Taylor, V. Chi, F. P. Brooks, S. Washburn, and R. Superfine. Bending and buckling of carbon nanotubes under large strain. *Nature*, 1997.
- [96] Fang Fang and Tayfun Babadagli. 3-d visualization of diffusive and convective solvent transport processes in oil-saturated porous media using laser technology. *Journal of Visualization*, pages 1–15, 2016.
- [97] Andrea Ferrari, Joaquin Jimenez-Martinez, Tanguy Le Borgne, Yves Méheust, and Ivan Lunati. Challenges in modeling unstable two-phase flow experiments in porous micromodels. *Water Resources Research*, 51(3):1381–1400, 2015.
- [98] R.P Feynman and E.L Vernon Jr. The theory of a general quantum system interacting with a linear dissipative system. *Annals of Physics*, 24:118–173, 1963.
- [99] Adolf Fick. Ueber diffusion. *Annalen der Physik*, 170(1):59–86, 1855.
- [100] J.J. Finnigan. Turbulence in waving wheat. *Bound.-Layer Meteorol.*, 16:213–236, 1978.
- [101] J.J. Finnigan. Turbulence in plant canopies. *Ann. Rev. Fluid Mech.*, 32:519–571, 2000.
- [102] J.J. Finnigan and P.J. Mulhearn. Modelling waving crops in a wind tunnel. *Bound.-Layer Meteorol.*, 14:253–277, 1978.

- [103] A.N. Ford and D.V. Papavassiliou. Flow around surface-attached carbon nanotubes. *Ind. Eng. Chem. Res.*, 45:1797–1804, 2006.
- [104] I Frankel and H Brenner. On the foundations of generalized Taylor dispersion theory. *Journal of Fluid Mechanics*, 204:97–119, 1989.
- [105] E. Friedman-Hill. *Writing Rules in Jess*. Manning Publications Co., Greenwich, CT, USA, 1 edition, 2003.
- [106] L. Galfi and Z. Racz. Properties of the reaction front in an  $a+b \rightarrow c$  type reaction-diffusion process. *Phys. Rev.*, A38:3151, 1988.
- [107] W. Gao, R. H. Shaw, and K.T. Paw U. Observation of organized structure in turbulent flow within and above a forest canopy. *Bound.-Layer Meteorol.*, 47:349–377, 1989.
- [108] Marco Ghisalberti. Obstructed shear flows: similarities across systems and scales. *J. Fluid Mech.*, 641:51–61, 2009.
- [109] S. Ghosh, A. K. Sood, and N. Kumar. Carbon nanotube flow sensors. *Science*, 2003.
- [110] S. Gilroy and D. L. Jones. Through form to function: Root hair development and nutrient uptake. *Trends Plant Sci.*, 5:56–60, 2000.
- [111] R. A. Gingold and J.J. Monaghan. Smoothed particle hydrodynamics: theory and application to non-spherical stars. *Royal Astronomical Society, Monthly Notices*, 181:375–389, 1977.
- [112] Afshin Goharzadeh, Arzhang Khalili, and Bo Barker Jørgensen. Transition layer thickness at a fluid-porous interface. *Phys. Fluids*, 17(5):057102, 2005.
- [113] B. Goyeau, T. Benihaddadene, D. Gobin, and M. Quintard. Averaged momentum equation for flow through a nonhomogeneous porous structure. *Transp. Porous Media*, 28:19–50, 1997.
- [114] Jay W Grate, Marvin G Warner, Jonathan W Pittman, Karl J Dehoff, Thomas W Wietsma, Changyong Zhang, and Mart Oostrom. Silane modification of glass and silica surfaces to obtain equally oil-wet surfaces in glass-covered silicon micromodel applications. *Water Resources Research*, 49(8):4724–4729, 2013.
- [115] Jay W Grate, Changyong Zhang, Thomas W Wietsma, Marvin G Warner, Norman C Anheier, Bruce E Bernacki, Galya Orr, and Mart Oostrom. A note on the visualization of wetting film structures and a nonwetting immiscible fluid in a pore network micromodel using a solvatochromic dye. *Water Resources*

*Research*, 46(11), 2010.

- [116] W. G. Gray and C. T. Miller. Thermodynamically constrained averaging theory approach for modeling flow and transport phenomena in porous medium systems: 1. Motivation and overview. *Adv. Water Resour.*, 28(2):161–180, 2005.
- [117] William G Gray and PCY Lee. On the theorems for local volume averaging of multiphase systems. *International Journal of Multiphase Flow*, 3(4):333–340, 1977.
- [118] I. M. Griffiths, P. D. Howell, and R. J. Shipley. Control and optimization of solute transport in a thin porous tube. *Phys. Fluids*, 25(3):033101, 2013.
- [119] G. E. Grisak and J. F. Pickens. Solute transport through fractured media, 1. The effect of matrix diffusion. *Water Resour. Res.*, 16(4):719–730, 1980.
- [120] G. E. Grisak, J. F. Pickens, and J. A. Cherry. Solute transport through fractured media, 2. Column study of fractured till. *Water Resour. Res.*, 16(4):731, 1980.
- [121] Alexander Gruenberger, Christopher Probst, Antonia Heyer, Wolfgang Wiechert, Julia Frunzke, and Dietrich Kohlheyer. Microfluidic picoliter bioreactor for microbial single-cell analysis: Fabrication, system setup, and operation. *JoVE*, 1(82):e50560–e50560, 2013.
- [122] P. Guo, A. M. Weinstein, and S. Weinbaum. A hydrodynamic mechanosensory hypothesis for brush border microvilli. *Am. J. Physiol. Renal Physiol.*, 279:F698–F712, 2000.
- [123] N. G. Hadjiconstantinou. Hybrid atomistic-continuum formulations and the moving contact-line problem. *J. Comp. Physics*, 154(2):245–265, 1999.
- [124] J. Happel. Viscous flow in multiparticle systems: slow motion of fluids relative to beds of spherical particles. *AIChE J.*, 4(2):197–201, 1958.
- [125] J. Happel. Viscous flow relative to arrays of cylinders. *AIChE J.*, 5:174–177, 1959.
- [126] V. M. Harik. Ranges of applicability for the continuum beam model in the mechanics of carbon nanotubes and nanorods. *Solid State Commun.*, 120:331, 2001.
- [127] Robert J Harris, Andrew J Sederman, Michael D Mantle, John Crawshaw, and Michael L Johns. A comparison of experimental and simulated propagators in porous media using confocal laser scanning microscopy, lattice boltzmann hydrodynamic simulations and nuclear magnetic resonance. *Magnetic resonance imaging*, 23(2):355–357, 2005.



- [128] Yassin A Hassan and EE Dominguez-Ontiveros. Flow visualization in a pebble bed reactor experiment using piv and refractive index matching techniques. *Nuclear Engineering and Design*, 238(11):3080–3085, 2008.
- [129] Behrooz Hassani and Ernest Hinton. A review of homogenization and topology optimization i—homogenization theory for media with periodic structure. *Computers & Structures*, 69(6):707–717, 1998.
- [130] S Majid Hassanizadeh and William G Gray. Mechanics and thermodynamics of multiphase flow in porous media including interphase boundaries. *Advances in water resources*, 13(4):169–186, 1990.
- [131] F Hesse, F. A. Radu, M. Thullner, and S. Attinger. Upscaling of the advection-diffusion-reaction equation with Monod reaction. *Adv. Water Resour.*, 32:1336–1351, 2009.
- [132] Christopher D Himmel and Gary S May. Advantages of plasma etch modeling using neural networks over statistical techniques. *IEEE Transactions on semiconductor manufacturing*, 6(2):103–111, 1993.
- [133] Cyril W Hirt and Billy D Nichols. Volume of fluid (vof) method for the dynamics of free boundaries. *Journal of computational physics*, 39(1):201–225, 1981.
- [134] R. N. Horne and F. Rodriguez. Dispersion in tracer flow in fractured geothermal systems. *Geophys. Res. Lett.*, 10(4):289–292, 1983.
- [135] U. Hornung. *Homogenization and Porous Media*. Springer, New York, 1997.
- [136] Mark F Horstemeyer. Multiscale modeling: a review. In *Practical aspects of computational chemistry*, pages 87–135. Springer, 2009.
- [137] X. Hou, Y. Hu, A. Grinthal, M. Khan, and J. Aizenberg. Liquid-based gating mechanism with tunable multiphase selectivity and antifouling behaviour. *Nature*, 519:70–73, 2015.
- [138] F. A. Howes and S. Whitaker. The spatial averaging theorem revisited. *Chem. Engng Sc.*, 40:1387–1392, 1985.
- [139] J. Y. Huang, S. Chen, Z. Q. Wang, K. Kempa, Y. M. Wang, S. H. Jo, G. Chen, M. S. Dresselhaus, and Z. F. Ren. Superplatic carbon nanotubes. *Nature*, 2006.
- [140] Charles W Hull. Apparatus for production of three-dimensional objects by stereolithography, March 11 1986. US Patent 4,575,330.
- [141] R. L. Jacobson and D. Langmuir. Dissociation constant of calcite and  $cahco_3^+$

from 0 to 50 c. *Geochimica et Cosmochimica Acta*, 38:301–318, 1974.

- [142] Henri Jansen, Han Gardeniers, Meint de Boer, Miko Elwenspoek, and Jan Fluitman. A survey on the reactive ion etching of silicon in microtechnology. *Journal of micromechanics and microengineering*, 6(1):14, 1996.
- [143] Z. Jiang and C. Ebner. Simulation study of reaction fronts. *Phys. Rev. A*, 42:7483–7486, 1990.
- [144] Vasilii Vasil'evich Jikov, Sergei M Kozlov, and Olga Arsen'evna Oleinik. *Homogenization of differential operators and integral functionals*. Springer Science & Business Media, 2012.
- [145] P. Joseph, C. Cottin-Bizonne, J.-M. Benoit, C. Ybert, C. Journet, P. Tabeling, and L. Bocquet. Slippage of water past superhydrophobic carbon nanotube forests in microchannels. *Phys. Rev. Lett.*, 97:156104, 2006.
- [146] Q. Kang, D. Zhang, P. Lichtner, and I. N. Tsimpanogiannis. Lattice boltzmann model for crystal growth from supersaturated solution. *Geophys. Res. Lett.*, 31:L21604. doi:10.1029/2004GL021107, 2004.
- [147] NK Karadimitriou and SM Hassanizadeh. A review of micromodels and their use in two-phase flow studies. *Vadose Zone Journal*, 11(3), 2012.
- [148] NK Karadimitriou, V Joekar-Niasar, SM Hassanizadeh, PJ Kleingeld, and LJ Pyrak-Nolte. A novel deep reactive ion etched (drie) glass micro-model for two-phase flow experiments. *Lab on a Chip*, 12(18):3413–3418, 2012.
- [149] C. M. Kazezyilmaz-Alhan. Analytical solutions for contaminant transport in streams. *J. Hydrol.*, 348(3):524–534, 2008.
- [150] RD Keane, RJ Adrian, and Y Zhang. Super-resolution particle imaging velocimetry. *Measurement Science and Technology*, 6(6):754, 1995.
- [151] P. E. Kechagia, I. N. Tsimpanogiannis, Y. C. Yortsos, and P. C. Lichtner. On the upscaling of reaction-transport processes in porous media with fast or finite kinetics. *Chem. Engrg. Sci.*, 57(13):2565–2577, 2002.
- [152] AA Keller. High resolution cat imaging of fractures in consolidated materials. *International Journal of Rock Mechanics and Mining Sciences*, 34(3):155–e1, 1997.
- [153] Arturo A Keller, Martin J Blunt, and Arturo Paul V Roberts. Micromodel observation of the role of oil layers in three-phase flow. *Transport in Porous Media*, 26(3):277–297, 1997.

- [154] Enoch Kim, Younan Xia, Milan Mrksich, Rebecca J Jackman, Xiao-Mei Zhao, Stephen P Smith, Mara G Prentiss, George M Whitesides, and Christian Marzolin. Method of forming articles including waveguides via capillary micro-molding and microtransfer molding, March 12 2002. US Patent 6,355,198.
- [155] Enoch Kim, Younan Xia, and George M Whitesides. Micromolding in capillaries: applications in materials science. *Journal of the American Chemical Society*, 118(24):5722–5731, 1996.
- [156] Enoch Kim, Younan Xia, and George M Whitesides. Two- and three-dimensional crystallization of polymeric microspheres by micromolding in capillaries. *Advanced Materials*, 8(3):245–247, 1996.
- [157] P. Kim and C. M. Lieber. Nanotube nanotweezers. *Science*, 1999.
- [158] Enoch King, Younan Xia, Xiao-Mei Zhao, and George M Whitesides. Solvent-assisted microcontact molding: A convenient method for fabricating three-dimensional structures on surfaces of polymers. *Advanced Materials*, 9(8):651–654, 1997.
- [159] Peter K Kitanidis. Prediction by the method of moments of transport in a heterogeneous formation. *Journal of Hydrology*, 102(1):453–473, 1988.
- [160] P. Knabner, C. J. Van Duijn, and S. Hengst. An analysis of crystal dissolution fronts in flows through porous media. Part 1: Compatible boundary conditions. *Adv. Water Resour.*, 18(3):171–185, 1995.
- [161] Jasper Knight and Stefan W Grab. Lightning as a geomorphic agent on mountain summits: evidence from southern africa. *Geomorphology*, 204:61–70, 2014.
- [162] C. Knutson, A. Valocchi, and C. Werth. Comparison of continuum and pore-scale models of nutrient biodegradation under transverse mixing conditions. *Adv. Water Resour.*, 30(6-7):1421–1431, 2007.
- [163] C. Knutson, A. Valocchi, and C. Werth. Comparison of continuum and pore-scale models of nutrient biodegradation under transverse mixing conditions. *Adv. Water Resour.*, 30:1421–1431, 2007.
- [164] Donald L Koch and John F Brady. Dispersion in fixed beds. *Journal of Fluid Mechanics*, 154:399–427, 1985.
- [165] E.M. Kotsalis, J.H. Walther, and P. Koumoutsakos. Multiphase water flow inside carbon nanotubes. *Int. J. Multiphase Flow*, 30:995–1010, 2004.
- [166] A. Krishnan, E. Dujardin, T.W. Ebbesen, P. N. Yanilos, and M. M. Treacy. Young's

- modulus of single-walled nanotubes. *Phys. Rev. B*, 58(20), 1998.
- [167] B Kruijt, Y Malhi, J Lloyd, AD Norbre, AC Miranda, MGP Pereira, A Culf, and J Grace. Turbulence statistics above and within two amazon rain forest canopies. *Bound-Lay. Meteorol.*, 94(2):297–331, 2000.
- [168] P. K. Kundu and I. M Cohen. *Fluid Mechanics*. Elsevier, San Diego, 4th edition, 2008.
- [169] P. K. Kundu and I. M. Cohen. *Fluid mechanics*. Elsevier Academic Press, San Diego, CA, 3rd edition, 2009.
- [170] Horace Lamb. *A Treatise on the Mathematical Theory of the Motion of Fluids*. The University Press, 1879.
- [171] Horace Lamb. *Hydrodynamics*. Cambridge The University Press, 1895.
- [172] O Lamrous, D Houi, C Zarcone, and J Pradere. Magnetic resonance imaging application to study of porous media. *Revue De Physique Appliquée*, 24(5):607–612, 1989.
- [173] P. Langlo and M. S. Espedal. Macrodispersion for two-phase, immiscible flow in porous media. *Adv. Water Resour.*, 17:297–316, 1994.
- [174] E. Lauga and H. A. Stone. Effective slip in pressure-driven stokes flow. *J. Fluid Mech.*, 489:55–77, 2003.
- [175] M. Le Bars and M. G. Worster. Interfacial conditions between a pure fluid and a porous medium: implications for binary alloy solidification. *J. Fluid Mech.*, 550:149–173, 2006.
- [176] Min Hyung Lee, Mark D Huntington, Wei Zhou, Jiun-Chan Yang, and Teri W Odom. Programmable soft lithography: solvent-assisted nanoscale embossing. *Nano letters*, 11(2):311–315, 2010.
- [177] P. Van Leemput, C. Vandekerckhove, W. Vanroose, and D. Roose. Accuracy of hybrid lattice Boltzmann/finite difference schemes for reaction-diffusion systems. *Multiscale Model. Simul.*, 6(3):838–857, 2007.
- [178] P.V. Leemput, C. Vandekerckhove, W. Vanroose, and D. Roose. Accuracy of hybrid lattice Boltzmann/finite difference schemes for reaction diffusion systems. *Multiscale Model. Simul.*, 6(3):838–857, 2007.
- [179] Andrew P Leis, Sven Schlicher, Hilmar Franke, and Martin Strathmann. Optically transparent porous medium for nondestructive studies of microbial

- biofilm architecture and transport dynamics. *Applied and environmental microbiology*, 71(8):4801–4808, 2005.
- [180] Roland Lenormand, Eric Touboul, and Cesar Zarcone. Numerical models and experiments on immiscible displacements in porous media. *Journal of fluid mechanics*, 189:165–187, 1988.
- [181] Roland Lenormand, Cesar Zarcone, and A Sarr. Mechanisms of the displacement of one fluid by another in a network of capillary ducts. *Journal of Fluid Mechanics*, 135:337–353, 1983.
- [182] T. Lévy. Fluid flow through an array of fixed particles. *Int. J Eng. Sci.*, 21:11–23, 1983.
- [183] L. Li, C. Peters, and M. Celia. Upscaling geochemical reaction rates using pore-scale network modeling. *Adv. Water Resour.*, 29:1351–1370, 2006.
- [184] L. Li, C. Peters, and M. Celia. Upscaling geochemical reaction rates using pore-scale network modeling. *Adv. Water Resour.*, 29:1351–1370, 2006.
- [185] X. M. Li, D. Reinhoudt, and M. Crego-Calama. What do we need for a superhydrophobic surface? A review on the recent progress in the preparation of superhydrophobic surfaces. *Chem. Soc. Rev.*, 36:1350–1368, 2007.
- [186] P. C. Lichtner and D. M. Tartakovsky. Upscaled effective rate constant for heterogeneous reactions. *Stoch. Environ. Res. Risk Assess.*, 17(6):419–429, 2003.
- [187] Bowen Ling, Alexandre M Tartakovsky, and Ilenia Battiato. Dispersion controlled by permeable surfaces: surface properties and scaling. *Journal of Fluid Mechanics*, 801:13–42, 2016.
- [188] Chongxuan Liu, Jianying Shang, Sebastien Kerisit, John M Zachara, and Weihuang Zhu. Scale-dependent rates of uranyl surface complexation reaction in sediments. *Geochim. Cosmochim. Ac.*, 105:326–341, 2013.
- [189] Francis Ernest Lloyd et al. The carnivorous plants. *The carnivorous plants*, 1942.
- [190] R.P. Lowell, Y. Yao, and L.N. Germanovich. Anhydrite precipitation and relationship between focused and diffuse flow in seafloor hydrothermal systems. *J. Geophys. Res.*, 108(2424), 2003.
- [191] J. P. Lu. Elastic properties of carbon nanotubes and nanopores. *Phys. Rev. Lett.*, 79(7):1297, 1997.
- [192] L. B. Lucy. Numerical approach to the testing of the fission hypothesis. *Astronom.*

- J.*, 82:1013–1024, 1977.
- [193] A. V. Luikov. *Analytical heat diffusion theory*. Elsevier, 2012.
- [194] A. Malevanets and R. Kapral. Solute molecular dynamics in a mesoscale solvent. *J. chem. Phys.*, 112:7260–7269, 2000.
- [195] K. J. Maloy, J. Feder, F. Boger, and T. Jossang. Fractal structure of hydrodynamic dispersion in porous media. *Phys. Rev. Lett.*, 61(82):2925, 1998.
- [196] A. Marmur. The lotus effect: Superhydrophobicity and metastability. *Langmuir*, 20:3517–3519, 2004.
- [197] Horst Marschner and B Dell. Nutrient uptake in mycorrhizal symbiosis. *Plant Soil*, 159(1):89–102, 1994.
- [198] S. H. Maruf, A. R. Greenberg, J. Pellegrino, and Y. Ding. Fabrication and characterization of a surface-patterned thin film composite membrane. *J. Memb. Sci.*, 452:11–19, 2014.
- [199] S. H. Maruf, M. Rickman, L. Wang, J. Mersch IV, A. R. Greenberg, J. Pellegrino, and Y. Ding. Influence of sub-micron surface patterns on the deposition of model proteins during active filtration. *J. Memb. Sci.*, 444:420–428, 2013.
- [200] S. H. Maruf, L. Wang, A. R. Greenberg, J. Pellegrino, and Y. Ding. Use of nanoimprinted surface patterns to mitigate colloidal deposition on ultrafiltration membranes. *J. Memb. Sci.*, 428:598–607, 2013.
- [201] S. H. Maruf, L. Wang, A. R. Greenberg, J. Pellegrino, and Y. Ding. Use of nanoimprinted surface patterns to mitigate colloidal deposition on ultrafiltration membranes. *J. Memb. Sci.*, 428:598–607, 2013.
- [202] E. Marušić-Paloka and A. Piatnitski. Homogenization of a nonlinear convection-diffusion equation with rapidly oscillating coefficients and strong convection. *J. London Math. Soc.*, 2(72):391–409, 2005.
- [203] J. C. Maxwell. *A Treatise on Electricity and Magnetism*, volume 1 (Chp. 9, p. 403). Clarendon Press, London, 2nd edition, 1881.
- [204] Gary S May, Jiahua Huang, and Costas J Spanos. Statistical experimental design in plasma etch modeling. *IEEE Transactions on Semiconductor Manufacturing*, 4(2):83–98, 1991.
- [205] P. Meakin and A. M. Tartakovsky. Modeling and simulation of pore scale multiphase fluid flow and reactive transport in fractured and porous media. *Rev.*

*Geophys.*, page doi:10.1029/2008RG000263, 2008.

- [206] P. Meakin and A. M. Tartakovsky. Modeling and simulation of pore-scale multiphase fluid flow and reactive transport in fractured and porous media. *Rev. Geophys.*, 47:RG3002, 2009. doi:10.1029/2008RG000263.
- [207] Paul Meakin and Alexandre M Tartakovsky. Modeling and simulation of pore-scale multiphase fluid flow and reactive transport in fractured and porous media. *Reviews of Geophysics*, 47(3), 2009.
- [208] C. C. Mei. Method of homogenization applied to dispersion in porous media. *Transp. Porous Med.*, 9(3):261–274, 1992.
- [209] C. C. Mei and J.-L. Auriault. The effect of weak inertia on flow through a porous medium. *J. Fluid Mech.*, 222:647–663, 1991.
- [210] C. Meile and K. Tuncay. Scale dependence of reaction rates in porous media. *Adv. Water Resour.*, 29:62–71, 2006.
- [211] Carl D Meinhart, Steve T Wereley, and Juan G Santiago. Piv measurements of a microchannel flow. *Experiments in fluids*, 27(5):414–419, 1999.
- [212] CD Meinhart, ST Wereley, and MHB Gray. Volume illumination for two-dimensional particle image velocimetry. *Measurement Science and Technology*, 11(6):809, 2000.
- [213] Ferry PW Melchels, Jan Feijen, and Dirk W Grijpma. A review on stereolithography and its applications in biomedical engineering. *Biomaterials*, 31(24):6121–6130, 2010.
- [214] A Melling. Tracer particles and seeding for particle image velocimetry. *Measurement Science and Technology*, 8(12):1406, 1997.
- [215] M. Meyyappan. *Carbon nanotubes: science and applications*. CRC Press, Boca Raton, FL, 2005.
- [216] A. Mikelic, V. Devigne, and C. J. Van Duijn. Rigorous upscaling of the reactive flow through a pore, under dominant pecllet and damkohler numbers. *SIAM J. Math. Anal.*, 38(4):1262–1287, 2006.
- [217] A. Mikelic, V. Devigne, and C.J. van Duijn. Rigorous upscaling of the reactive flow through a pore, under dominant Péclet and Damköhler numbers. *SIAM J. Math. Anal.*, 38(4):1262–1287, 2006.
- [218] Cass T Miller, George Christakos, Paul T Imhoff, John F McBride, Joseph A Pedit,

- and John A Trangenstein. Multiphase flow and transport modeling in heterogeneous porous media: challenges and approaches. *Advances in Water Resources*, 21(2):77–120, 1998.
- [219] Marvin Minsky. Memoir on inventing the confocal scanning microscope. *Scanning*, 10(4):128–138, 1988.
- [220] S Mohammadi, A Maghzi, MH Ghazanfari, M Masihi, A Mohebbi, and R Kharat. On the control of glass micro-model characteristics developed by laser technology. *Energy sources, Part A: recovery, utilization, and environmental effects*, 35(3):193–201, 2013.
- [221] KK Mohanty, A Gupta, and RA Deruiter. Pore-level mechanisms of residual oil formation during miscible displacement. *Journal of colloid and interface science*, 163(1):199–216, 1994.
- [222] J. W. Morse and R. S. Arvidson. The dissolution kinetics of major sedimentary carbonate minerals. *Earth Sci. Rev.*, 58:51–84, 2002.
- [223] Heidi Nepf, M Ghisalberti, B White, and E Murphy. Retention time and dispersion associated with submerged aquatic canopies. *Water Resour. Res.*, 43(4), 2007.
- [224] H.M. Nepf. Flow and Transport in Regions with Aquatic Vegetation. *Annu. Rev. Fluid Mech.*, 44(1):123–142, 2012.
- [225] S. P. Neuman. Theoretical derivation of Darcy’s law. *Acta Mechanica*, 25:153–170, 1977.
- [226] S. P. Neuman and D. M. Tartakovsky. Perspective on theories of anomalous transport in heterogeneous media. *Adv. Water Resour.*, 32(5):670–680, 2009.
- [227] S. P. Neuman and D. M. Tartakovsky. Perspective on theories of anomalous transport in heterogeneous media. *Adv. Water Resour.*, 32(5):670–680, 2009.
- [228] D. A. Niel, S. L. M. Junqueira, and J. L. Lage. Forced convection in a fluid-saturated porous-medium channel with isothermal or isoflux boundaries. *J. Fluid Mech.*, 322:201–214, 1996.
- [229] Vladimir Nikora, Derek Goring, Ian McEwan, and George Griffiths. Spatially averaged open-channel flow over rough bed. *J. of Hydraul. Eng.*, 2001.
- [230] L. C. Nitsche and H. Brenner. Eulerian kinematics of flow through spatially periodic models of porous media. *Arch. Ration. Mech. Anal.*, 107(3):225–292, 1989.



- [231] M.D. Novak, J. S. Warland, A.L. Orchansky, R. Ketler, and S. Green. Wind tunnel and field measurements of turbulent flow in forests. part i: uniformly thinned stands. *Bound.-Layer Meteorol.*, 95:457–495, 2000.
- [232] J. A. Ochoa-Tapia, P. Stroeve, and S. Whitaker. Facilitated transport in porous media. *Chem. Engng. Sci.*, 46:477–496, 1991.
- [233] A. Ogata and R. B. Banks. A solution of the differential equation of longitudinal dispersion in porous media. *US Geol. Surv. Prof. Pap*, 411-A, 1961.
- [234] Mart Oostrom, Jacob H Dane, and Thomas W Wietsma. Removal of carbon tetrachloride from a layered porous medium by means of soil vapor extraction enhanced by desiccation and water table reduction. *Vadose Zone Journal*, 4(4):1170–1182, 2005.
- [235] Mart Oostrom, JH Dane, and Thomas W Wietsma. A review of multidimensional, multifluid, intermediate-scale experiments: Flow behavior, saturation imaging, and tracer detection and quantification. *Vadose Zone Journal*, 6(3):610–637, 2007.
- [236] Martinus Oostrom, Michael J Truex, George V Last, Christopher E Strickland, and Guzel D Tartakovsky. Evaluation of deep vadose zone contaminant flux into groundwater: Approach and case study. *Journal of contaminant hydrology*, 189:27–43, 2016.
- [237] Jia Ou, Blair Perot, and Jonathan P Rothstein. Laminar drag reduction in microchannels using ultrahydrophobic surfaces. *Phys. Fluids*, 16(12):4635–4643, 2004.
- [238] T. Paces. Rate constant of dissolution derived from the measurements of mass balances in catchments. *Geochim. Cosmochim. Acta*, 47:1855–1863, 1983.
- [239] J.L. Palandri and M.H. Reed. Geochemical models of metasomatism in ultramafic systems: serpentinization, rodingitization, and sea floor carbonate chimney precipitation. *Geochim. Cosmochim. Acta*, 68:1115–1133, 2004.
- [240] A. Papke and I. Battiato. A reduced complexity model for dynamic similarity in obstructed shear flows. *Geophys. Res. Lett.*, 40:1–5, 2013.
- [241] H.S. Park and W.K. Liu. An introduction and tutorial on multiple-scale analysis in solids. *Comput. Methods Appl. Mech. Engrg.*, 193:1733–1772, 2004.
- [242] Michael L Parks and Louis A Romero. Taylor–aris dispersion in high aspect ratio columns of nearly rectangular cross section. *Mathematical and computer modelling*, 46(5):699–717, 2007.

- [243] John E Paulsen, Eirik Oppen, and Rune Bakke. Biofilm morphology in porous media, a study with microscopic and image techniques. *Water Science and Technology*, 36(1):1–9, 1997.
- [244] M. A. Peter. Homogenization in domains with evolving microstructure. *C. R. Mécanique*, 335:357–362, 2007.
- [245] Zdeněk Petrášek and Petra Schwillé. Precise measurement of diffusion coefficients using scanning fluorescence correlation spectroscopy. *Biophysical journal*, 94(4):1437–1448, 2008.
- [246] Franck Plouraboué, Jean-Pierre Hulin, Stéphane Roux, and Joel Koplik. Numerical study of geometrical dispersion in self-affine rough fractures. *Physical Review E*, 58(3):3334, 1998.
- [247] P. Poncharal, Z. L. Wang, D. Ugarte, and W. A. de Heer. Electrostatic deflections and electromechanical resonances of carbon nanotubes. *Science*, 283(1513):DOI: 10.1126/science.283.5407.1513, 1999.
- [248] S. B. Pope. *Turbulent Flows*. Cambridge University Press, New York, USA, 2000.
- [249] S. Prager. Diffusion and viscous flow in concentrated suspensions. *Physica*, 29:129, 1963.
- [250] Ludwig Prandtl. Über flüssigkeits bewegung bei sehr kleiner reibung. *Verhaldlg III Int. Math. Kong*, pages 484–491, 1904.
- [251] Ajay K Prasad. Particle image velocimetry. *CURRENT SCIENCE-BANGALORE-*, 79(1):51–60, 2000.
- [252] M. Prat. On the boundary conditions at the macroscopic level. *Transp. in Porous Media*, 4:259–280, 1989.
- [253] M. Pratt. On the boundary conditions at the macroscopic level. *Transp. Porous Media*, 4:259–280, 1989.
- [254] R. F. Probstein. *Physicochemical Hydrodynamics*. Butterworth-Heinemann, Stoneham, MA, 1989.
- [255] Stephen R Quake and Axel Scherer. From micro-to nanofabrication with soft materials. *Science*, 290(5496):1536–1540, 2000.
- [256] M. Quintard and S. Whitaker. Convection, dispersion, and interfacial transport of contaminants: homogeneous porous media. *Adv. Water Resour.*, 17:221–239, 1994.

- [257] M. Quintard and S. Whitaker. Transport in ordered and disordered porous media II: Generalized volume averaging. *Transp. Porous Media*, 14:179–206, 1994.
- [258] M. Quintard and S. Whitaker. Transport in ordered and disordered porous media II: Generalized volume averaging. *Transp. Porous Media*, 14:179–206, 1994.
- [259] Michel Quintard and Stephen Whitaker. Transport in ordered and disordered porous media ii: Generalized volume averaging. *Transport in porous media*, 14(2):179–206, 1994.
- [260] H .Rajaram. Time and scale dependent effective retardation factors in heterogeneous aquifers. *Adv. Wat. Res.*, 20:217–230, 1997.
- [261] Edgar R Rangel-German and Anthony R Kovscek. Time-dependent matrix-fracture shape factors for partially and completely immersed fractures. *Journal of Petroleum Science and Engineering*, 54(3):149–163, 2006.
- [262] M Rashidi, L Peurrung, AFB Tompson, and TJ Kulp. Experimental analysis of pore-scale flow and transport in porous media. *Advances in Water Resources*, 19(3):163–180, 1996.
- [263] M. R. Raupach, J.J. Finnigan, and Y. Brunet. Coherent eddies and turbulence in vegetation canopies: the mixing-layer analogy. *Bound.-Layer Meteorol.*, 78:351–382, 1996.
- [264] M. R. Raupach and A. S. Thom. Turbulence in and above canopies. *Ann. Re. Fluid Mech.*, 13:97–129, 1981.
- [265] M. M. Reddy, L. N. Plummer, and E. Busenberg. Crystal growth of calcite from calcium bicarbonate solutions at constant  $p_{CO_2}$  and 25 c: a test for calcite dissolution model. *Geochimica et Cosmochimica Acta*, 45:1281–1289, 1981.
- [266] P. Reichert and O. Wanner. Enhanced one-dimensional modeling of transport in rivers. *J. Hydraul. Eng.*, 117(9):1165–1183, 1991.
- [267] D. H. Robertson, D.W. Brenner, and J. W. Mintmire. Energetics of nanoscale graphitic tubules. *Phys. Rev. B*, 45:12592, 1992.
- [268] Jonathan P Rothstein. Slip on superhydrophobic surfaces. *Annu. Rev. Fluid Mech.*, 42:89–109, 2010.
- [269] D. Roubinet, J.-R. Dreuzy, and D. M. Tartakovsky. Semi-analytical solutions for solute transport and exchange in fractured porous media. *Water Resour. Res.*, 48(1), 2012.

- [270] Philip Geoffrey Saffman and Geoffrey Taylor. The penetration of a fluid into a porous medium or hele-shaw cell containing a more viscous liquid. *The Royal Society*, 245(1242):312–329, 1958.
- [271] M. Sahimi. Flow phenomena in rocks: from continuum models to fractals, percolation, cellular automata, and simulated annealing. *Rev. Mod. Phys.*, 65(4):1393–1534, 1993.
- [272] Muhammad Sahimi. *Flow and transport in porous media and fractured rock: from classical methods to modern approaches*. John Wiley & Sons, 2011.
- [273] W.E. Sanford and L.F. Konikow. Simulation of calcite dissolution and porosity changes in saltwater mixing zones on coastal aquifers. *Water Resour. Res. WRERAO*, 25:655–667, 1989.
- [274] Juan G Santiago, Steve T Wereley, Carl D Meinhart, DJ Beebe, and Ronald J Adrian. A particle image velocimetry system for microfluidics. *Experiments in fluids*, 25(4):316–319, 1998.
- [275] John T Santini, Michael J Cima, and Robert Langer. A controlled-release microchip. *Nature*, 397(6717):335–338, 1999.
- [276] Adrian E Scheidegger. Statistical hydrodynamics in porous media. *Journal of Applied Physics*, 25(8):994–1001, 1954.
- [277] Hermann Schlichting. Zur entstehung der turbulenz bei der plattenströmung. *Nachrichten von der Gesellschaft der Wissenschaften zu Göttingen, Mathematisch-Physikalische Klasse*, 1933:181–208, 1933.
- [278] G. W. Schmid-Schonbein and D. N. Granger. *Molecular Basis for Microcirculatory Disorders*. Springer, New York, 2003.
- [279] I. Scholz, M. Bückins, L. Dolge, T. Erlinghagen, A. Weth, F. Hischen, J. Mayer, S. Hoffmann, M. Riederer, M. Riedel, and W. Baumgartner. Slippery surfaces of pitcher plants: Nepenthes wax crystals minimize insect attachment via microscopic surface roughness. *J. Exp. Biol.*, 213:1115–1125, 2010.
- [280] I. Seginer, P. J. Mulhearn, E. F. Bradley, and J. J. Finnigan. Turbulent flow in a model plant canopy. *Bound.-Layer Meteorol.*, 10:423–453, 1976.
- [281] T Senn, JP Esquivel, M Lörger, N Sabaté, and B Löchel. Replica molding for multilevel micro-/nanostructure replication. *Journal of micromechanics and microengineering*, 20(11):115012, 2010.
- [282] M. Shapiro and H. Brenner. Taylor dispersion of chemically reactive species:

- Irreversible first-order reactions in bulk and on boundaries. *Chem. Engrg. Sci.*, 41(6):1417–1433, 1986.
- [283] M. Shapiro and M. Brenner. Dispersion of a chemically reactive solute in a spatially periodic model of a porous medium. *Chem. Engrg. Sci.*, 43(3):551–571, 1988.
- [284] M. Shapiro, R. Fedou, J.-F. Thovert, and P. M. Adler. Coupled transport and dispersion of multicomponent reactive solutes in rectilinear flows. *Chem. Engrg. Sci.*, 51(22):5017–5041, 1996.
- [285] S.E. Silliman and E.S. Simpson. Laboratory evidence of the scale effect in dispersion of solutes in porous media. *Water Resour. Res.*, 23:1667–1673, 1987.
- [286] O. Singurindy, B. Berkowitz, and R.P. Lowell. Carbonate dissolution and precipitation in coastal environments: laboratory analysis and theoretical considerations. *Water Resour. Res.*, 40(W04401), 2004.
- [287] P. K. Smolarkiewicz and C. L. Winter. Pores resolving simulation of Darcy flows. *J. Comp. Phys.*, 229(9):3121–3133, 2010.
- [288] M Sohrabi, GD Henderson, DH Tehrani, A Danesh, et al. Visualisation of oil recovery by water alternating gas (wag) injection using high pressure micromodels-water-wet system. In *SPE Annual Technical Conference and Exhibition*. Society of Petroleum Engineers, 2000.
- [289] WE Soll, MA Celia, and JL Wilson. Micromodel studies of three-fluid porous media systems: Pore-scale processes relating to capillary pressure-saturation relationships. *Water resources research*, 29(9):2963–2974, 1993.
- [290] D. B. Spalding. A novel finite-difference formulation for differential expressions involving both first and second derivatives. *Int. J. Numer. Methods Eng.*, 4:551, 1972.
- [291] Todd M Squires and Stephen R Quake. Microfluidics: Fluid physics at the nanoliter scale. *Reviews of modern physics*, 77(3):977, 2005.
- [292] A. Srivastava, O. N. Srivastava, S. Talapatra, R. Vajtai, and P. M. Ajayan. Carbon nanotube filters. *Nature Materials*, 2004.
- [293] D. Srivastava, C. Wei, and K. Cho. Nanomechanics of carbon nanotubes and composites. *Appl Mech Rev*, 56(2):DOI: 10.1115/1.1538625, 2003.
- [294] C. I. Steefel, D. J. DePaolo, and P. C. Lichtner. Reactive transport modeling: An essential tool and a new research approach for the Earth sciences. *Earth Planet.*

- Sci. Lett.*, 240:539–558, 2005.
- [295] Ingo Steinbach, Franco Pezzolla, Britta Nestler, Markus Seeßelberg, Robert Prieler, Georg J Schmitz, and Joao LL Rezende. A phase field concept for multi-phase systems. *Physica D: Nonlinear Phenomena*, 94(3):135–147, 1996.
- [296] JS Steude, F Hopkins, and Jeffrey E Anders. Industrial x-ray computed tomography applied to soil research. *Tomography of Soil-Water-Root Processes*, 1(tomographyofsoi):29–41, 1994.
- [297] A. D. Stroock, S. K. W. Dertinger, A. Ajdari, I. Mezic, H. A. Stone, and G. M. Whitesides. Chaotic mixer for microchannels. *Science*, 295:647–651, 2002.
- [298] A. D. Stroock and G. M. Whitesides. Controlling flows in microchannels with patterned surface charge and topography. *Acc. Chem. Res.*, 36:597–604, 2003.
- [299] H.-B. Su, H. P. Schmid, C. S. Vogel, and P. S. Curtis. Effects of canopy morphology and thermal stability on mean flow and turbulence statistics observed inside a mixed hardwood forest. *Agric. Forest Meteorol.*, 148:862–882, 2008.
- [300] E. A. Sudicky and E. O. Frind. Contaminant transport in fractured porous media: Analytical solutions for a system of parallel fractures. *Water Resour. Res.*, 18(6):1634–1642, 1982.
- [301] M. C. Sukop and D. T. Thorne. *Lattice Boltzmann Modeling: An Introduction for Geoscientists and Engineers*. Springer, New York, 2005.
- [302] M. C. Sukop and D. T. Thorne, Jr. *Lattice Boltzmann Modeling: An Introduction for Geoscientists and Engineers*. Springer, New York, 2007.
- [303] D. H. Tang, E. O. Frind, and E. A. Sudicky. Contaminant transport in fractured porous media: Analytical solution for a single fracture. *Water Resour. Res.*, 17(3):555–564, 1981.
- [304] A. M. Tartakovsky, P. Meakin, and T. Scheibe. Simulations of reactive transport and precipitation with smoothed particle hydrodynamics. *J. Comput. Phys.*, 222(2):654–672, 2007.
- [305] A. M. Tartakovsky, P. Meakin, and T. Scheibe. A smoothed particle hydrodynamics model for reactive transport and mineral precipitation in porous and fractured porous media. *Water Resour. Res.*, 2007.
- [306] A. M. Tartakovsky, P. Meakin, T. D. Scheibe, and R. M. Eichler West. Simulation of reactive transport and precipitation with smoothed particle hydrodynamics. *J. Comp. Phys.*, 222:654–672, 2007.

- [307] A. M. Tartakovsky, P. Meakin, T.D. Scheibe, and R. M. Eichler West. Simulation of reactive transport and precipitation with smoothed particle hydrodynamics. *J. Comp. Phys.*, 222:654–672, 2007.
- [308] A. M. Tartakovsky, G. Redden, P. C. Lichtner, T. D. Scheibe, and P. Meakin. Mixing-induced precipitation: Experimental study and multi-scale numerical analysis. *Water Resour. Res.*, 44:W06S04, doi:10.1029/2006WR005725, 2008.
- [309] A. M. Tartakovsky, D. M. Tartakovsky, and P. Meakin. Stochastic Langevin model for flow and transport in porous media. *Phys. Rev. Lett.*, 101:044502, 2008.
- [310] A. M. Tartakovsky, D. M. Tartakovsky, and P. Meakin. Stochastic Langevin model for flow and transport in porous media. *Phys. Rev. Lett.*, 101:044502, doi:10.1103/PhysRevLett.101.044502, 2008.
- [311] A. M. Tartakovsky, D. M. Tartakovsky, T. D. Scheibe, and P. Meakin. Hybrid simulations of reaction-diffusion systems in porous media. *SIAM J. Sci. Comput.*, 30(6):2799–2816, 2008.
- [312] Alexandre Tartakovsky and Paul Meakin. Modeling of surface tension and contact angles with smoothed particle hydrodynamics. *Physical Review E*, 72(2):026301, 2005.
- [313] Alexandre M Tartakovsky and Alexander Panchenko. Pairwise force smoothed particle hydrodynamics model for multiphase flow: surface tension and contact line dynamics. *Journal of Computational Physics*, 305:1119–1146, 2016.
- [314] Alexandre M Tartakovsky, Andy L Ward, and Paul Meakin. Pore-scale simulations of drainage of heterogeneous and anisotropic porous media. *Physics of Fluids (1994-present)*, 19(10):103301, 2007.
- [315] D. M. Tartakovsky, M. Dentz, and P. C. Lichtner. Probability density functions for advective-reactive transport in porous media with uncertain reaction rates. *Water Resour. Res.*, 45:W07414, 2009.
- [316] G. Taylor. Dispersion of soluble matter in solvent flowing slowly through a tube. In *P. R. Soc. London*, volume 219, pages 186–203, 1953.
- [317] Geoffrey I Taylor. Diffusion by continuous movements. *Proceedings of the london mathematical society*, 20:196–211, 1921.
- [318] Larry F Thompson, C Grant Willson, Murrae J Bowden, et al. *Introduction to microlithography*. American Chemical Society, 1983.
- [319] N. Tokada, C. Akasaka, T.F. Xu, and K. Pruess. Reactive geothermal transport

- simulations to study the formation mechanism of an impermeable barrier between acidic and neutral fluid zones in the onikobe geothermal field, Japan. *J. Geophys. Res.*, 109(B05209), 2004.
- [320] M. M. J. Treacy, T. W. Ebbesen, and J. M. Gibson. Exceptionally high Young's modulus observed for individual carbon nanotubes. *Nature*, 1996.
- [321] LA Tse, PJ Hesketh, DW Rosen, and JL Gole. Stereolithography on silicon for microfluidics and microsensor packaging. *Microsystem Technologies*, 9(5):319–323, 2003.
- [322] W. Um, R. J. Serne, S. B. Yabusaki, and A. T. Owen. Enhanced radionuclide immobilization and flow path modifications by dissolution and secondary precipitates. *J. Environ. Qual.*, 34:1404–1414, 2005.
- [323] K. Vafai and S. J. Kim. Fluid mechanics of the interface region between a porous medium and a fluid layer—an exact solution. *Int. J. Heat and Fluid Flow*, 11(3):254–256, 1990.
- [324] F. J. Valdés-Parada, B. Goyeau, and J. A. Ochoa-Tapia. Diffusive mass transfer between a microporous medium and an homogeneous fluid: Jump boundary conditions. *Chem. Engrg Sci.*, 61:1692–1704, 2006.
- [325] F. J. Valdes-Parada, J. A. Ochoa-Tapia, and J. Alvarez-Ramirez. Validity of the permeability Carman–Kozeny equation: A volume averaging approach. *Physica A*, 388(6):789–798, 2009.
- [326] F.J. Valdes-Parada, J.A. Ochoa-Tapia, and J. Alvarez-Ramirez. On the effective viscosity for the Darcy-Brinkman equation. *Physica A*, 385:69–79, 2007.
- [327] C Van Ertbruggen, P Corieri, R Theunissen, ML Riethmuller, and C Darquenne. Validation of cfd predictions of flow in a 3d alveolated bend with experimental data. *Journal of biomechanics*, 41(2):399–405, 2008.
- [328] T. L. van Noorden and I. S. Pop. A Stefan problem modelling crystal dissolution and precipitation. *IMA J. Appl. Math.*, 73(2):393–411, 2008.
- [329] BGM Van Wachem and Alf-Erik Almstedt. Methods for multiphase computational fluid dynamics. *Chemical Engineering Journal*, 96(1):81–98, 2003.
- [330] DV Vayenas, E Michalopoulou, GN Constantinides, S Pavlou, and AC Payatakes. Visualization experiments of biodegradation in porous media and calculation of the biodegradation rate. *Advances in water resources*, 25(2):203–219, 2002.
- [331] M. Velbel. The mathematical basis for determining rates of geochemical and



- geomorphic processes in small forested watersheds by mass balance. Examples and implications. In S. Coleman and D. Dethier, editors, *Rates of Chemical Weathering of Rocks and Minerals*, pages 439–451. Academic Press, New York, 1986.
- [332] H. K. Versteeg and M. Malalasekera. *An Introduction to Computational Fluid Dynamics: The Finite Volume Method*. Pearson Education Ltd.; Harlow, England; New York, 2007.
- [333] B. Vigolo, A. Penicaud, C. Coulon, C. Sauder, R. Paillet, C. Journet, P. Bernier, and P. Poulin. Macroscopic fibers and ribbons of oriented carbon nanotubes. *Science*, 290(1331):DOI: 10.1126/science.290.5495.1331, 2000.
- [334] E. Villa, A. Balaeff, L. Mahadevan, and K. Schulten. Multiscale method for simulating protein-dna complexes. *Mult. Model. Simul.*, 2:527–553, 2004.
- [335] D. G. Vlachos, A. B. Mhadeshwar, and N. S. Kaisare. Hierarchical multiscale model-based design of experiments, catalysts, and reactors for fuel processing. *Comp. Chem. Engng.*, 30:1712–1724, 2006.
- [336] J.H. Walther, T. Werder, R.L. Jaffe, and P. Koumoutsakos. Hydrodynamic properties of carbon nanotubes. *Phys. Rev. E*, 69:062201, 2004.
- [337] Lichun Wang, M Bayani Cardenas, Wen Deng, and Philip C Bennett. Theory for dynamic longitudinal dispersion in fractures and rivers with poiseuille flow. *Geophysical Research Letters*, 39(5), 2012.
- [338] MW Wegner and JM Christie. Chemical etching of deformation sub-structures in quartz. *Physics and Chemistry of Minerals*, 9(2):67–78, 1983.
- [339] S. Weinbaum, X. Zhang, Y. Han, H. Vink, and S. C. Cowin. Mechanotransduction and flow across the endothelial glycocalyx. *PNAS*, 100(13):7988–7995, 2003.
- [340] Sheldon Weinbaum, Xiaobing Zhang, Yuefeng Han, Hans Vink, and Stephen C Cowin. Mechanotransduction and flow across the endothelial glycocalyx. *P. Natl. A. Sci.*, 100(13):7988–7995, 2003.
- [341] S. T. Weinman and S. M. Husson. Influence of chemical coating combined with nanopatterning on alginate fouling during nanofiltration. *J. Memb. Sci.*, 513:146–154, 2016.
- [342] H. L. Weissberg. Effective diffusion coefficient in porous media. *J. Applied Physics*, 34:2636, 1963.

- [343] Charles J Werth, Changyong Zhang, Mark L Brusseau, Mart Oostrom, and Thomas Baumann. A review of non-invasive imaging methods and applications in contaminant hydrogeology research. *Journal of Contaminant Hydrology*, 113(1):1–24, 2010.
- [344] J Westerweel. Fundamentals of digital particle image velocimetry. *Measurement science and technology*, 8(12):1379, 1997.
- [345] S. Whitaker. Flow in Porous Media I: A Theoretical Derivation of Darcy's Law. *Transp. Porous Media*, 1:3–25, 1986.
- [346] S. Whitaker. *The Method of Volume Averaging*. Kluwer Academic Publishers, Netherlands, 1999.
- [347] MD White and M Oostrom. Subsurface transport over multiple phases. Technical report, Pacific Northwest National Lab., Richland, WA (United States), 2006.
- [348] C.M. Wicks and J.S. Herman. Regional hydrogeochemistry of a modern coastal mixing zone. *Water Resour. Res.*, 32(2):401–407, 1996.
- [349] M. Widdowson, F. Molz, and L. Benefield. Numerical transport model for oxygen- and nitrate-based respiration linked to substrate and nutrient availability in porous media. *Water Resour. Res.*, 24:1553–1565, 1988.
- [350] Christian E Willert and Morteza Gharib. Digital particle image velocimetry. *Experiments in fluids*, 10(4):181–193, 1991.
- [351] Thomas Willingham, Changyong Zhang, Charles J Werth, Albert J Valocchi, Mart Oostrom, and Thomas W Wietsma. Using dispersivity values to quantify the effects of pore-scale flow focusing on enhanced reaction along a transverse mixing zone. *Advances in water resources*, 33(4):525–535, 2010.
- [352] Thomas W Willingham, Charles J Werth, and Albert J Valocchi. Evaluation of the effects of porous media structure on mixing-controlled reactions using pore-scale modeling and micromodel experiments. *Environmental science & technology*, 42(9):3185–3193, 2008.
- [353] J. D. Wilson, D. P. Ward, G. W. Thurtell, and G. E. Kidd. Statistics of atmospheric turbulence within and above a corn canopy. *Bound.-Layer Meteorol.*, 24:495–519, 1982.
- [354] John L Wilson, Stephen H Conrad, Edward Hagan, William R Mason, and William Peplinski. The pore level spatial distribution and saturation of organic liquids in porous media. In *Proceedings of the conference on Petroleum Hydrocarbons and Organic Chemicals in Ground Water: Prevention Detection and*

*Restoration*, 1988.

- [355] M. Wilson. Superhydrophobic surfaces reduce drag. *Phys. Today*, 2009.
- [356] T.-S. Wong, S. H. Kang, S. K. Y. Tang, E. J. Smythe, B. D. Hatton, A. Grinthal, and J. Aizenberg Aizenberg. Bioinspired self-repairing slippery surfaces with pressure-stable omniphobicity. *Nature*, 477, 2011.
- [357] B. D. Wood and R. M. Ford. Biological processes in porous media: From the pore scale to the field. *Adv. Water Resour.*, 30(6-7):1387–1391, 2007.
- [358] B. D. Wood, M. Quintard, and S. Whitaker. Jump conditions at non-uniform boundaries: the catalytic surface. *Chem. Engrg Sci.*, 55:5231–5245, 2000.
- [359] B. D. Wood, K. Radakovich, and F. Golfier. Effective reaction at a fluid-solid interface: Applications to biotransformation in porous media. *Adv. Water Resour.*, 30(6-7):1630–1647, 2007.
- [360] Y.-S. Wu, M. Ye, and E. A. Sudicky. Fracture-flow-enhanced matrix diffusion in solute transport through fractured porous media. *Transp. Porous Med.*, 81(1):21–34, 2010.
- [361] Younan Xia and George M Whitesides. Soft lithography. *Annual review of materials science*, 28(1):153–184, 1998.
- [362] Xiaofan Yang, Yashar Mehmani, William A. Perkins, Andrea Pasquali, Martin SchÄ nher, Kyungjoo Kim, Mauro Perego, Michael L. Parks, Nathaniel Trask, Matthew T. Balhoff, Marshall C. Richmond, Martin Geier, Manfred Krafczyk, Li-Shi Luo, Alexandre M. Tartakovsky, and Timothy D. Scheibe. Intercomparison of 3d pore-scale flow and solute transport simulation methods. *Advances in Water Resources*, pages –, 2015.
- [363] C. Ybert, C. Barentin, C. Cottin-Bizonne, P. Joseph, and L. Bocquet. Achieving large slip with superhydrophobic surfaces: Scaling laws for generic geometries. *Phys. Fluids*, 19(123601), 2007.
- [364] Yu Ye, Gabriele Chiogna, Olaf Cirpka, Peter Grathwohl, and Massimo Rolle. 5. experimental investigation of transverse mixing under helical flow conditions in saturated porous media. *Experimental Investigation of Plume Dilution in Three-Dimensional Porous Media*, page 100, 2016.
- [365] Thomas Young. An essay on the cohesion of fluids. *Philosophical Transactions of the Royal Society of London*, 95:65–87, 1805.
- [366] M.-F. Yu, B. S. Files, S. Arepalli, and R. S. Ruoff. Tensile loading of ropes of

- singlewall carbon nanotubes and their mechanical properties. *Phys. Rev. Lett.*, 84(24), 2000.
- [367] X. Yue and W. E. Numerical methods for multiscale transport equations and application to two-phase porous media flow. *J. Comput. Phys.*, 210:656–675, 2005.
- [368] Changyong Zhang, Karl Dehoff, Nancy Hess, Mart Oostrom, Thomas W Wietsma, Albert J Valocchi, Bruce W Fouke, and Charles J Werth. Pore-scale study of transverse mixing induced  $\text{CaCO}_3$  precipitation and permeability reduction in a model subsurface sedimentary system. *Environmental science & technology*, 44(20):7833–7838, 2010.
- [369] Changyong Zhang, Mart Oostrom, Jay W Grate, Thomas W Wietsma, and Marvin G Warner. Liquid  $\text{CO}_2$  displacement of water in a dual-permeability pore network micromodel. *Environmental science & technology*, 45(17):7581–7588, 2011.
- [370] Changyong Zhang, Mart Oostrom, Thomas W Wietsma, Jay W Grate, and Marvin G Warner. Influence of viscous and capillary forces on immiscible fluid displacement: Pore-scale experimental study in a water-wet micromodel demonstrating viscous and capillary fingering. *Energy & Fuels*, 25(8):3493–3505, 2011.
- [371] M. Zhang, S. Fang, A.A. Zakhidov, S. B. Lee, A. E. Aliev, C. D. Williams, K. R. Atkinson, and R. H. Baughman. Strong, transparent, multifunctional, carbon nanotube sheets. *Science*, 309(5738):1215–1219, 2005.
- [372] Xiao-Mei Zhao, Younan Xia, and George M Whitesides. Fabrication of three-dimensional micro-structures: Microtransfer molding. *Advanced Materials*, 8(10):837–840, 1996.